

Multiferroic interfaces of mixed valency systems studied from first principles

Dissertation

zur Erlangung des Doktorgrades der Naturwissenschaften
(Dr. rer. nat.)

der

Naturwissenschaftlichen Fakultät II
Chemie, Physik und Mathematik

der Martin-Luther-Universität
Halle-Wittenberg

vorgelegt von

Vladislav Borisov

geboren am 05.05.1988 in Irkutsk (Russland)

Datum der Verteidigung: 25.02.2015

Gutachterin bzw. Gutachter:

1. Prof. Dr. Ingrid Mertig, Martin-Luther-Universität Halle-Wittenberg
2. Prof. Dr. Steffen Trimper, Martin-Luther-Universität Halle-Wittenberg
3. Prof. Dr. Maria-Roser Valentí, Goethe-Universität Frankfurt am Main

Halle (Saale), den 16. Oktober 2014

Contents

1	Introduction	4
2	Multiferroic oxide interfaces	6
2.1	Oxides with perovskite structure	6
2.1.1	Structural aspects of bulk systems	7
2.1.2	Features of the electronic structure	8
2.1.3	Magnetism and exchange interactions	10
2.1.4	Origin of the ferroelectricity	14
2.1.5	Single-phase multiferroics	15
2.2	Phenomena at nanostructured oxide interfaces	17
2.2.1	Ferroelectricity in oxide films	17
2.2.2	Interfacial magnetoelectricity	20
2.2.3	Emergent electronic states	23
3	Theoretical Background	26
3.1	Density functional theory	26
3.1.1	Quantum many-body problem	26
3.1.2	Kohn-Sham equations	29
3.1.3	Common approximations in DFT	31
3.1.4	LDA+U method	33
3.2	Pseudopotential plane-wave approach	36
3.2.1	Plane-wave expansion	36
3.2.2	Core states and pseudopotentials	38
3.2.3	Projector-augmented waves	40
3.2.4	Structural optimization	41
3.3	Green's function method	44
3.3.1	KKR equations for periodic solids	44
3.3.2	Exchange coupling parameters	46
3.3.3	Coherent potential approximation	47
4	Electronic transport	50
4.1	Transport regimes	50
4.2	Ballistic tunneling transport	51
4.3	Tunneling effects in oxides	53
4.3.1	Tunneling electroresistance	54
4.3.2	Tunneling magnetoresistance	56
4.3.3	Multiferroic tunnel junctions	58
5	Selected results	60
5.1	2DEG at the SrTcO ₃ /BaTiO ₃ (001) interface	61
5.2	ME coupling in Co/PZT (001)	73
5.3	Magnetization modulation in LSMO/PTO	84

5.4 Spin-dependent transport in MFTJ	92
6 Summary	104
A Adaptive mesh refinement	106
B Bibliography	108
C List of publications	121
D Acknowledgements	123
E Curriculum vitae	124
F Eidesstattliche Erklärung	125

Introduction

Multiferroics are materials that combine two or more of the basic ferroic orders [1]. Most of the current research is concentrated on a specific class of multiferroic systems where the ferroelectric and magnetic orderings coexist, even in the absence of external fields [2, 3]. Under certain conditions, the spontaneously ordered electric dipoles and spin magnetic moments are coupled to each other, which is known as the magnetoelectric coupling phenomenon first proposed by Piere Curie and then observed in 1960 in the antiferromagnetic Cr_2O_3 material by Astrov [4]. The “Holy Grail” of the multiferroic physics is a material where this coupling is so strong, that the magnetization can be switched or rotated by means of the spontaneous polarization and *vice versa*. However, this sort of cross-coupling between the two order parameters is usually very weak in typical single-phase multiferroics, such as BiFeO_3 and TbMnO_3 . This originates already in the fact that magnetism and ferroelectricity have mutually exclusive mechanisms, which necessitates the search for new exotic origins of multiferroicity in single-phase systems and presents an interesting topic [2, 3, 5]. Another popular approach is to combine a ferromagnet and a ferroelectric in a two-component multiferroic heterostructure where both order parameters coexist only in the interface region [6]. Numerous experimental studies [7, 8], supported by first-principle calculations [9, 10], have demonstrated a range of possibilities to achieve large cross-couplings at such interfaces, with a plethora of ways to tune their functional properties.

An additional boost of interest in multiferroic interfaces, especially those based on oxides, in recent years can be explained by potential applications of these structures in spintronics. Multiferroicity combines the advantages of the field control of both the charge and the spin degrees of freedom and, in this respect, adds new functionality to the existing nanoelectronic devices. In particular, multiferroic tunnel junctions (MFTJ) have motivated researchers in the last decade due to the possibility of controlling the spin transport by external electric fields [9]. In these systems, the coexistence of the tunneling magneto- and electroresistances (TMR and TER) creates four-state memory devices with different resistances corresponding to the parallel/antiparallel orientation of the magnetization in the electrodes and two opposite polarizations. Additional degree of control is provided, if a strong coupling is present between the magnetic and the ferroelectric order parameters. In prominent cases, the sign of the TMR effect can be robustly switched by the polarization reversal of the ferroelectric side, as reported, for example, by Pantel et al. for epitaxial LSMO/PZT/Co junctions [11] where LSMO and PZT are perovskite alloys with the compositions $\text{La}_{0.67}\text{Sr}_{0.33}\text{MnO}_3$ and $\text{PbTi}_{1-x}\text{Zr}_x\text{O}_3$, respectively. Similar to the case of magnetoelectric materials, the use of electric fields instead of magnetic fields is beneficial and helps to reduce the energy consumption and the dimensions of electronic devices based on these new principles. The aforementioned examples convincingly demonstrate the prospects of multiferroic oxide-based nanostructures in spintronics and memory applications.

Physics of oxide interfaces is far from being completely understood, although considerable progress has been made both in theoretical approaches and experimental techniques. Novel electronic states that appear when two “usual” materials are brought

in contact with each other, as it happens for the $\text{LaAlO}_3/\text{SrTiO}_3$ system [12], deserve large attention. In each case, the derivation of a structure-property relation is the main challenge and, in this respect, modern *ab initio* electronic structure methods play a significant role in the development of this field. Regarding spintronics applications, the mechanism of electronic transport in multiferroic tunnel junctions in the presence of the interfacial magnetoelectric coupling is one of the main questions. A permanent goal in spintronics, the robust control of spin-dependent transport by electric fields, is of huge fundamental and practical importance. The discovery of new ways to achieve the effective control of transport and magnetism at the nanoscale requires furthermore a close interaction between theory and experiment.

The aim of this work is to study the electronic properties controlled by electric fields and, in particular, the magnetoelectric coupling phenomena in multiferroic oxide nanostructures where both magnetic and ferroelectric orders coexist. In the first part, unusual electronic behavior will be demonstrated for the new oxide system $\text{SrTcO}_3/\text{BaTiO}_3$ (001) where the ferroelectric polarization of BaTiO_3 creates a tunable two-dimensional electron gas (2DEG) in the interface region. The second part is devoted to the transport and magnetoelectric coupling phenomena in recently grown and measured LSMO/PZT/Co tunnel junctions. The origin of the field-manipulated spin-dependent transport observed in this system will be studied in details.

The issues highlighted above will be addressed in this work using first-principle electronic structure methods based on the density functional theory. The projector-augmented plane-wave pseudopotential method will be applied in most cases, although investigation of disorder effects in oxides will be done for selected systems within the Koringa-Kohn-Rostoker (KKR) Green function approach. The chosen *ab initio* techniques provide a detailed picture of the structure, electronic and magnetic properties, as well as electronic transport in complex solids.

The present work includes four parts. The introductory chapter aims at providing a brief overview of the physical properties of oxides with the perovskite structure. General electronic features and the origin of ferroic ordering are discussed, first, for bulk materials and, then, for oxide heterostructures and interfaces. At this point, the concept of the interfacial magnetoelectric effect is introduced and different approaches to its realization are described. In the second chapter, the theoretical background for the *ab initio* treatment of complex solid systems is briefly described. We start with a formulation of the density functional theory and make a comparison between different approximations that will be made use of throughout this work. Afterwards, the plane-wave expansion and, subsequently, the concept of a pseudopotential are in the focus of discussion in view of their further application to different systems. Another approach to the electronic structure problem, namely, the KKR Green function method together with its advantages is briefly outlined to conclude this part. The next chapter is devoted to the theory of coherent electronic transport. First, I mention different transport regimes that can be, in general, realized in solids and, in the following, restrict the discussion solely to the coherent transport. The basics of the Landauer-Büttiker formalism are described and the mechanism of tunneling as well as related phenomena in oxide junctions are discussed. In the closing chapter, the main results of this work are presented for a number of oxide interfaces that have demonstrated interesting physics. The thesis is concluded with a summary and the list of published papers.

CHAPTER 2

Multiferroic oxide interfaces

This introductory chapter gives an overview of the multiferroic oxide materials and nanostructured interfaces. A consistent picture of their physical properties can be obtained, first, by considering the specific features of the individual compounds that build the studied system and, then, by analyzing the interaction at the interface boundary between different components. This structure will be adopted in this chapter to present more clearly the progress and new challenges in the field of multiferroic physics.

In the first part, the fundamental properties of bulk materials that belong to the perovskite family of oxides are discussed, specifically, the general relations between the crystal structure and electronic as well as magnetic phenomena. The discussion is concluded with arguments, as to why the single-phase multiferroics are scarcely present among the known materials.

In the second part, the focus shifts to the new functionality that can be created at the nanostructured oxide interfaces. The size effects in ferroelectricity as well as the mechanism of the interfacial magnetoelectric coupling are addressed in view of the recent progress in both experimental and theoretical studies. The non-trivial character of the electronic states at the interface between two perovskites is highlighted on the example of $\text{LaAlO}_3/\text{SrTiO}_3$ heterostructure.

2.1 Oxides with perovskite structure

Oxide materials with the perovskite structure have been motivating researchers for many decades due to the broad spectrum of the physical phenomena observed in these structures. As inferred from the literature [13], virtually any phenomenon or property known in condensed matter physics can be found in the family of perovskite compounds. Such a variety of qualities is not only a matter of interest from the fundamental point of view, but also a reason for the wide application of the perovskite oxides in different technological branches, from gate dielectrics in MOSFET's to complex film structures for memory devices and detectors. Until the late 1960's perovskites were studied mostly in form of ceramics and composites [14]. Due to the recent successes in growing atomically well-ordered perovskite nanostructures with thin film geometry, the whole venue of possibilities for tuning and adjusting their properties in a controlled way has emerged. In this part, we discuss some of the fundamental aspects of the perovskite crystal symmetry, electronic structure and the origins of different ferroic properties in the bulk phase.¹ I will conclude by discussing the structure-property relation and the basic criteria for the occurrence of multiferroicity in oxide-based materials.

¹More details on the presented topics can be found in reviews [13, 15].

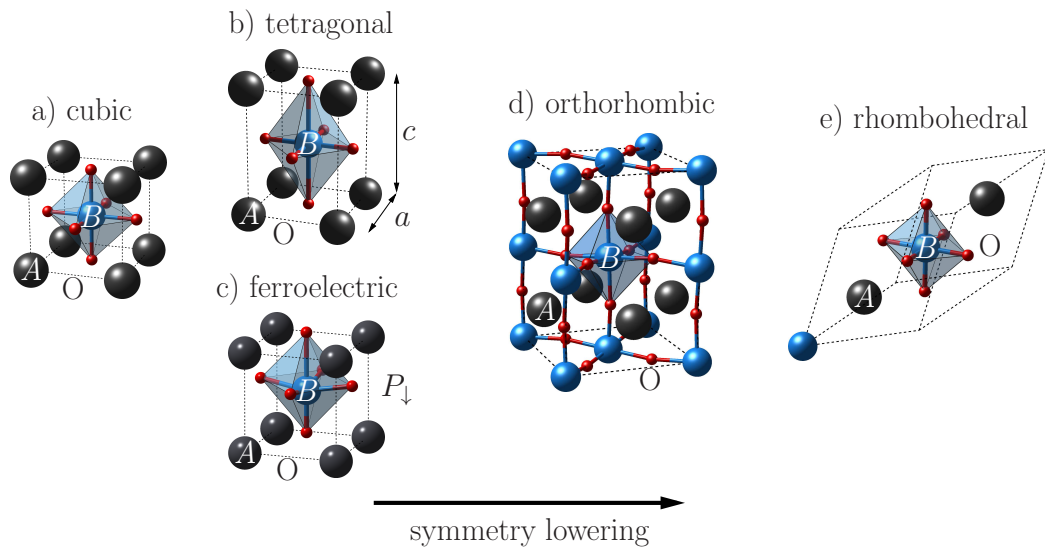


Figure 2.1: Sketch of perovskite structures with different crystal symmetries: a) cubic, b) tetragonal non-ferroelectric, c) tetragonal ferroelectric, d) orthorhombic, and e) rhombohedral.

2.1.1 Structural aspects of bulk systems

The simplest possible structure in the perovskite family is the cubic structure that possesses the unit cell depicted on Fig. 2.1a. In this crystal lattice, each transition metal (TM) cation is positioned at the center of the cube (B -site) and coordinated by six oxygen anions that form an octahedra. The larger cation, usually represented by mono-, di- or trivalent metal ions, occupies the corners of the cell (A -sites) and stabilizes the whole lattice. This is the structure with the highest symmetry that can be achieved in a perovskite compound. It has been experimentally established that oxides as paraelectric SrTiO_3 [16] and ferromagnetic metallic SrCoO_3 [17] adopt the cubic structure.

In contrast to this, the *tetragonally distorted structure* (Fig. 2.1b), which is frequently observed in epitaxially grown oxide films, shows an asymmetry between the in-plane (a) and out-of-plane (c) directions that are described by the corresponding lattice constants ($a \neq c$). This asymmetry is characterized by the elongation ratio ($\xi = c/a$) of the crystal lattice along $[001]$ direction. The tetragonal lattice is often observed for the ferroelectric perovskites, such as BaTiO_3 and PbTiO_3 [16, 18] where the symmetry is additionally reduced by the A – O and B – O ionic displacements (see paragraph 2.1.4 for more details). Paraelectric compounds (e.g. SrTiO_3) may become polarized in strained epitaxial films, where the tetragonal distortion due to a mismatch with the substrate favours the formation of a permanent ferroelectric polarization [19].

The next lower-symmetry structures are represented by *orthorhombic* and *rhombohedral* lattices (Fig. 2.1c and d), where a cooperative rotation of oxygen octahedra occurs around $[110]$ and $[111]$ crystallographic directions, respectively. The smallest unit cell of the orthorhombic structure contains 4 formula units (Fig. 2.1c), whereas the rhombohedral structure can be defined by one formula unit on a hexagonal lattice (Fig. 2.1d).

The ability of a perovskite to adopt a particular structure depends very much on the mismatch between the equilibrium length of the A – O and B – O bonds [13]. A

useful quantity here is the geometric tolerance factor

$$t = \frac{\langle d \rangle_{A-O}}{\sqrt{2} \langle d \rangle_{B-O}}. \quad (2.1)$$

In this definition, the average distances are approximated by the sum of the tabulated ionic radii [20, 21] of the corresponding cations/anions, e.g. $\langle d \rangle_{A-O} = \langle r \rangle_A + \langle r \rangle_O$. Compositions with the tolerance factor less than one ($t < 1$) have $B-O$ bonds under compressive and $A-O$ bonds under tensile strain. To reduce the internal strain the structure tends to lower its symmetry through rotations of the oxygen octahedra in certain directions. This gives rise to the whole variety of structures (cf. Fig. 2.1a-e). In the opposite case ($t > 1$), the $A-O$ bond is now under compression and the $B-O$ bond is under tension, which does not favor changes in the $B-O-B$ angles. Instead, a double-well potential may develop for the B cations, which results in the ferroelectric distortion of the lattice [13, 22–24]. An alternative way of relaxing the internal strain is realized in structures with the hexagonal stacking. The presented “rules” are based on purely geometric reasons and should not be viewed as an ultimate recipe for searching the preferable crystal symmetry, as the details of bonding can differ considerably from the aforementioned simple superposition of the ionic radii.

It is characteristic of perovskite materials to experience a series of first-order phase transitions with decreasing temperature where structures with lower symmetry appear one after another [25]. For instance, BaTiO_3 is paraelectric for high temperatures and adopts a highly symmetric cubic structure. As the temperature goes down to 403 K, the structure changes to tetragonal with a permanent ferroelectric polarization. Further decrease of temperature leads to the transition to a lower-symmetry orthorhombic phase at 278 K, which eventually transforms to a rhombohedral one below 183 K. In contrast to this, the PbTiO_3 compound shows only a single phase transition at 763 K from the cubic paraelectric to the tetragonal ferroelectric structure.

Further on, we discuss the characteristic features of the electronic structure that can be derived by considering the spin and orbital degrees of freedom of the transition metal cations and oxygen anions.

2.1.2 Features of the electronic structure

Many physical properties of oxides from the perovskite family can be understood and estimated based on the electronic configuration of the central d element and general conclusions about the hybridization effects together with the particular crystal symmetry, which usually suffices to draw a physically correct picture. For example, the expected magnetic ordering in a wide variety of single-valence compounds might be predicted using the generalized Goodenough-Kanamori-Anderson (GKA) rules [26]. However, due to rich orbital structure of d electrons many competing factors should be included in the consideration and, in most practical cases, only a detailed calculation is able to provide an answer, as to what particular electronic and magnetic structure can be expected from the compound. In this paragraph, the discussion will be restricted to a tight-binding-like picture [15] of the energy bands for a generic perovskite compound ABO_3 with a different symmetry of the lattice.

It is advantageous to start from the isolated A -, B - and oxygen atoms with the characteristic energies of the electronic states appearing in the order shown in Fig. 2.2a. Having been placed into the perovskite structure, these atoms attain certain oxidation

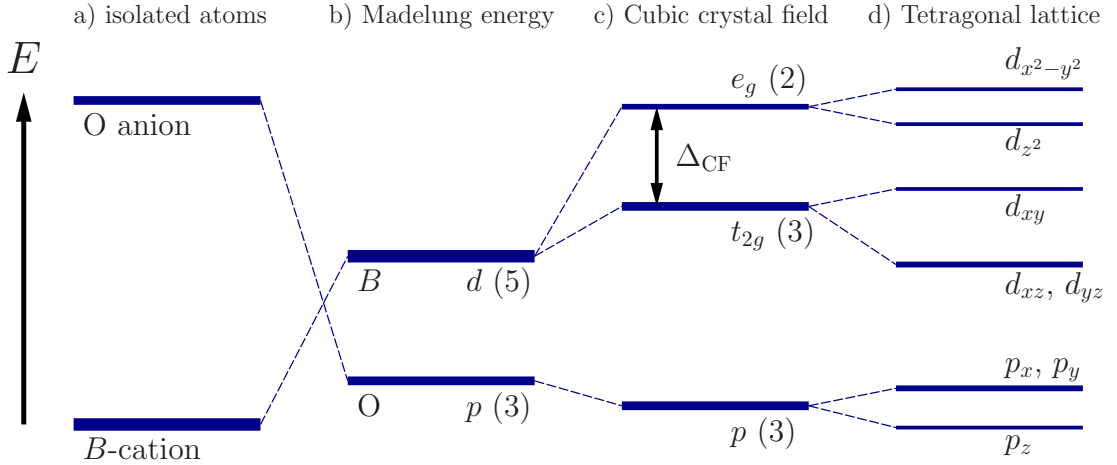


Figure 2.2: Schematic representation of the crystal field splitting of different energy levels for the perovskite structure: a) energy levels of the isolated atoms, b) shift of the energy levels due to the Madelung electrostatic potential, c) splitting of the d orbitals for the cubic lattice, d) partial lifting of the orbital degeneracy for the tetragonal symmetry. The degree of orbital degeneracy is shown by the number in round brackets.

states. For example, all alkali metals (Li, Na, K etc.) demonstrate the oxidation state 1+, whereas the 2+ state is characteristic of the alkaline earth metals (Ca, Sr and Ba). On the other hand, there is a plenty of elements (mostly transition metals) that possess two or even more stable oxidation states: chromium (Cr^{3+} and Cr^{6+}), manganese (Mn^{2+} , Mn^{4+} and Mn^{7+}), iron (Fe^{2+} and Fe^{3+}) and so on. Stabilization of a particular valence state in a perovskite compound is influenced by different factors, such as atomic environment and electronic correlations. In the first approximation, the ions in the lattice can be considered as point charges that create the crystal potential which is different for individual atomic sites. The sum of all electrostatic contributions from the surrounding ions for a given atomic site in the lattice determines the Madelung energy for this site, which is usually of the order of 10^1 – 10^2 eV [27]. The corresponding electrostatic potential on A - and B -sites is negative, whereas on the oxygen sites it is positive. Since electrons carry a negative charge, this picture of the crystal potential leads to the rearrangement of the electronic levels shown on Fig. 2.2b.

To this point, the orbital symmetry of the transition metal ions was not taken into account. For isolated elements, the d orbitals are degenerate due to the space symmetry. However, in the presence of the crystal field, the p and d levels shift in the energy due to the interplay between the orbital and crystal symmetries. It is convenient to define this splitting in terms of atomic-like orbitals of the d element: d_{xy} , d_{xz} , and d_{yz} with the t_{2g} symmetry and $d_{x^2-y^2}$ and d_{z^2} orbitals with the e_g symmetry. Of course, the d states in periodic solids with interacting atoms are different from what this simplified picture assumes. Nevertheless, the electronic states of the transition metal cation in the crystal can be still characterized in terms of the aforementioned atomic-like orbitals with different symmetry. In this case, the overlap of the electronic clouds of the central B -cation with the neighboring oxygen p orbitals and s states of the A -cations can be described analytically [27].

It turns out that the e_g orbitals are lifted in energy with respect to the t_{2g} orbitals. There are two main contributions to the splitting: i) point-charge contribution from oxygen ions; ii) covalency contribution due to the pd hybridization. Since the e_g orbitals are oriented directly towards the oxygen ions, they are subject to a much

larger Coulomb repulsion than the t_{2g} orbitals, which point at somewhat remoter A -cations. The overlap between the d and p orbitals, which leads to their hybridization and further splits these states, is stronger for the $e_g - p$ than for the $t_{2g} - p$ pairs. Together, the two aforementioned contributions lead to the value of the crystal field splitting (Δ_{CF}) of approximately 1–2 eV for the cubic structure (Fig. 2.2c).

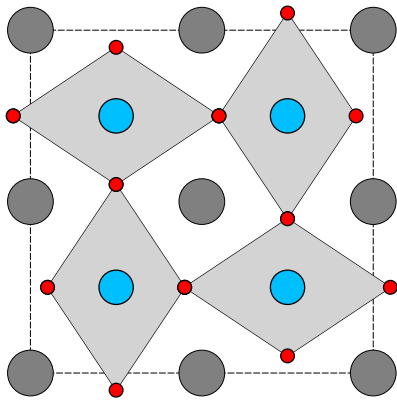


Figure 2.3: Collective distortion of the oxygen octahedra in transition metal oxides due to Jahn-Teller effect on d orbitals. Gray (blue) and red spheres mark the position of $A(B)$ -cations and oxygen anions in the lattice, respectively.

degeneracy of the e_g -levels that should be dealt with. The lifting of the degeneracy is realized by a cooperative distortion of the oxygen octahedra, a process that usually follows the pattern shown in Fig. 2.3. In the distorted lattice, it is common to observe an orbital ordering, since the elongation direction in each unit cell determines, which orbitals become occupied.

Due to the high symmetry of the cubic lattice some orbitals remain degenerate, e.g. all three t_{2g} -orbitals of the B -cation. For that reason, if we have to distribute a certain number of electrons on these d levels, an ambiguity might appear as to which of these orbitals should be occupied. According to the *Jahn-Teller theorem* [28], the only allowed degeneracy in the ground state of any system is the Kramers degeneracy, i.e. the degeneracy with respect to spin, which is observed in non-magnetic systems. An important consequence of this fact for the transition metal oxides is that, if any sort of orbital degeneracy exists in the system, it should be lifted by lowering the symmetry of the lattice, e.g. through deformation. This is the microscopic origin of the Jahn-Teller effect (JT) in perovskites. The JT effect is frequently observed in compounds with JT-active ions, such as Mn^{3+} [29], Cr^{2+} and Cu^{2+} .

2.1.3 Magnetism and exchange interactions

The driving mechanism for magnetism in the so-called itinerant magnets can be understood in terms of the *Stoner theory* [30]. In this picture, the magnetism appears due to the strong exchange interactions in the electron gas distributed over the volume of the solid. If one starts with a non-spin-polarized system and then pumps electrons from one spin channel to another, thereby increasing the imbalance between the spin-up and spin-down electron densities, then the Fermi energy and the average kinetic energy of electrons will increase substantially, which is unfavourable for magnetism. On the other hand, if the exchange processes, characterized by a constant I , are sufficiently strong, then the energy gain due to the formation of the magnetization is larger than the contribution from the kinetic energy and the magnetic state becomes energetically preferable. In this simple model, the criterium for the existence of the magnetization is expressed in terms of the density of states $n(E_F)$ at the Fermi level:

$$n(E_F) \cdot I > 1. \quad (2.2)$$

The Stoner model is well applied to simple ferromagnetic metals, such as Fe, Co and Ni, but fails for strongly correlated electronic systems where the magnetism might have a localized character. Since the nature of magnetism in condensed matter is

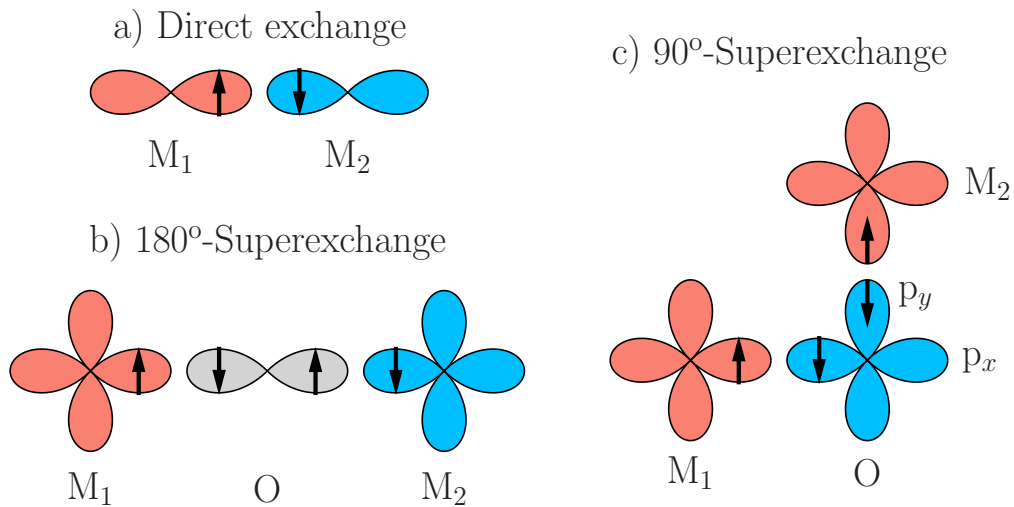


Figure 2.4: Different types of exchange interactions in transition metal (TM) oxides with the perovskite structure. The labels M_1 and M_2 denote the two interacting TM cations. The arrows show the spin direction of electrons on different d and p orbitals.

inherently interwoven with electronic interactions, which appear in the Stoner model simply as an empirical parameter I , advanced *ab initio* techniques might be necessary to treat the spin-polarized systems beyond the Stoner model. The effects of electronic correlations can be very different in this respect. For example, multiple spin states can be observed in the ferromagnetic SrCoO_3 compound and theoretical studies [31, 32] based on Hubbard formalism show that the interplay between different types of on-site and inter-site correlations determines which spin state is stabilized. This gives a flavour of the richness of physics that can be observed in perovskite compounds.

The electronic features of the TM oxides described above are decisive for the realization of a particular long-range magnetic ordering. Further on, we discuss different mechanisms of exchange interactions [26] and their influence on the magnetic properties of the perovskite compounds.

Direct exchange is the simplest type of exchange that is observed between half-filled orbitals of two neighboring TM cations (Fig. 2.4). In this system of two interacting spins there is a hopping of electrons from one site to another. This hopping is virtual in case of magnetic insulators and actual in case of metallic compounds. The energy gain due to the hopping process depends on the relative orientation of spins. For the parallel spin configuration, the hopping is forbidden by the Pauli principle. On the other hand, this process is allowed for the antiparallel orientation (see Fig. 2.4a) and according to the perturbation theory it lowers the energy of the system. One might conclude that the direct exchange prefers the antiparallel configuration of spins.

Superexchange is the dominating mechanism in magnetic insulating oxides. In these compounds, the exchange interaction between the neighboring TM ions is mediated by the oxygen p states (shown in Fig. 2.4b). The interaction is now a combination of two direct exchange processes and depends on the geometry of $M_1\text{-O-}M_2$ bonds, as well as on the orbital occupations of cations M_1 and M_2 . There is a number of rules, known as Goodenough-Kanamori-Anderson (GKA) rules [26], that help to predict the preferable magnetic ordering in perovskite compounds:

1. *Superexchange between half-filled orbitals for 180°-bonds is strongly antiferromagnetic.* The total energy is lower for the AFM configuration, since virtual hoppings

are allowed for both TM ions (see Fig. 2.4b).

2. *Superexchange between half-filled orbitals for 90°-bonds is weakly ferromagnetic.* For the 90°-exchange path, the half-filled d orbitals of ions M_1 and M_2 interact with different p orbitals of the neighboring oxygen. The parallel spin configuration is preferred due to Hund's coupling between the two oxygen electrons that appear there because of the virtual hopping (see panel **c** in Fig. 2.4).
3. *Superexchange between a half-filled and an empty orbital for 180°-bonds is weakly ferromagnetic (not shown on the figure).* The FM configuration of spins is, similarly to the previous case, related to Hund's coupling with the only difference that the virtual hopping occurs between orbitals of different symmetry.

In many cases, the GKA rules are useful for the general understanding of magnetic interactions in different oxides. For example, from the simple physical picture of 180°-superexchange it follows that perovskites with single-valence TM cations and nearly cubic structure should demonstrate antiferromagnetic ordering, which is indeed observed in the $ATcO_3$ series ($A = Ca, Sr, Ba$) [33, 34]. Sometimes it is necessary to combine several rules to interpret the observed magnetism, as is the case for undoped manganites, such as $LaMnO_3$. In this compound, interesting physics occurs: orbital ordering due to the Jahn-Teller effect leads to the anisotropic A-type AFM structure where strongly ferromagnetic atomic planes are weakly AFM coupled to each other [15].

The above discussion applies exclusively to insulating oxides with an integer occupation of d orbitals. Different physics arises in doped systems, where the average orbital occupation is changed by introducing impurities. Maybe the most prominent example of such system is the Sr-doped compound $La_{1-x}Sr_xMnO_3$ (shortly LSMO). Doped manganites like this show a very rich phase diagram (Fig. 2.7) as a function of doping level [35]. Whereas the host compound, $LaMnO_3$, is insulating with the A-type AFM ordering, the doped material becomes both strongly ferromagnetic and conducting for Sr-concentrations exceeding the critical value $x_{cr} = 0.18$. The interplay between the observed magnetic and transport properties of such oxides can be explained by the *double exchange* model first developed by Zener [36]. In this model, extra electrons/holes are formed on the TM sites due to the doping with impurities. These new charge carriers move freely through the crystal and interact with the magnetic background of localized spins on the TM cations (Mn in case of LSMO). For an AFM ordered system, the motion of charge carriers is inhibited because of Hund's coupling. In contrast to it, the hopping between the lattice sites is maximal for the FM ordered state. In general case, the hopping amplitude t_{ij} of an extra electron from site i to site j depends on the angle θ_{ij} between the spins of these two sites:

$$t_{ij} = t \cos \frac{\theta_{ij}}{2}. \quad (2.3)$$

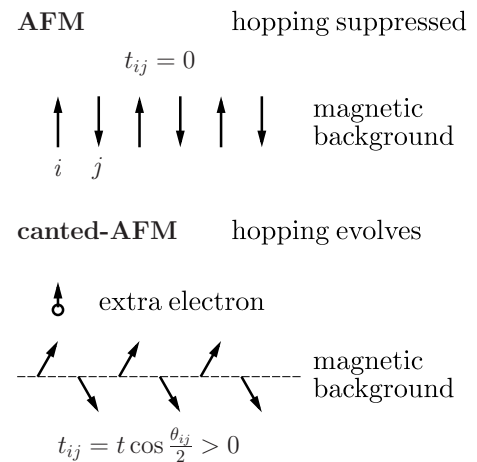


Figure 2.5: Mechanism of double exchange in correlated systems with a non-integer site occupation. Extra charge carriers that can freely hop between the neighbouring sites allow the system to minimize the total energy by adopting a canted AFM state.

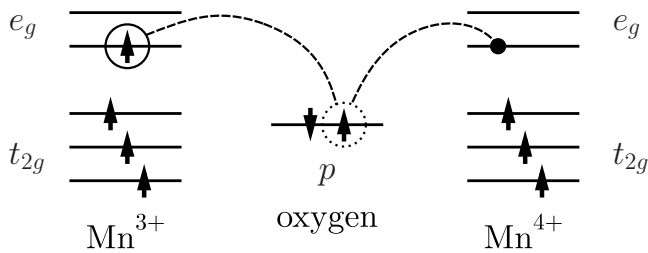


Figure 2.6: Double exchange between Mn^{4+} and Mn^{3+} cations in doped manganites mediated by the oxygen p states. The exchange process involves two successive hoppings that bring an electron from one e_g orbital to another (shown by dashed curves).

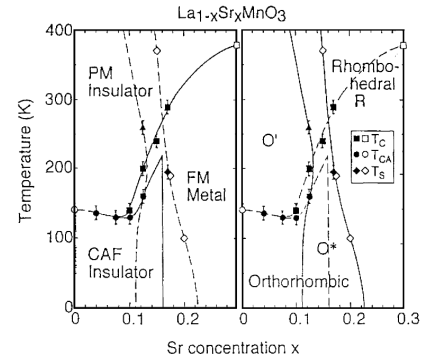


Figure 2.7: Magnetic and structural phase diagrams of the doped manganite $\text{La}_{1-x}\text{Sr}_x\text{MnO}_3$ as a function of temperature and hole concentration (reproduced from [37]).

The hopping changes from 0 to 1 as the ordering reconstructs from the AFM ($\theta = \pi$) to the FM ($\theta = 0$). In the original undoped system the orbitals of individual sites are singly occupied and the antiferromagnetic state is adopted, which provides the lowest energy (upper part of Fig. 2.5). The hopping between the neighboring sites is energetically unfavourable here. In the doped system, the possibility for electron hopping is increased proportionally to the doping level and, therefore, the energy can be additionally lowered by reducing the tilting angle θ_{ij} of spins, which increases the effective hopping t_{ij} . The competition between superexchange interactions and electron hopping leads to the formation of a canted AFM structure (lower part of Fig. 2.5). The canting angle θ increases with the doping level x until the whole material becomes ferromagnetic. This is the generally accepted model that accounts for the simultaneous transition to the ferromagnetic and conducting state in doped double-exchange oxides.

For the double exchange, we would like to have now a similar microscopic picture as we had in the case of superexchange. Let us turn again to the example of doped LSMO. In the original undoped system, all manganese cations are in the Mn^{3+} valence state with $t_{2g}^3 e_g^1$ electronic configuration of d orbitals. Substitution of some La atoms with Sr impurities leads to the creation of holes in e_g orbitals and the emergence of new valence state Mn^{4+} with only t_{2g} orbitals being occupied. Let us consider the exchange interaction between Mn^{3+} and Mn^{4+} cations through the intermediate oxygen p states (Fig. 2.6). In this example, electrons on the e_g orbitals can participate in the actual hopping process with two successive steps that end on the originally unoccupied e_g orbital of the Mn^{4+} cation (shown on the right side of Fig. 2.6). The spin of the hopping electron prefers to be parallel to the t_{2g} manifold, which plays the role of the magnetic background, due to Hund's coupling. Thus, the double exchange is ferromagnetic in the considered $\text{Mn}^{3+} - \text{O} - \text{Mn}^{4+}$ bond, whereas the superexchange in the $\text{Mn}^{3+} - \text{O} - \text{Mn}^{3+}$ bond is antiferromagnetic according to the aforementioned GKA rules. As pointed out already, the complicated interplay between different types of exchange interactions is partly the reason for a very sophisticated magnetic/electronic phase diagram of the doped compound $\text{La}_{1-x}\text{Sr}_x\text{MnO}_3$ (Fig. 2.7). Another contribution is related to structure. In the region of low Sr doping, the crystal structure is orthorhombic – the same as that of the parent compound LaMnO_3 . Starting from the critical Sr-concentration, the crystal symmetry changes to rhombohedral. Since exchange interactions are sensitive to the bond geometry, the magnetic phase diagram is additionally affected by structural phase transitions.

2.1.4 Origin of the ferroelectricity

Ferroelectricity in transition metal oxides with the perovskite structure is known since the 1940's, when the prototype compound barium titanate started to attract much attention as a new material for capacitors. The whole spectrum of applications of ferroelectric perovskites is too large to be considered here in any details. To mention just a few, it ranges from capacitors with high dielectric permittivity to memory elements and tunneling barriers in nanostructure devices. Further on, the mechanism of the conventional ferroelectricity in transition metal oxides is analyzed and different interpretations of this phenomenon are discussed.

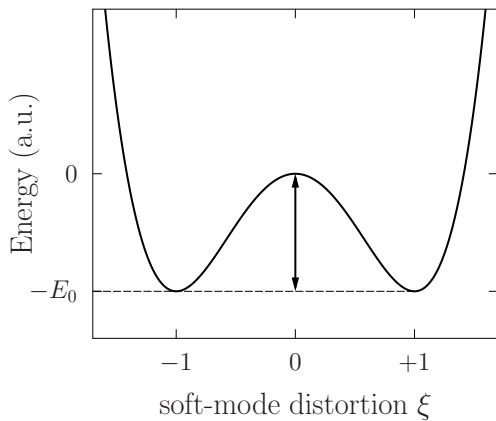


Figure 2.8: Qualitative behaviour of the total energy as a function of the soft-mode distortion value ξ for a bulk ferroelectric. The two stable polarization states ($\xi = -1$ and $\xi = +1$) are separated by a potential barrier E_0 .

favors a high-symmetry structure with no spontaneous polarization [23, 24]. On the other hand, the relative contribution of the LR dipole interactions can be estimated from the Born effective charges Z^* that describe the polarization created by an infinitesimal shift of a particular atom. Numerous *ab initio* studies on perovskite compounds confirm the significance of the covalent bonding and orbital hybridization for the formation of large effective charges that might exceed the nominal ionic charges by almost 100%, thereby providing the necessary conditions for the emergence of the ferroelectric instability (for review, see [25]).

From the viewpoint of lattice dynamics, the existence of the ferroelectric instability can be perceived from the total energy surface as a function of atomic coordinates. Starting from the paraelectric cubic structure and considering displacements along a certain direction, one arrives at the typical double-well shape of the energy surface (Fig. 2.8), which indicates the existence of an unstable transverse phonon mode at the Γ point in the high-symmetry crystal phase. This instability, also referred to as the *soft mode*, is characterized by imaginary frequency $\omega^2 < 0$ (within the harmonic approximation) coming from a negative curvature of the total energy surface at the origin $\xi = 0$. The eigenvectors of the soft mode define the pattern of ionic displacements that would lower the total energy of the crystal with respect to the paraelectric state. Therefore, one might interpret the emergence of the ferroelectric order as the softening of an unstable phonon mode that is thereby “frozen” in the whole crystal structure after the ferroelectric phase transition has occurred [22].

Ferroelectricity is a collective phenomenon that involves coherent ionic displacements not just in one cell but in the whole crystal. The observed spontaneous polarization results predominantly from the electric dipole moment created by the displaced ions. The fact that some systems demonstrate a permanent polarization in the absence of external electric fields indicates, among all, that the energy of these systems is lowered by the polar distortion and the corresponding transition to a lower-symmetry structure has occurred. The main criteria for this transition are based on the balance between short-range (SR) and long-range (LR) forces [38]. The SR forces originate from the repulsion of adjacent electron clouds, which

2.1.5 Single-phase multiferroics

The presence of partially occupied d orbitals is a necessary condition for the emergence of magnetism in transition metal oxides. On the other hand, the ferroelectricity relies on the combined ionic-covalent character of B –O bonds, which depends on the orbital hybridization between the B -cations and the surrounding oxygen ions. One might ponder the question, whether it is achievable to combine both ferromagnetic and ferroelectric orderings in a single-phase material. In reality, it turns out, however, that the driving mechanism of ferroelectric distortions is incompatible with partially filled d orbitals of the central TM cations. The exact reason for the importance of the formal d^0 -state of this ion is currently unknown. Many first-principle studies indicate that the emergence of the Jahn-Teller distortion for partially occupied d states is unfavourable for the development of the off-center displacements in the lattice [2]. Different ways to circumvent this “ d^0 -rule” have been proposed in the last decades, including the concepts of improper and geometrically driven ferroelectricity, as well as mechanisms relying on a highly polarized lone pair of 5s or 6s valence electrons. Detailed discussion of these and many other issues can be found in reviews [2, 3].

Other reasons for the scarcity of multiferroic materials exist that should be mentioned here. The appearance of a certain type of ferroic order in a crystal depends strongly on the symmetry group, to which the crystal belongs. For example, in a system with space inversion symmetry there is no possibility for a spontaneous polarization to evolve, just as there is no magnetic order in crystals with time inversion symmetry. It turns out that there are only 13 candidate point groups for multiferroics, where both space and time inversion symmetries are broken [1]. This narrows considerably the range of possible candidates. In addition, there is a very general difference between ferroelectric and ferromagnetic materials. Since ferroelectricity is driven by the long-range dipole forces that stabilize the spontaneous polarization, the material has to be insulating, since otherwise the conduction electrons screen the long-range Coulomb interactions and the ferroelectric instability is suppressed [2]. In contrast to this, magnetic materials are represented mostly by conducting systems, because magnetism involves partially occupied d states, which provide a finite density of states at the Fermi level.

One of the earliest attempts to circumvent the d^0 -rule took place in the 1950s, as researches started to investigate mixed perovskites [39]. In these compounds, some of the d^0 B -cations are replaced either in ordered or in disordered fashion by magnetic d^n cations, such as that of iron or cobalt. Examples of mixed perovskites include ordered $\text{Pb}_2(\text{CoW})\text{O}_6$ and disordered $\text{Pb}_2(\text{FeTa})\text{O}_6$ materials, which show coexisting magnetic and ferroelectric orders at low temperatures [40]. Unfortunately, since the magnetic cations are diluted in an otherwise nonmagnetic host, the critical temperature for the multiferroicity is rather low and, therefore, these materials are unlikely to find any applications. Much more promising venues opened with the discovery of multiferroicity in Bi-based perovskites of the series BiBO_3 that includes BiFeO_3 (BFO) and BiMnO_3 as the most studied compounds². Although the d orbital occupancy suppresses the ferroelectric distortions in the B –O planes, these systems still show a spontaneous polarization due to the strong covalent effects in the Bi–O bonds, where Bi 6p and O 2p states are involved in the hybridization process. First-principle calculations have demonstrated, for example, that the ferroelectricity in BiMnO_3 might be due

²Several papers on these compounds are referred to in the feature article [2].

to two different mechanisms, namely, the softening of a Γ -centered phonon mode and the purely electronic mechanism. However, the coexistence of two ferroic orders does not necessarily mean that there is a strong coupling between the corresponding order parameters. Indeed, the magnetoelectric effect in BiFeO_3 appears to be very weak in the bulk phase [41].

It can be seen, already from this rather simple analysis, that the coexistence of different ferroic orders, not to mention a strong coupling between them, in a single-phase material is very unlikely to be found in conventional systems. The revival of interest in multiferroics in recent years is related to the experimental findings that the multiferroicity in BFO is significantly enhanced for thin epitaxial films [7, 42]. In this respect, high-quality oxide nanostructures offer great perspectives for spintronics applications and, for that reason, are currently in the focus of the research community.

2.2 Phenomena at nanostructured oxide interfaces

The subsequent material will be devoted to new functionalities that can be achieved in oxide nanostructures. Special attention is paid to size effects in the electronic and ferroic properties as well as novel phenomena at oxide interfaces.

2.2.1 Ferroelectricity in oxide films

Previously, the general mechanism of emergence of the ferroelectricity in bulk transition metal oxides with the perovskite structure was considered (see paragraph 2.1.4). However, in modern applications of oxide materials they appear mostly in form of thin films grown epitaxially on a substrate. The latter imposes both structural constraints and electrostatic boundary conditions on the ferroelectric film. Depending on the nature of these conditions, the spontaneous polarization can be either suppressed or enhanced [14].

If an oxide is to be grown on a given substrate, a number of conditions have to be satisfied. Firstly, the crystal structures of the two materials should be compatible with each other in terms of crystal symmetry and atomic environment. The latter basically means that there should be a possibility for the stabilization of chemical bonds at the newly formed interface. Secondly, the lattice mismatch between the grown compound and the substrate has to be sufficiently low (within the range of $\pm 5\%$) to provide a stable regime of the epitaxial growth. As the two lattices are successfully matched at the interface, the structure of the grown oxide is usually tetragonally distorted along the growth direction to compensate for the deformation in the in-plane direction. In case of ferroelectric perovskites, this has a large effect on the value and the existence of the permanent polarization [43, 44]. For compressively strained perovskite films, out-of-plane elongation is most likely to occur and the ferroelectricity is enhanced, whereas it is usually suppressed in oxide films under a tensile strain. Under certain conditions, strain can even induce ferroelectricity in a paraelectric compound at room temperature, as it was observed for SrTiO_3 [45]. On the other hand, strain can also change the preferable direction of the ferroelectric polarization. For example, BTO prefers to be polarized along the [001] direction for the compressive strain, but shows in-plane ferroelectric domains under a tensile strain. Polarization is not the only property that depends on the strain: the coercive field E_c and the ferroelectric Curie temperature T_c (dynamical properties) are strongly influenced by the growth conditions as well and demonstrate large variations with film thickness [14, 46].

Another structural constraint comes from the surface termination of the substrate. For simple perovskite compounds ABO_3 , two types of termination might be observed for a (001)-surface: AO - and BO_2 -terminations. Which one of these is realized experimentally depends mostly on the details of the growth process. In epitaxial nanostructures, the ferroelectric BTO oxide grows usually in complete unit cells, as found, for example, in the BTO/Fe system [47, 48]. The preferred termination of an oxide surface/interface can be estimated in first-principle calculations by analysing the total energy of different atomic configurations. However, the disadvantage of most existing approaches is constituted in the fact that these are zero-temperature ground-state calculations, whereas in real systems various temperature- and defect-related contributions might change the energy balance towards an absolutely different structure, as is the case for the long-discussed LaAlO_3 free surface [49].

The double-well potential in thin ferroelectric films with a given termination is, generally, asymmetric with respect to the sign of the lattice distortion. The two stable polarization states possess different ground-state energies (E_1 and E_2 in Fig. 2.9). Consequently, one of these states is energetically preferable and, therefore, is expected to naturally appear in the growing film. Under certain conditions, the asymmetry of the double-well potential is so large that one of the states becomes unstable and the potential has only one minimum (red curve in Fig. 2.9). The latter describes a non-ferroelectric polar phase that, indeed, has a spontaneous polarization but it cannot be switched any more. It should be noted that the ionic displacements, which characterize the ferroelectric polarization, vary along the growth direction of the film and usually decrease near the free surfaces and interfaces depending on the direction of the polarization. Suppression of the local ferroelectric distortion has been observed, for instance, near the free surfaces of strongly ferroelectric BaTiO_3 and PbTiO_3 [50]. In the present work, this phenomenon is investigated for the two-component multiferroic Co/PZT [51] and LSMO/PTO interfaces.

An issue of extreme importance, especially for nanoelectronic devices, is the thickness dependence of the ferroelectric properties. Numerous experimental studies confirmed, for example, large variations and even complete suppression of the spontaneous polarization as the thickness goes down to several nanometers. This is related to the formation of a *depolarizing field* in the film, which might occur due to one of the following mechanisms: i) the presence of a "dead-layer" with degraded ferroelectric properties near the interface with an electrode, ii) the inhomogeneity of the spontaneous polarization and, consequently, the formation of volume charges, which increase the total electrostatic energy, and iii) the imperfect screening of the polarization charges by the electrodes. Whereas the first two cases can be successfully treated within phenomenological approaches, the latter mechanism is studied nowadays using first-principle methods. Let us proceed now with the discussion of this particular mechanism standing behind the depolarizing field, which is argued to govern the behaviour of ferroelectric films in spintronics devices.

The simplest model that introduces the concept of a depolarizing field can be worked out by considering the electrostatics of a free-standing ferroelectric slab in vacuum. Further on, the whole slab is assumed to be uniformly polarized perpendicular to the free surface ($\mathbf{P} = \text{const}$). From the basic principles of the physics of dielectrics it follows that the electric displacement vector \mathbf{D} is conserved at the boundary with vacuum, which implies a relation between the internal (\mathbf{E}_{in}) and the external (\mathbf{E}_{ext}) fields:

$$\mathbf{E}_{\text{in}} + 4\pi\mathbf{P} = \mathbf{E}_{\text{ext}}. \quad (2.4)$$

Two important conclusions are inferred from this relation. First, if we assume that the external field is zero $\mathbf{E}_{\text{ext}} = 0$, then a potential build-up will be observed

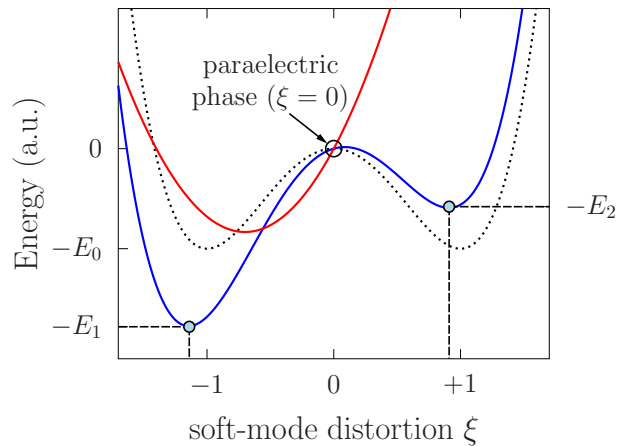


Figure 2.9: Qualitative behaviour of the total energy as a function of the soft-mode distortion value ξ for a ferroelectric oxide film (blue solid curve) in comparison with the bulk material (black dashed curve). The behaviour of a non-switchable polarized system is represented by the red curve.

in the film (left panel of Fig. 2.10). This corresponds to the internal field $\mathbf{E}_{\text{in}} = -4\pi\mathbf{P}$, which is oriented opposite to the ferroelectric polarization. The internal field increases the total electrostatic energy of the system and competes with the energy gain due to the emergence of the ferroelectric state. For sufficiently thin films, this makes a spontaneously polarized state energetically unstable. In this respect, the internal field can be viewed as a depolarizing field and its formation is intrinsic to low-dimensional structures, as follows already from this simple model. On the other hand, if an external field is applied to the sample in the direction of the polarization \mathbf{P} , then the internal field vanishes when the external field reaches $\mathbf{E}_{\text{ext}} = 4\pi\mathbf{P}$, which eliminates the depolarizing field and stabilizes the ferroelectric ordering.

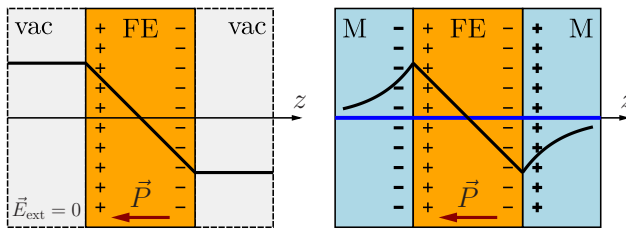


Figure 2.10: Electrostatic potential $V(z)$ in a polarized ferroelectric film under different boundary conditions: in the vacuum (left) and between two metallic electrodes (right). In the second case, the potential distribution for perfectly screening electrodes ($V(z) = 0$) is shown by the blue horizontal line.

This *ab initio* technique is known as *the dipole corrections* [52].

The model of a free-standing slab gives a flavour of the role that the electrostatic boundary conditions play in the stabilization of a polarized state in thin films. In a real system, however, the ferroelectric film is necessarily placed between two metallic electrodes and, therefore, one might be wondering, as to how the depolarizing field depends on the nature of the electrodes. In oxide-based spintronics, one can use either pure metals as electrodes or, alternatively, conductive transition metal oxides, such as SrRuO_3 or LSMO . The role of the electrodes is to screen the polarization charges σ_{pol} that appear on the opposite sides of the ferroelectric. If the electrodes were perfect metals, then the electric field of the bound charges σ_{pol} would be compensated by the screening electrons and the depolarizing field would vanish (blue horizontal line in the right panel of Fig. 2.10). In reality, however, the screening occurs over some finite distance characterized by the effective screening length λ_{eff} . Consequently, the distribution centers of the bound and screening charges no longer coincide with each other and finite dipoles are formed at both interfaces. The potential drop due to the dipole contribution has the same sign on both sides of the film and, therefore, finite electric field opposed to the polarization appears in the ferroelectric (black curve on the right side of Fig. 2.10). This explains the existence of a *critical thickness* for the emergence of ferroelectricity. Below this value the destructive effect of the internal depolarizing field prevails over the driving forces of ferroelectricity and the system becomes non-polarized. For good metallic electrodes, the critical thickness could be as small as 4-5 perovskite unit cells, as is the case for the $\text{Fe}/\text{BaTiO}_3/\text{Fe}$ system. However, if the electrodes are poorly conducting, then the depolarizing field destabilizes the ferroelectricity even for relatively thick films. The persistence of ferroelectricity in epitaxially grown thin oxide films down to several unit cells makes it possible to build tunneling nano-sized devices with electrically controlled transport properties.

A brief note should be made here.

In first-principle calculations, the short-circuit boundary conditions are implemented in most cases, which might lead to a spurious electric field that provides the periodicity of the electrostatic potential in the unit cell. In order to simulate the two previously discussed cases ($\mathbf{E}_{\text{ext}} = 0$ and $\mathbf{E}_{\text{in}} = 0$), a point dipole can be added to the vacuum layer. The magnitude and the sign of this dipole determine the concrete periodic boundary conditions.

The stability of a polarized state increases, generally, with the thickness of the film and also improves with the quality of the electrodes, which means smaller screening lengths. Further on in the text, in paragraph 4.3.1, this issue will be discussed in more details using a simple phenomenological model for the depolarizing field.

2.2.2 Interfacial magnetoelectricity

As pointed out already, the coexistence of two ferroic orders in a single-phase material is extremely rare due to several fundamental reasons (see paragraph 2.1.5). In contrast to it, multiferroic oxide nanostructures with ferroelectric and magnetic components separated by an interface have received much attention in the last years, since they allow to circumvent some of the problems of single-phase multiferroics. In particular, an appropriate choice of the components and growth conditions provides the existence of a robust multiferroic ordering at room temperature, which is advantageous for spintronics applications. Under certain conditions such nanostructures exhibit a strong *magnetoelectric (ME) coupling* effect that can fall into one of the two categories:

- direct ME coupling originating in electronic effects at the interface;
- indirect ME coupling mediated by a third-order parameter, e.g. strain.

The cross-coupling between different order parameters can be demonstrated by considering the interaction of the electric (\mathbf{E}), magnetic (\mathbf{H}) and stress (σ) fields with condensed matter. The system might possess, in general case, a permanent spontaneous polarization (\mathbf{P}_S), magnetization (\mathbf{M}_S) and deformation (ε_S) even in the absence of external fields. The thermodynamic properties of such systems can be described at the macroscopic level using the phenomenological Devonshire-Ginzburg-Landau (DGL) theory where the free energy F_0 is expanded in terms of increasing degrees of the order parameters. Under the influence of external fields additional contributions to the free energy appear, which are described, in the linear-response approximation, by the corresponding field susceptibilities $\hat{\chi}_E$, $\hat{\chi}_H$ and $\hat{\chi}_\sigma$. Expanding the free energy of the system up to the second order in the external fields gives the following expression³:

$$F = F_0 - (\mathbf{P}_S \mathbf{E} + \mu_0 \mathbf{M}_S \mathbf{H} + \varepsilon_S \sigma) + \frac{1}{2} [\varepsilon_0 \hat{\chi}_E \mathbf{E}^2 + \mu_0 \hat{\chi}_H \mathbf{H}^2 + \hat{\chi}_\sigma \sigma^2] + \quad (2.5)$$

$$+ [\mathbf{E} \hat{\alpha} \mathbf{H} + \mathbf{E} \hat{d} \sigma + \mathbf{H} \hat{q} \sigma].$$

The first group of terms after the zero-field free energy F_0 represents the dipole contributions to the free energy, and the second one – the electrostatic, magnetostatic and elastic energies (ε_0 and μ_0 are the dielectric and magnetic constants). The last three terms in this expansion describe different kinds of cross-coupling between the three order parameters (\mathbf{P} , \mathbf{M} and σ) and, therefore, are of the highest interest in the context of the present work. These cross-couplings are described by the new tensor quantities $\hat{\alpha}$, \hat{d} , and \hat{q} introduced in (2.5).

There can be more than one way to realize the magnetoelectric coupling in a real system. The first approach to this problem was based on the idea of connecting two

³Here, \mathbf{E} , \mathbf{H} and σ represent vector fields, whereas the susceptibilities in the second order terms are tensors. However, to simplify the notations, $\mathbf{E} \hat{\alpha} \mathbf{H}$ is written here instead of $\alpha_{ij} E_i H_j$.

order parameters, e.g. \mathbf{P} and \mathbf{M} , through a third-order parameter, such as strain. In case of piezoelectric and piezomagnetic components, the application of an electric field to the piezoelectric one causes elastic deformations that propagate into the piezomagnetic material and eventually lead to changes in the magnetization. The ME coupling realized in this way is called indirect, since it is mediated by another order parameter. The effect can be estimated as a product of two couplings:

$$\frac{\partial P_i}{\partial M_j} = \frac{\partial P_i}{\partial \sigma_k} \left[\frac{\partial M_j}{\partial \sigma_k} \right]^{-1}. \quad (2.6)$$

The indirect ME coupling effect has been extensively studied, especially for disordered composite multiferroics, and is nowadays applied in many existing magnetoelectric devices (see review [8]).

In the present work, the direct magnetoelectric coupling described by the term $\mathbf{E} \hat{\alpha} \mathbf{H}$ would be of particular interest. This sort of coupling allows manipulation of the macroscopic polarization by an external magnetic field and, vice versa, the magnetization of the material can be controlled by an external electric field:

$$\begin{aligned} \mathbf{P} &= -\frac{\partial F}{\partial \mathbf{E}} = \mathbf{P}_s + \varepsilon_0 \hat{\chi}_E \mathbf{E} + \hat{\alpha} \mathbf{H}; \\ \mathbf{M} &= -\mu_0^{-1} \frac{\partial F}{\partial \mathbf{H}} = \mathbf{M}_s + \hat{\chi}_M \mathbf{H} + \frac{\hat{\alpha}}{\mu_0} \mathbf{E}. \end{aligned} \quad (2.7)$$

It should be noted here that the ME coupling term $\mathbf{E} \hat{\alpha} \mathbf{H}$ breaks the time-reversal symmetry, so it cannot be present in the thermodynamic potential of a paramagnetic material where this symmetry is conserved [53]. Another situation is observed in magnetic systems, e.g. Cr_2O_3 , where other types of symmetry are present, so that non-zero cross-coupling terms appear.

In recent years, considerable progress has been made in growing well-ordered oxide nanostructures with a high degree of control of the interface structure and composition. This has opened many ways to realize experimentally a certain class of oxide interfaces where the direct magnetoelectric effect can be observed. The electronic origins of this coupling can be of different nature. In the following, the two most widely discussed mechanisms will be briefly introduced.

Electrostatic doping. At the interface between a ferromagnetic metal and a ferroelectric insulator measurable changes of the local magnetization can be induced by the polarization switching due to the effect of spin-dependent screening [54, 55]. The mechanism of the ME coupling is easily understood in this case: electrons in the metallic part, as usually, screen the electric field of the ferroelectric, which increases the electron density near the interface. However, the asymmetry between the spin-up and spin-down channels in the ferromagnet affects the density of screening electrons, which eventually contributes to the spin density imbalance and changes the magnetization. In this picture, the magnetoelectric effect is related to the phenomenon of *electrostatic doping*. If the metallic side is an itinerant ferromagnet, then the exchange splitting is also influenced by the electrostatic doping at the interface and the magnetoelectric response is additionally enhanced. Much more detailed discussion of the fundamentals of this electronic effect as well as its dynamical aspect can be found elsewhere [9, 56, 57].

The effect of the spin-dependent screening is predicted to determine the magnetic stability of half-metallic oxide interfaces. For instance, transition from the ferromagnetic to an antiferromagnetic ordering is expected for the interface between the ferroelectric BaTiO₃ and the half-metallic manganite La_{1-x}Sr_xMnO₃ with a certain concentration of the dopant [58]. Doped manganites are generally known for the rich phase diagram as a function of Sr-doping level x . At the aforementioned interface, the carrier concentration can be tuned through the electrostatic doping governed by the polarization of the ferroelectric side. If the initial doping level x is chosen close to the FM-AFM phase transition of the manganite (around $x = 0.5$), then the net magnetization of the half-metallic oxide can be changed by approximately $7 \mu_B$ by switching the polarization of BTO. Another compound, LSMO, with the composition La_{0.67}Sr_{0.33}MnO₃, which is often used as an electrode in tunnel junctions, is magnetically much more stable than the one in the previous example and, therefore, no magnetic transition is expected for this material. However, another interesting phenomenon has been experimentally observed in LSMO and described by Lu et al. [59]. For this perovskite grown epitaxially on the polar BTO substrate, the authors found evidence for a pronounced spatial modulation of the LSMO magnetization near the interface when the ferroelectric polarization points away from the LSMO film. The effect propagates into the manganite layer over the distance of several nanometers and is attributed both to the spin-dependent screening of the polarization charges and to the field-induced decrease of the LSMO Curie temperature.

Orbital hybridization. Another possibility for achieving the direct MEC effect relates to polarization-dependent interface bonding. This mechanism has been predicted for the first time for the prototype system of Fe layers on the ferroelectric surface of BaTiO₃ [47, 60–62]. Due to the strong orbital hybridization of the 3d states of Fe and Ti across the interface, spin-dependent charge transfer is observed for the polarization pointing towards the Fe film. The charge transfer results in a finite occupation of the Ti d orbitals and sizeable induced magnetic moments of the order of $0.3 \mu_B$ per each Ti site, which was confirmed by X-ray resonant magnetic scattering spectroscopy experiments [63]. In subsequent *ab initio* studies by different authors, the interfacial ME coupling effect related to orbital hybridization has been predicted and investigated for a number of similar systems (for a review see [9, 10]). It has been concluded that the strength of the ME coupling depends on the features of the covalent bonding between the two materials. The latter can be tuned by introducing impurities or vacancies into the system [64–66].

In all studies presented in the literature, the direct ME coupling is localized to a few atomic layers within the interface region. On the other hand, the ME coefficient for the two-component multiferroics is four orders of magnitude larger than that of single-phase multiferroics, not to mention the temperature range of existence of this effect. Moreover, by controlling the interface properties in low-dimensional electronic devices it is possible to alter dramatically their functional characteristics and, in this respect, the interfacial ME coupling might become a useful tool for adjusting the functionality of nanostructures.

2.2.3 Emergent electronic states

The reason for the large attention to the oxide-based nanostructures in the last years is related to the amazing diversity of physical properties shown by oxide materials and numerous possibilities of controlling their functional parameters. From the fundamental point of view, the most important issue here is the emergence of novel electronic states at the interface between two oxide compounds which bring new functionality not existent in the bulk materials.

Probably the most prominent example of this phenomenon is the formation of a quasi-two-dimensional electron gas (2DEG) at the (001)-oriented interface between two band insulators, LaAlO_3 and SrTiO_3 [12]. The mechanism leading to the conducting behaviour in this structure is traditionally ascribed to the polar discontinuity problem [67] and studies on this topic are vastly presented in the literature (for a review see [68, 69]). The polar discontinuity arises from the fact that the positively and negatively charged $(\text{LaO})^+$ and $(\text{AlO}_2)^-$ atomic planes of the LAO oxide have to be matched at the interface with the neutral layers of STO. For the formal ionic charges, this leads to the infinite growth of the electrostatic potential inside the LAO part, which is energetically unfavorable. Therefore, the system tends to get into a state with a lower total energy by transferring half an electron (half a hole) to the n-type (p-type) LAO/STO interface (Fig. 2.11), which makes the electrostatic potential finite [67]. At the n-type interface, the excess charge is detected as a 2DEG with a high mobility and concentration of charge carriers. Numerous experimental studies have shown that this oxide interface demonstrates a number of unexpected physical properties, such as field-controlled 2D superconductivity [70] that coexists, in theory, with magnetism [71], magnetoresistance [72], switchable electronic transport [73] etc. This would imply a wide spectrum of potential applications, especially, in spintronics and nanoelectronics [74]. In contrast to it, the p-type interface remains insulating and there is still no complete physical picture that would account for this asymmetry between the two interfaces. In existing *ab initio* works, different mechanisms related to the polar discontinuity scenario are usually addressed. These can be arranged in two large groups:

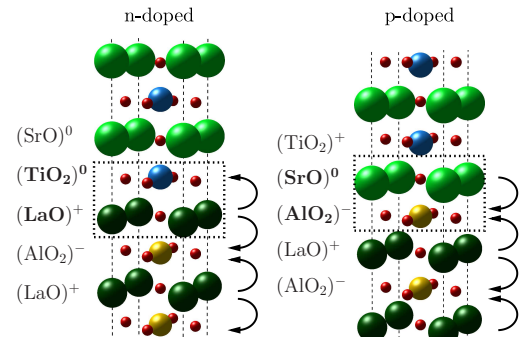


Figure 2.11: The polar discontinuity at the ideal n- and p-doped $\text{LaAlO}_3/\text{SrTiO}_3$ (001) interfaces. Each curved arrow shows the direction of transfer of half an electron from one atomic monolayer to another.

- **Intrinsic mechanisms**

1. *Electronic reconstruction.* The excess half an electron at the LaO/TiO_2 -terminated interface can be accommodated by the Ti cations, which allow for different valence states and attain, in this case, an effective valency of $3.5+$, opposed to $4+$ in the bulk. Strong electronic correlations on the Ti sites might cause a mixed valency pattern on the interface with the checker-board arrangement of $\text{Ti}^{4+}/\text{Ti}^{3+}$ cations [68]. Sizeable fraction of Ti^{3+} sites has been confirmed already in earlier experiments on electron energy loss spectroscopy [67], where the dominance of the electronic reconstruction scenario is argued for the n-type structure.
2. *Lattice distortions.* Thin LAO films grown epitaxially on the STO substrate are

known to demonstrate a metal-insulator transition starting from the thickness of 4–5 unit cells (u.c.) [73]. This effect is usually explained by a potential build-up inside the LAO layers due to the polar discontinuity at the interface. When additional layers of the LAO oxide are grown, the band gap of the structure decreases by 0.4 eV/ML and, finally, closes at the critical thickness. This leads to the electronic reconstruction accompanied by the transfer of electrons (holes) from the free LAO surface to the interface region. How this process occurs in reality is not known up to now. Surface X-ray diffraction experiments have confirmed the appearance of strong lattice distortions in epitaxial LAO films, which are argued to reduce the effect of the internal field. However, there is no experimental evidence for the existence of a measurable internal field in these structures. This should question the proposed mechanism of the metal-insulator transition.

- **Extrinsic mechanisms**

1. *Oxygen defects.* The conducting properties of the LAO/STO interface depend on the growth conditions, in particular, on the oxygen pressure. In a low pressure regime (10^{-6} mbar), the n-type interface shows a 3D conductivity comparable to the extrinsic conductivity of an oxygen-deficient bulk STO. For medium oxygen pressures (10^{-4} mbar), the n-type interface shows a 2D superconductivity that can even coexist with magnetism [71]. Finally, in the high pressure range (10^{-3} mbar), the aforementioned 2D electron gas is observed at the interface. This assumes that oxygen vacancies, although sparsely present in the sample, play a noticeable role in the electronic properties of the oxide interface. *Ab initio* calculations show that, for the n-type structure, the formation of an oxygen vacancy is energetically preferable near the free LAO surface starting from the critical thickness of 4–5 u.c. and, for the p-type structure, the vacancy is likely to form directly at the interface [69]. In the former case, the vacancy provides additional electrons, thereby increasing the carrier density at the interface, and, in the latter case, it partially compensates for the polar discontinuity, which makes the interface insulating. In other study [71], it was proposed that oxygen vacancies are responsible for the emergence of magnetism in this oxide system.
2. *Cation intermixing.* Another possibility for the compensation of the polar discontinuity is a substitutional disorder on the cation sublattices. The disorder can appear either on the interface in the form of La/Sr and Al/Ti cation intermixing or at the free surface of the LAO film. Progressive interface roughness has been observed in LAO/STO superlattices [67] containing only one type of the interface, which can be considered as an evidence for the cation intermixing. This effect is expected to be thickness-dependent, in a large similarity to the above-mentioned mechanism based on oxygen vacancies.
3. *Metal/oxide capping.* The importance of the free LAO surface for the electronic reconstruction has been pointed out in several studies [68, 75, 76]. In fact, the metal-insulator transition can be initiated already for 2 u.c.-thick LAO films through an appropriate surface engineering, namely, by growing an additional STO capping layer on top of the system. For the TiO_2 -terminated capping layer, there is a strong shift of the valence bands towards the Fermi level in the upper STO part, which closes the band gap and induces the 2DEG at the n-type

interface. On the other hand, in the system with SrO-terminated capping layer there is no additional band bending near the surface and the interface remains insulating below the critical thickness.

At the moment, there is no satisfactory explanation for the remarkable properties of the LAO/STO interface, although intensive research is continued in this direction. After the work of Ohtomo and Hwang in 2004, attempts to understand the physics of oxide heterostructures escalated and led to the confirmation of the aforementioned effects in similar heterostructures with the STO-substrate where the LaAlO_3 -part is replaced by LaGaO_3 [77], RO ($R=\text{La, Pr, Nd, Sm, Y}$) [78] or LaVO_3 [79]. This should serve as a demonstration of the complexity of physical phenomena at oxide interfaces, many of them still remaining to be discovered.

CHAPTER 3

Theoretical Background

Theory of electronic structure is nowadays a solid instrument for studying and interpreting physical phenomena in solids. Although the fundamental equation of this theory – the Schrödinger equation – was formulated already in late 1925, the practical side of the theory with its applications to solids is still being developed and expanded to provide a reliable description of physics in electronic systems. Current electronic structure methods allow a complex analysis of electronic, magnetic and transport properties starting from very general equations and a small number of model parameters.

In this chapter, the theoretical basis of the electronic structure and density functional theory (DFT) will be presented.

The first part constitutes a brief introduction into the formulation and main ideas of DFT and the most common approximations regarding the electronic correlations. In the next subsection, the plane-wave based representation of the Kohn-Sham equations and the related concept of pseudopotential are discussed in details. Finally, a totally different approach to the electronic structure based on the Green functions and multiple scattering theory is sketched and the advantages of this method in comparison to other techniques are outlined.

3.1 Density functional theory

3.1.1 Quantum many-body problem

Consistent quantum-mechanical description of condensed matter requires the solution of the corresponding many-body problem. In solid state physics, systems of interest are composed of a crystal lattice with a certain number N_{at} of positively charged atomic nuclei with masses M_n and charges Z_n ($n = 1 \dots N_{\text{at}}$) and N negatively charged electrons with masses m and elementary charges $e < 0$. For this system of interacting particles, one can write the Hamiltonian \hat{H} of the following general form:

$$\begin{aligned} \hat{H}(\mathbf{R}_1 \dots \mathbf{R}_{N_{\text{at}}}; \mathbf{r}_1 \dots \mathbf{r}_N) = & \sum_{n=1}^{N_{\text{at}}} \overbrace{\left[-\frac{\hbar^2}{2M_n} \nabla_n^2 + \frac{1}{2} \sum_{m \neq n}^{N_{\text{at}}} \frac{e^2 Z_m^2}{|\mathbf{R}_n - \mathbf{R}_m|} \right]}^{T_n \text{ Nuclei } V_{nn}} + \\ & + \sum_{i=1}^N \overbrace{\left[-\frac{\hbar^2}{2m} \nabla_i^2 + \frac{1}{2} \sum_{j \neq i}^N \frac{e^2}{|\mathbf{r}_i - \mathbf{r}_j|} \right]}^{T_e \text{ Electrons } V_{ee}} + \overbrace{\sum_{n=1}^{N_{\text{at}}} \frac{e^2 Z_n}{|\mathbf{r}_i - \mathbf{R}_n|}}^{\text{Electron-Nuclei } V_{en}}, \end{aligned} \quad (3.1)$$

where $\{\mathbf{R}_1 \dots \mathbf{R}_{N_{\text{at}}}; \mathbf{r}_1 \dots \mathbf{r}_N\}$ stands for the set of atomic and electron coordinates.

The full many-body wavefunction Ψ describing the solid satisfies the Schrödinger equation

$$\hat{H}\Psi = E\Psi. \quad (3.2)$$

This is an eigenvalue problem, and its solution gives the total energy E of the interacting system.

In this many-body problem three types of interactions have to be taken into account: nucleus-nucleus repulsion, attraction between the nuclei and the electrons and, finally, the electron-electron repulsion. All the listed interactions are essentially Coulomb electrostatic interactions between charged particles, but due to quantum correlation effects the electron-electron part appears as the most problematic. Because of this fact and the large number of degrees of freedom in a crystal, the exact solution of the problem represented by equations (3.1) and (3.2) is not feasible without introducing serious approximations. The first important step in this direction was the Born-Oppenheimer (adiabatic) approximation [80]. Due to the large difference in the masses of nuclei and electrons ($M_n \gg m$), their motion can be separated from each other. At any instant of time the crystal lattice looks “frozen” to the electronic subsystem, i.e. for each atomic configuration $\mathbf{R} = \mathbf{R}_1 \dots \mathbf{R}_{N_{\text{at}}}$ the electrons are found in the ground state, whose energy depends parametrically on the nuclei positions. The many-body wavefunction can be factorized into nuclei ($\Psi_n(\mathbf{R})$) and electron ($\Psi_{el}(\mathbf{r})$ where $\mathbf{r} = \mathbf{r}_1 \dots \mathbf{r}_N$) wavefunctions and the general Hamiltonian is correspondingly split into two parts:

$$\begin{cases} \Psi(\mathbf{X}) = \Psi_n(\mathbf{R}) \cdot \Psi_{el}(\mathbf{r}) \\ \hat{H} = \hat{H}_n + \hat{H}_{el}. \end{cases} \quad (3.3)$$

The problem is now reduced to the solution of the electron problem for given positions of the atomic nuclei, which create electrostatic potential acting on the electrons:

$$\begin{aligned} \hat{H}_{el}\Psi_{el}(\mathbf{R}, \mathbf{r}) &= E_{el}(\mathbf{R})\Psi_{el}(\mathbf{R}, \mathbf{r}), \text{ where} \\ \hat{H}_{el} &= \sum_{i=1}^N \left[-\frac{\hbar^2}{2m} \nabla_i^2 + \frac{1}{2} \sum_{j \neq i}^N \frac{e^2}{|\mathbf{r}_i - \mathbf{r}_j|} + \sum_{n=1}^{N_{\text{at}}} \frac{e^2 Z_n}{|\mathbf{r}_i - \mathbf{R}_n|} \right] + V_{nn}. \end{aligned} \quad (3.4)$$

The nucleus-nucleus interaction V_{nn} is included in the electron problem as a positive constant, which gives an important contribution to the total energy of the many-particle system. The nuclei create a positively charged background that compensates for the negative charge of all electrons and prevents the electrostatic energy of the whole crystal to diverge with its volume.

The electronic energy $E_{el}(\mathbf{R})$, which includes parametrically the crystal structure, is added to the nuclei part of the Hamiltonian to obtain the Schrödinger equation for the crystal lattice:

$$\left[\hat{H}_n + E_{el}(\mathbf{R}) \right] \Psi_n(\mathbf{R}, Q) = E(Q)\Psi_n(\mathbf{R}, Q), \quad (3.5)$$

where Q is a set of quantum numbers that characterize the state of the whole system.

Even in the adiabatic approximation, the energy state of electrons has an influence on the motion and bonding of the nuclei¹. Moreover, the quantum-mechanical problem

¹Some terms that were omitted in this approximation and which are of the order of $m/M_n \sim 10^{-3}$ could be essential for the electron-phonon coupling and the superconducting properties [81].

defined by the electronic Hamiltonian

$$\hat{H} = \sum_{i=1}^N \left[-\frac{\hbar^2}{2m} \nabla_i^2 + V(\mathbf{r}_i) + \frac{1}{2} \sum_{j \neq i}^N \frac{e^2}{|\mathbf{r}_i - \mathbf{r}_j|} \right] \quad (3.6)$$

with the external potential $V(\mathbf{r}_i)$ created by the nuclei is still quite complicated to be solved straightforwardly. The first considerable progress in this respect should be regarded to the Hartree-Fock (HF) approximation [81, 82], which set the basic ingredients for the latter formulated density functional theory. It is convenient to formulate the HF theory starting from the variational principle for the total energy of the many-body system:

$$E = \frac{\langle \Psi | \hat{H} | \Psi \rangle}{\langle \Psi | \Psi \rangle}. \quad (3.7)$$

One can prove that the ground-state wavefunction $|\Psi\rangle_0$ minimizes the functional (3.7) and the latter takes the value of the ground state energy. In the HF approach, the exact solution $|\Psi\rangle_0$ is approximated by a wavefunction that reflects the correct symmetry postulated by the Pauli exclusion principle. The approximate wavefunction can then be constructed as a Slater determinant of single-particle wavefunctions $|\psi_i\rangle$. The total energy of the system is, therefore, a functional of $|\psi_i\rangle$. By applying the Euler-Lagrange method to account for the normalization of the wavefunction one can reduce the aforementioned minimization problem to a set of single-particle equations:

$$\left[-\frac{\hbar^2}{2m} \nabla^2 + V_{\text{eff}}(\mathbf{r}) \right] \psi_i(\mathbf{r}) = \varepsilon_i \psi_i(\mathbf{r}), \quad i = 1..N \quad (3.8)$$

with the effective potential

$$\begin{aligned} V_{\text{eff}}(\mathbf{r}) &= V(\mathbf{r}) + V_H(\mathbf{r}) + V_{\text{ex}}(\mathbf{r}) = \\ &= V(\mathbf{r}) + |e| \int \frac{\rho(\mathbf{r}')}{|\mathbf{r} - \mathbf{r}'|} d\mathbf{r}' - |e| \int \frac{\rho_{\text{ex}}(\mathbf{r}, \mathbf{r}')}{|\mathbf{r} - \mathbf{r}'|} d\mathbf{r}' \end{aligned} \quad (3.9)$$

containing three contributions:

- $V(\mathbf{r})$ – the electrostatic potential of the nuclei,
- $V_H(\mathbf{r})$ – the Hartree potential for the electron distribution with density $\rho(\mathbf{r})$,
- $V_{\text{ex}}(\mathbf{r})$ – the exchange energy with the corresponding exchange hole $\rho_{\text{ex}}(\mathbf{r}, \mathbf{r}')$.

The Hartree term is a characteristic feature of the effective potential approaches to many-body systems and represents the electrostatic energy of the electronic charge distribution. The HF theory has an inherent problem that stems from the long-range character of the Coulomb potential. This leads to logarithmic singularities in the HF eigenvalues as functions of the wave-vector. The latter manifests itself in observed contradictions of theory with experimental data on free-electron bandwidth and specific heat of metals [81]. It goes without saying that the electronic correlations are completely neglected in equations (3.8) which originates in the initial approximation for the N -electron wavefunction.

Although the Hartree-Fock theory was not successful in explaining the properties of even simple metals, it provided a solid background and a good starting point for

the latter theories. The Hartree-Fock theory introduced for the first time the concept of the exchange hole $\rho_{\text{ex}}(\mathbf{r}, \mathbf{r}')$ which depicts the well-known fact that two electrons cannot occupy the same quantum state. The generalization of this concept – the exchange-correlation hole – plays a central role in the density functional theory [82–84] and determines all the variety of electronic correlation effects in condensed matter.

3.1.2 Kohn-Sham equations

The main “subterfuge” of the HF theory is the mapping of the sophisticated many-body problem onto a set of single-particle equations with some effective potential. This approach has been extended and revised in the density functional theory formulated by Hohenberg and Kohn [85] and later by Kohn and Sham [86]. The first observation is that the full wavefunction $\Psi(\{\mathbf{r}_i\})$ of N interacting electrons, although containing in principle all information about the system, is in most cases superfluous and not needed. Therefore, the evaluation of $\Psi(\{\mathbf{r}_i\})$ can be circumvented by resorting to the ground-state electronic density, which is derived from the full wavefunction by integrating over all electronic coordinates except for those of one electron

$$n(\mathbf{r}) = \int d\mathbf{r}_2 \dots \int d\mathbf{r}_N |\Psi(\mathbf{r}, \mathbf{r}_2 \dots \mathbf{r}_N)|^2. \quad (3.10)$$

In the original papers of Hohenberg and Kohn [85], two important theorems have been formulated²:

Theorem 1. *The total energy is a functional $E[n]$ of the electronic density $n(\mathbf{r})$.*

Theorem 2. *The functional $E[n]$ is minimized by the ground-state density $n_0(\mathbf{r})$ and its minimum corresponds to the ground-state energy E_0 .*

The aforementioned functional of the total energy can be written in the following form:

$$E[n] = F[n] + \int n(\mathbf{r})V(\mathbf{r})d\mathbf{r}. \quad (3.11)$$

The functional $F[n]$ appearing here does not depend on the potential $V(\mathbf{r})$ of the nuclei and, therefore, it is universal for all atomic structures. Three different contributions are included in this functional:

$$F[n] = T[n] + \iint \frac{n(\mathbf{r})n(\mathbf{r}')}{|\mathbf{r} - \mathbf{r}'|} d\mathbf{r} d\mathbf{r}' + \tilde{E}_{\text{xc}}[n]. \quad (3.12)$$

The first term is the kinetic energy functional $T[n]$ of the interacting electrons; the second one – Hartree energy V_{H} – was mentioned earlier in this chapter and the last term is the exchange-correlation energy $\tilde{E}_{\text{xc}}[n]$. Here, the kinetic energy $T[n]$ can be split into two terms: the kinetic energy $T_0[n]$ of non-interacting particles and the missing contribution T_{xc} of the electronic correlations. The latter can be combined with the third term $\tilde{E}_{\text{xc}}[n]$ to form the total exchange-correlation functional $E_{\text{xc}}[n]$. The main statement of the density functional theory says: *if the exact form of the exchange-correlation functional $E_{\text{xc}}[n]$ is known, then the calculated properties of the ground state are in principle exact.* Unfortunately this functional is not known so far and, in

²The mathematical intricacies involved in the consistent proof of these statements will not be addressed in this thesis.

practical cases, one needs to use an appropriate approximation. It is then postulated that the many-body system can be mapped onto an effective single-particle problem using the *Kohn-Sham (KS) ansatz* with the electronic density defined as follows:

$$n(\mathbf{r}) = \sum_{i=1}^N |\varphi_i(\mathbf{r})|^2. \quad (3.13)$$

Applying the condition that the density $n(\mathbf{r})$ obtained from single-particle wavefunctions $\varphi_i(\mathbf{r})$ minimizes the total energy functional (3.11), one can derive a general expression for the effective single-particle potential $v_{\text{eff}}(\mathbf{r})$:

$$v_{\text{eff}}(\mathbf{r}) = V(\mathbf{r}) + 2 \int \frac{n(\mathbf{r}')}{|\mathbf{r} - \mathbf{r}'|} d\mathbf{r}' + v_{\text{xc}}(\mathbf{r}) \quad (3.14)$$

which enters the *Kohn-Sham equations* [86]³

$$[-\nabla^2 + v_{\text{eff}}(\mathbf{r}) - \varepsilon_i] \varphi_i(\mathbf{r}) = 0. \quad (3.15)$$

The quantum problem defined by the set of equations (3.13), (3.14) and (3.15) forms the basis of the *density functional theory*. Solution of the KS equations in terms of one-electron orbitals $\varphi_i(\mathbf{r})$ gives all necessary information on the total energy functional:

$$E[n] = - \sum_{i=1}^N \int \varphi_i^*(\mathbf{r}) \nabla^2 \varphi_i(\mathbf{r}) d\mathbf{r} + \iint \frac{n(\mathbf{r})n(\mathbf{r}')}{|\mathbf{r} - \mathbf{r}'|} d\mathbf{r} d\mathbf{r}' + E_{\text{xc}}[n]. \quad (3.16)$$

The first two terms describe the single-particle contribution to the energy. All correlation effects are contained within the exchange-correlation functional $E_{\text{xc}}[n]$ which, in all real calculations, has to be approximated. Success or failure of the density functional theory in explaining and describing electronic phenomena in solids depend largely on the quality of the chosen approximation for the exchange-correlation energy.

The DFT formalism can be extended for spin-polarized electron systems with magnetic ordering by introducing electron wavefunctions with two components, each corresponding to a different spin quantum number. In this work, only collinear magnetism will be considered, so that each spin channel is characterized by its own charge density ($n_+(\mathbf{r})$ for the spin-up and $n_-(\mathbf{r})$ for the spin-down states). The total charge density $n(\mathbf{r}) = n_+(\mathbf{r}) + n_-(\mathbf{r})$ in the energy functional (3.16) becomes augmented by the magnetization density $\mathbf{m}(\mathbf{r}) = n_+(\mathbf{r}) - n_-(\mathbf{r})$. The KS equations (3.15) turn now into a set of decoupled equations for each spin component where the exchange-correlation potential $v_{\text{xc}}(\mathbf{r})$, being a part of the effective potential (3.14), is different for the two spin components. It makes sense to think of the spin-dependence of the exchange-correlation functional in terms of an effective internal magnetic field [81]:

$$\mathbf{B}_{\text{xc}}(\mathbf{r}) = - \frac{\partial E_{\text{xc}}(n, \mathbf{m})}{\partial \mathbf{m}(\mathbf{r})}. \quad (3.17)$$

With this additional magnetic field intrinsic to the electronic subsystem, the Kohn-Sham equations are reformulated as Pauli-like equations:

$$[T + v_{\text{ext}}(\mathbf{r}) + V_H(\mathbf{r}) + V_{\text{xc}}(\mathbf{r}) - \mathbf{B}_{\text{xc}}(\mathbf{r}) \cdot \boldsymbol{\sigma}] \varphi_{i,\sigma}(\mathbf{r}) = \varepsilon_i \varphi_{i,\sigma}(\mathbf{r}), \quad (3.18)$$

³In contrast to (3.8), atomic units are used here and further on in the text to simplify the notations.

where $V_{xc}(\mathbf{r})$ describes the spin-independent part of the exchange-correlation energy, and σ is the spin quantum number. For many ferromagnetic materials, the spin dependence of the exchange-correlation potential can be represented in terms of exchange splitting between the spin-up and spin-down states. Large exchange splitting favours spin-polarized solutions, while the kinetic energy term in the total energy opposes them⁴.

3.1.3 Common approximations in DFT

The main idea of the density functional theory is the replacement of the sophisticated many-body quantum mechanical problem with an effective single-particle problem, all many-body correlation effects being included in the exchange-correlation functional $E_{xc}[n]$. Since the exact expression for $E_{xc}[n]$ is unknown so far, the eventual applicability of the Kohn-Sham theory depends largely on the quality of the approximate functional describing the electronic correlations. Further on, I will briefly discuss different approximation schemes that are nowadays widely used in the community and compare their qualities in relation with experiment.

Among the first and most widely used schemes is the local-density approximation (LDA) and its natural descendants: local spin-density approximation (LSDA) [87, 88] and LDA+U approach [89, 90] (Hubbard model for strongly correlated electronic states).

In LDA, the exchange-correlation potential is local and the corresponding energy has the form:

$$E_{xc}[n] = \int n(\mathbf{r})\epsilon_{xc}(n(\mathbf{r}))d\mathbf{r}, \quad (3.19)$$

where $\epsilon_{xc}(n(\mathbf{r}))$ is calculated as the exchange-correlation energy for the uniform electron gas with the electron density equal to the local value $n = n(\mathbf{r})$ at a certain point \mathbf{r} in space. From the definition of the exchange-correlation potential, one obtains:

$$v_{xc}(\mathbf{r}) = \left\{ \frac{d}{dn} [n\epsilon_{xc}(n)] \right\} \Big|_{n=n(\mathbf{r})} = \epsilon_{xc}(n) + n \frac{d\epsilon_{xc}(n)}{dn}. \quad (3.20)$$

Both expressions (3.19) and (3.20) are straightforwardly generalized for the collinear spin-polarized case, defining thereby the local spin-density approximation:

$$E_{xc}[n] = \int n(\mathbf{r})\epsilon_{xc}(n_+(\mathbf{r}), n_-(\mathbf{r}))d\mathbf{r} \quad (3.21)$$

$$v_{\sigma}^{xc}(\mathbf{r}) = \left\{ \frac{\partial}{\partial n_{\sigma}} [n\epsilon_{xc}(n_+, n_-)] \right\} \Big|_{n_{\sigma}=n_{\sigma}(\mathbf{r})} \quad (3.22)$$

In LSDA, the exchange-correlation energy of a spin-polarized uniform electron gas is needed. Although there is no exact expression for that quantity, it can be obtained numerically with a very high accuracy⁵ [91–93]. To make the scheme most effective one uses a parametrization for the exchange-correlation energy which embodies the results of quantum Monte Carlo simulations. The most important parametrization

⁴This aspect of spin-polarized systems has been already mentioned in chapter 2 as a part of the Stoner model applied to magnetic oxides.

⁵The exchange-correlation density and the corresponding potential are, in this case, *functions* rather than functionals of density.

schemes are that of Janak, Moruzzi and Williams [91], Vosko [92], and Perdew and Wang [93]. There is a vast literature on these and related matters, so I make here only some general remarks on the L(S)DA approach. At first glance, it seems natural that the theory should provide good results for systems close to nearly free electron gases (e.g. simple metals), whereas it should severely fail for more complex systems with a rapidly varying electron density. For one thing, the non-local interaction effects are not taken into account in LDA and, for another, there is still some spurious uncompensated self-interaction, which delocalizes electrons. The most surprising fact is that the LDA method appears to be relatively successful in a great number of cases, where it should fail. Although strongly correlated systems still remain a great challenge for theory and require other methods than the simple LDA, the huge success of the latter in the description of the electronic and magnetic properties of a large class of materials cannot be ignored.

The next natural step in improving the exchange-correlation functional is a systematic expansion in terms of the density and its derivatives starting from the LSDA expression:

$$E_{\text{xc}}[n_+, n_-] = E_{\text{xc}}^{\text{LSDA}}[n_+, n_-] + \sum_{\sigma, \sigma'} \int C_{\text{xc}}^{\sigma, \sigma'}(n_+, n_-) \frac{\nabla n_{\sigma}}{n_{\sigma}^{2/3}} \frac{\nabla n_{\sigma'}}{n_{\sigma'}^{2/3}} d\mathbf{r} + \dots, \quad (3.23)$$

where the expansion coefficients $C_{\text{xc}}^{\sigma, \sigma'}$ define the gradient corrections to the exchange-correlation energy.

Unfortunately, even expansions with high-order terms do not provide any considerable improvement upon the standard LSDA and, in most cases, give less accurate results compared to the experiment. The reason for this peculiar behaviour lies in the violation of certain sum rules [83] by the expression (3.23). In the LDA method, these rules are satisfied, because the LDA functional is constructed from the exact Hamiltonian of a real physical system (homogeneous electron gas). Moreover, the gradient of the density cannot be considered, in most real systems, as a small parameter in expansion (3.23), and, therefore, the sum over all terms in this expansion is not necessarily diverging. Taking into account some general functional properties of the exchange-correlation energy and considering a certain parametrization of this energy, Perdew et al. [94] proposed the *generalized-gradient approximation* (GGA):

$$E_{\text{xc}}^{\text{GGA}}[n_+, n_-] = \int n(\mathbf{r}) \epsilon_x^P(r_S) F_{\text{xc}}(r_S, \zeta, s) d\mathbf{r}, \quad (3.24)$$

where $\epsilon_x^P(r_S)$ denotes the exchange energy per particle of the non-polarized uniform electron gas, $F_{\text{xc}}(r_S, \zeta, s)$ is called the enhancement factor which includes the density parameter $r_S \sim 1/n$, a measure of its variation $s \sim \nabla r_S$ and the local spin polarization $\zeta = (n_+ - n_-)/(n_+ + n_-)$. I am not going to run into details here, as to how the derivation of the factor F_{xc} proceeds. Nevertheless, it should be mentioned that the GGA construction is not unique, and a comparison between theory and experiment has to be made to determine the accuracy of the chosen functional.

Numerous studies presented in literature have shown that, in some cases, the GGA provides an improvement over the LDA, which is due to a better description of the non-local character of electronic correlations. Though a general feature of virtually all GGA functionals applied to solids is their tendency to overestimation of the lattice constant with respect to the experimental value (the so-called underbinding problem), whereas LDA-based calculations usually lead to overbinding and smaller lattice volumes. This

might become a serious problem for ferroelectric materials, where even a small deviation from the actual equilibrium volume can destroy the ferroelectric instability. To deal with such situations one might resort to the so-called *hybrid functionals* [95] that are formulated as a mixture of LDA and Hartree-Fock functionals. In this procedure, a portion of the exact HF exchange is added to the corresponding term of the LDA expression. With a hybrid functional obtained in such a way one can achieve a better agreement between the calculated and experimental values of the equilibrium volume. The common problem of such functionals is the lack of clarity, as to how the mixing parameter should be chosen in each particular case.

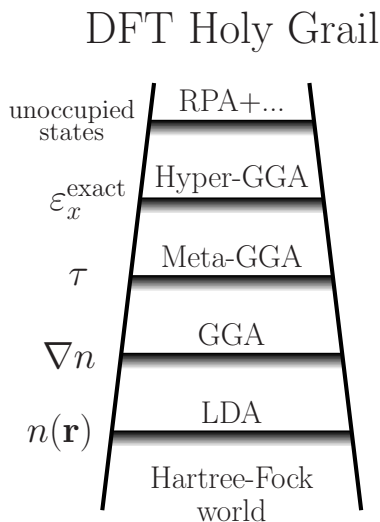


Figure 3.1: Jacob’s ladder of hierarchy of different exchange-correlation functionals. Important quantities characterizing the approximations are shown on the left side. The quality of approximation increases towards the upper steps of the ladder.

has exceeded well over several thousands – so many different functionals are now available for numerical simulations. The subtle question, as to which functional should be used in each particular case, requires an extensive testing procedure which is usually bound to large computational costs. The future perspectives of DFT in comparison to other first-principle approaches to the many-body electron problem are discussed in the recent paper of K. Burke [99].

3.1.4 LDA+U method

The main criticism of the standard LSDA approach is constituted in its inability to properly describe the wide variety of magnetic insulators and, in particular, Mott-Hubbard metal-insulator transition. The latter is a well-known phenomenon in strongly correlated electron systems, such as transition metal oxides with partially filled d and f orbitals. For these compounds, the LSDA method fails not only to predict the correct value of the fundamental band gap, but also to describe the ground state magnetic

In strongly correlated systems one might need to resort to different approaches, such as semi-empirical LDA+U method [89, 90, 96], where certain states are “manually” localized by introducing an additional repulsive Coulomb energy U on the corresponding atomic sites. In solids, where d and f elements determine the physical properties, corrections to self-interaction energy for localized states [97] and, possibly, inclusion of relativistic effects and the spin-orbit coupling might be needed as well. Another important issue is the correct treatment of band gaps in insulators that might require the use of exact-exchange functionals [98].

On the way of improving the exchange-correlation (XC) functional one strives for “including” as many corrections and effects as only possible to better describe the nature. This process is traditionally depicted by Jacob’s ladder⁶ (Fig. 3.1), where the functionals of higher complexity and precision reside on higher steps tending towards the Holy Grail of DFT – the exact XC-energy functional. Meanwhile, the actual number of sub-steps and sideways on this road

⁶The figure presented here was adapted from the talk “Basics of DFT” of K. Burke and L. Wagner during the ELK-2011 conference.

properties. This should not be surprising, since LSDA is a mean-field theory, where the spin dependence of the total energy comes from the exchange splitting related to Hund's-rule exchange. The typical value of the corresponding exchange energy is of the order of 1 eV, which is apparently insufficient for the understanding of strongly localized d and f states. In this respect, the LDA+U method is an amalgamation of two approaches to the electron problem that, on the one hand, includes strong intra-atomic repulsion between the opposite spins on the same site (similar to the Hubbard model) and, on the other hand, conserves the "band-approach" character of the theory [89, 90, 96].

In the LDA+U method, orbital-dependent Hartree-Fock exchange energy and the double-counting term are added to the LDA expression for the total energy:

$$E_{\text{LDA+U}}(n, \hat{n}) = E_{\text{LDA}}(n, \hat{n}) + E_{\text{HF}}(\hat{n}) - E_{dc}(\hat{n}). \quad (3.25)$$

The rotationally invariant Hartree-Fock-like part $E_{\text{HF}}(\hat{n})$ introduced by Liechtenstein et al. [90] has the following form:

$$E_{\text{HF}}(\hat{n}) = \frac{1}{2} \sum_{\gamma} (U_{\gamma_1\gamma_3\gamma_2\gamma_4} - U_{\gamma_1\gamma_3\gamma_4\gamma_2}) \hat{n}_{\gamma_1\gamma_2} \hat{n}_{\gamma_3\gamma_4}, \quad (3.26)$$

where $\hat{n}_{\gamma_1\gamma_2}$ are orbital-dependent on-site occupancies and index γ contains orbital and spin quantum numbers. The matrix elements $U_{\{\gamma\}}$ describe the unscreened on-site electron-electron interaction. In solids, however, the Coulomb interaction is screened and its self-consistent calculation is rather computationally demanding and not always feasible. For that reason, these matrix elements are often expressed in terms of two empirical parameters U and J , which are adjusted to fit the calculated values to experimental data, e.g. for magnetic moments, band gaps, equilibrium volume, structure etc. In terms of these parameters, the last term in (3.25), which accounts for double counting, can be rewritten

$$E_{dc}(\hat{n}) = \frac{U}{2} \hat{n}_{\text{tot}} (\hat{n}_{\text{tot}} - 1) - \frac{J}{2} \sum_{\sigma=+,-} \hat{n}_{\text{tot}}^{\sigma} (\hat{n}_{\text{tot}}^{\sigma} - 1). \quad (3.27)$$

Another widely used formulation of the LDA+U theory, which will be applied throughout this work, has been introduced by Dudarev et al. [96] by defining the orbital-dependent energy:

$$E_{\text{LDA+U}} = E_{\text{LDA}} + \frac{(U - J)}{2} \sum_{\sigma} \left[\left(\sum_{m_1} n_{m_1, m_1}^{\sigma} \right) - \left(\sum_{m_1, m_2} \hat{n}_{m_1, m_2}^{\sigma} \hat{n}_{m_2, m_1}^{\sigma} \right) \right]. \quad (3.28)$$

By introducing additional Hubbard-like term in the total energy that depicts the Coulomb d - d (or f - f) interaction, one shifts the occupied d - (or f -) bands by $-U/2$ and the unoccupied bands by $+U/2$ on the energy scale. The exchange-correlation potential, which eventually enters the Kohn-Sham equations, becomes orbital-dependent and gives rise to aspherical charge densities on the corresponding sites. The LDA+U term adds an energy penalty for two electrons of opposite spin occupying the same orbital/site, which enforces the involved orbitals to be either empty or half-filled. This can be seen as a spin polarization induced by strong electronic correlations, which is, indeed, observed for rare-earth elements with open f -shells. In 3d transition metal oxides, the application of the LDA+U method enhances the magnetic moments and,

in certain cases, might open or significantly improve the fundamental band gap, which happens, for example, in NiO oxide.

Two expressions (3.25) and (3.28) reflect the Anderson-like approach to representing the Hamiltonian: on the one hand, there is a subspace of well localized orbitals (their interaction is described by Hubbard terms); on another hand, there is also a subspace of the delocalized states (usually, s - and p -states), for which the LDA method can be successfully applied. These two subspaces are treated simultaneously in the LDA+U method, an important factor being the relative energy position of the localized states with respect to the delocalized conduction bands. In the conventional LDA treatment, the separation between the bands is underestimated, which affects the magnetic properties of the ground state and leads to discrepancies between the predicted and measured XPS and BIS spectra. The LDA+U method is advantageous for understanding the basic physics of Mott-Hubbard insulating behavior in the family of transition metal oxides, where strong hybridization effects might arise as well. It should be mentioned that the LDA+U method depends much on the choice of the localized set of orbitals. However, in most cases, partially filled d and f orbitals are so much localized that they retain their atomic character and can be well represented by the superposition of atomic-like orbitals. In this respect, the method is most naturally realized in LMTO calculation schemes. Nevertheless, there are corresponding generalizations in terms of plane waves as well.

3.2 Pseudopotential plane-wave approach

3.2.1 Plane-wave expansion

To describe the physical properties of solids within DFT one needs to solve the Kohn-Sham equations (3.15) with an appropriate approximation for the exchange-correlation energy. In doing so, one can either solve differential equations directly or, more effectively, expand the wavefunctions using a complete basis set $\{\psi_i\}$. In the latter case, differential equations can be reduced to an equivalent set of algebraic problems of determining the eigenvalues and the eigenvectors of the Hamilton matrix.

For periodic solids, e.g. ideal crystals, there is a symmetry consideration that helps to simplify the original problem. The external potential created by the nuclei has the translational invariance symmetry coming from the crystal lattice, which makes the whole single-particle Hamiltonian (3.6) periodic in space. According to Bloch theorem (1929), the solutions of the original electron problem with this Hamiltonian as well as the Kohn-Sham equations (3.15) have a general property:

$$\varphi_{\mathbf{k}n}(\mathbf{r} + \mathbf{R}_j) = e^{i\mathbf{k}\cdot\mathbf{R}_j} \varphi_{\mathbf{k}n}(\mathbf{r}), \quad (3.29)$$

which is satisfied for an arbitrary lattice vector \mathbf{R}_j .

This theorem states that the translation by any lattice vector does not change the wavefunction except for the additional phase factor. The wave-vector \mathbf{k} is introduced here as a quantum number that characterizes the eigenstates $\varphi_{\mathbf{k}n}$ belonging to the n th band. If the electron wavefunction $\varphi_{\mathbf{k}n}$ was just a plane wave $\sim e^{i\mathbf{k}\mathbf{r}}$ propagating along a certain direction in the crystal, then the Bloch theorem would be a trivial consequence of the definition of a plane wave. However, due to a non-uniform crystal potential the real wavefunction is different from that of a free electron. Nevertheless, the existence of the aforementioned property (3.29) gives a hint that the wavefunction can be naturally expanded into different plane waves with appropriate amplitudes and phases. This idea is the basis of all plane-wave-based approaches to the Kohn-Sham problem and the corresponding expansion can be expressed as follows:

$$\varphi_{\mathbf{k}n}(\mathbf{r}) = \frac{1}{\sqrt{\Omega}} \sum_s a_{ns}(\mathbf{k}) e^{i(\mathbf{k}+\mathbf{G}_s)\cdot\mathbf{r}}, \quad (3.30)$$

where the sum runs over all reciprocal lattice vectors \mathbf{G}_s , Ω is the total volume of the system, and the expansion coefficients a_{ns} are normalized $\sum_s |a_{ns}(\mathbf{k})|^2 = 1$. In this Fourier series, each term represents a Bloch function, which satisfies (3.29), and, therefore, the whole wavefunction has this property.

Plane waves have several advantages as the basis functions in the Kohn-Sham problem for solids:

- The basis functions are orthogonal and normalized.
- They are independent of the atomic positions (unlike local atomic orbitals).
- They fulfil naturally periodic boundary conditions (PBC).
- The implementation of a plane-wave-based method is usually much simpler than for other basis sets. For example, the kinetic energy operator looks particularly

simple in this representation:

$$-\frac{1}{2}\nabla^2\varphi_{\mathbf{G}}(\mathbf{r}) = -\frac{1}{2}(i\mathbf{G})^2\frac{1}{\sqrt{V}}e^{i\mathbf{G}\mathbf{r}} = \frac{1}{2}G^2\varphi_{\mathbf{G}}(\mathbf{r}), \quad (3.31)$$

so that it is diagonal with the matrix elements $E_{\text{kin}}^{GG'} = (G^2/2)\delta_{GG'}$.

- The accuracy of the solution can be systematically increased by simply taking more plane waves. The infinitely large plane wave basis set is complete in a sense that every function can be represented as a weighted sum of functions from this set.

From the Bloch theorem it follows that the physical properties are also periodic in space, so that the quantum problem has to be solved only in a restricted region defined by the unit cell of the considered material. In the plane wave representation, this corresponds to the solution within the *Brillouin zone* (BZ). The latter is defined as Wigner-Seitz cell constructed on the reciprocal lattice vectors \mathbf{G}_s that satisfy

$$\mathbf{G}_s \cdot \mathbf{R}_j = 2\pi Z\delta_{sj}, \quad Z = 0, \pm 1, \pm 2\dots \quad (3.32)$$

The solution of the electronic problem in the BZ is a set of n bands with dispersion law $\varepsilon_n(\mathbf{k})$. Most physical properties are determined as a sum/integral over the Brillouin zone⁷, e.g. the density of states:

$$n(E) = \frac{\Omega_{\text{u.c.}}}{(2\pi)^3} \sum_n \int_{\text{BZ}} d\mathbf{k} \delta(E - \varepsilon_n(\mathbf{k})), \quad (3.33)$$

where the volume $\Omega_{\text{u.c.}}$ of the unit cell appears.

Using the plane-wave expansion (3.30), one can reduce the KS equations (3.15) to an algebraic problem represented by the following secular equation [81]:

$$\sum_{t,s} \{[(\mathbf{k} + \mathbf{G}_s)^2 - \varepsilon(\mathbf{k})] \delta_{st} + V(\mathbf{G}_t - \mathbf{G}_s)\} a_{ns}(\mathbf{k}) = 0. \quad (3.34)$$

The main tricky point about solving the formulated algebraic problem⁸, i.e. diagonalization of the matrix on the left-hand side of equation (3.34) and obtaining the eigenvalues as functions of \mathbf{k} , is the nature of the crystal potential $V(\mathbf{G}_t - \mathbf{G}_s)$. The latter is relatively smooth and weak in the interstitial region, whereas near the nuclei it changes drastically and cannot be considered as a small perturbation. For that reason, the electron wavefunction in the core region is rapidly oscillating and, consequently, a large number of plane waves is necessary to include in expansion (3.30), which requires large computational resources. Historically, first attempts to avoid these difficulties involved the construction of augmented wavefunctions that capture the rapid oscillations in the cores and include the effect of the smooth potential in the interstitial region. The most prominent examples are orthogonalized-plane-wave (OPW) and augmented-plane-wave (APW) methods [101], as well as the Green functions technique [102], which are now widely used and proved to be very effective. The Green function method will be addressed later on in this chapter, but for the moment it is necessary to consider another approach, which is more related to the spirit of plane waves – the pseudopotential approach.

⁷More information on the plane wave method can be found, for example, in the book of Richard Martin [100].

⁸The summation in (3.34) runs over the sites of the reciprocal lattice.

3.2.2 Core states and pseudopotentials

The main idea of the pseudopotential (PP) method is the replacement of the original electron wavefunction in the core region by a smoother function that can be represented by a moderate number of planewaves. At the same time, the wavefunction of the valence electrons outside the cores should be reproduced as accurately as possible. According to the transformation procedure suggested by Phillips, Kleinman and Antoncik (PKA) [103, 104], the pseudo-wavefunction, defined in this manner, satisfies a Schrödinger-like equation with an additional contribution to the potential coming from the core states (for review, see [101]). It is worth going now through the main steps of the PKA pseudopotential derivation.

Following the concept of a pseudopotential, one can represent the electron wavefunction $\varphi_n^v(\mathbf{r})$ of the valence states as the sum of the smooth pseudo-wavefunction $\varphi_n^{\text{ps}}(\mathbf{r})$ and a superposition of the core states $|c_m\rangle$:

$$\varphi_n^v(\mathbf{r}) = \varphi_n^{\text{ps}}(\mathbf{r}) + \sum_m b_m |c_m\rangle, \quad (3.35)$$

where n and m denote the corresponding band indices; the core states $|c_m\rangle$ are the lowest eigenstates of the studied Hamiltonian.

By substituting representation (3.35) into the Schrödinger equation for the valence wavefunction

$$[-\nabla^2 + V_{\text{eff}}(\mathbf{r})] \varphi_n^v(\mathbf{r}) = \varepsilon_n \varphi_n^v(\mathbf{r}), \quad (3.36)$$

one obtains a similar equation for the smooth part $\varphi_n^{\text{ps}}(\mathbf{r})$, however, with a different potential

$$\hat{V}^{\text{ps}} = V_{\text{eff}}(\mathbf{r}) + \hat{V}_{\text{NL}}, \quad (3.37)$$

where \hat{V}_{NL} is a non-local operator acting as a strongly repulsive potential. In the real-space representation it reads:

$$\hat{V}_{\text{NL}} \varphi_n^{\text{ps}}(\mathbf{r}) = \sum_m (\varepsilon_n^v - \varepsilon_m^c) \langle \mathbf{r} | c_m \rangle \langle c_m | \varphi_n^{\text{ps}} \rangle, \quad (3.38)$$

where the summation runs over the core states with the energies ε_m^c .

If we assume that the core states are localized in a sphere with the radius r_c around each atom, then the non-local part \hat{V}_{NL} contributes only within the core region and the pseudopotential differs from the original Coulomb potential only inside the spheres. Beyond the boundary $r = r_c$ the core states vanish and the effective potential equals $V_{\text{eff}}(\mathbf{r})$. Repulsive character of the additional potential \hat{V}_{NL} follows from the obvious relation $(\varepsilon_i^v - \varepsilon_j^c) > 0$. For that reason, the pseudopotential \hat{V}^{ps} is generally much weaker than the original one ($V_{\text{eff}}(\mathbf{r})$). This statement was formulated as the ‘‘cancellation theorem’’ by Cohen and Heine [105]. On the other hand, the new potential in the KS problem is now a complicated non-local operator that depends also on the core states. However, due to the non-unique character of the pseudopotential construction one can

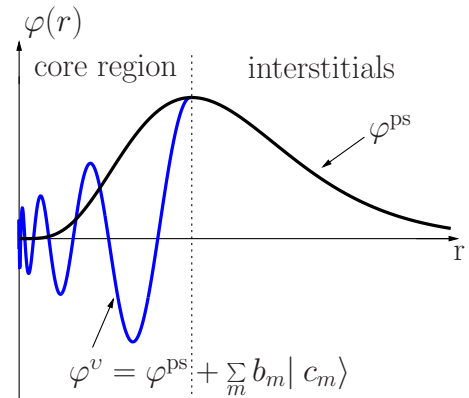


Figure 3.2: Schematic representation of the electron wavefunction near an atom in a solid. Rapidly oscillating wavefunction in the core region is replaced by a smooth function which, at the same time, reproduces accurately the true electron solution in the interstitials.

make \hat{V}^{ps} relatively smooth. The requirement is that the new potential reproduces the scattering properties (phase shifts and amplitudes) of the original one in the chosen energy range.

The advantage of working with a pseudopotential in plane-wave-based methods relates to the smooth spatial behaviour of the potential operators, which can be, therefore, represented by a reasonable number of plane waves. According to the PKA equation (3.36), the electronic bands are determined by the smooth pseudo-wavefunction $\varphi^{\text{ps}}(\mathbf{r})$. Moreover, the whole valence wavefunction $\varphi^v(\mathbf{r})$ can be restored from the pseudo-wavefunction by means of a linear transformation $\varphi^v = \hat{T}\varphi^{\text{ps}}$. In the next paragraph, I will discuss how this idea is used in the projector-augmented wavefunction approach.

The quality of a pseudopotential depends on its softness, transferability and accuracy. The transferability and softness are determined mostly by the radius of the core sphere and usually play against each other. The accuracy of a particular pseudopotential could be judged on by inspecting the calculated valence charge density and comparing it with the results of an all-electron calculation. An appropriate choice of the core configuration is important in reaching high accuracy in PP calculations. It is implied that the core states remain unchanged in the solid compared to the isolated atom, for which the pseudopotential was generated, not to mention that the cores of the neighboring atoms should not overlap at any studied conditions. However, it is not trivial to predict which states possess such “robustness” and in each particular case a number of tests should be made to decide on that.

There are several big families of pseudopotentials that are widely used in the DFT calculations. We shall be mostly interested in the following ones:

- norm-conserving (NC) pseudopotentials [106]
- ultrasoft (US) pseudopotentials [107]
- projector-augmented-wave (PAW) pseudopotentials [108]

The concept of norm-conservation was an important step in achieving the necessary qualities that pseudopotentials need to have. The pseudo-wavefunction/potential is required to coincide with the actual one outside the core region. Inside the core region ($r < r_c$) it can be different but the norm has to be conserved:

$$\int_0^{r_c} |\varphi_n^{\text{ps}}(\mathbf{r})|^2 r^2 dr = \int_0^{r_c} |\varphi_n^v(r)|^2 r^2 dr. \quad (3.39)$$

The Bachelet-Hamann-Schluter procedure is nowadays commonly used for the generation of norm-conserving pseudopotentials suited for practical calculations. It starts with a choice of an atomic reference configuration and core radii. Then an atomic calculation is performed and the all-electron atomic potential is generated. Afterwards, the latter is replaced by a constant value inside the core region, so that the lowest lying solution of the radial Schrödinger equation has the same eigenvalue as the atomic valence state. The wavefunction is corrected to include the norm conservation. The so-defined pseudo-wavefunction $\varphi^{\text{ps}}(\mathbf{r})$ is used to obtain the screened pseudopotential by the numerical inversion of the Schrödinger equation. Finally, unscreening procedure is applied to remove the Hartree and the exchange-correlation contributions coming from the total valence pseudocharge. This procedure allows, in principle, the tabulation of

a pseudopotential for the further use in *ab initio* calculations, so that these two tasks become separated. At the end, the accuracy of calculations depends on the quality of the generated pseudopotential, which should be tested by comparing the energy eigenvalues and the wavefunctions obtained within all-electron and pseudopotential calculations on single atoms with different core configurations.

Another family of pseudopotentials – ultrasoft pseudopotentials proposed by Vanderbilt and co-workers [107] – relies on the idea of making a pseudopotential as soft as possible to reduce the number of plane waves and, thereby, increase the convergence with respect to the plane-wave cut-off energy. However, since the norm conservation condition is omitted here, a number of complications arise. Namely, there is a non-trivial and non-diagonal overlap entering the secular equation (3.34) and, moreover, the charge density cannot be calculated simply by evaluating $\sum_n |\varphi_n(\mathbf{r})|^2$, as this will give a wrong value for the total charge. For that reason, an augmentation term has to be added to the wavefunction in the core region. The general problem is, the obtained pseudopotential might be less transferable than a similar PP with the norm conservation. On the other hand, the cost of generating a US potential is sufficiently small, so that it is possible to refine the pseudopotential during the calculation as the electronic configuration converges.

To summarize, norm-conserving pseudopotentials are, in principle, semi-local and, therefore, require high computational power, but, the price being paid, they provide higher accuracy. In contrast to this, ultrasoft pseudopotentials are computationally less demanding but show complications with the implementation and the transferability.

3.2.3 Projector-augmented waves

The conventional way of treating highly oscillating core states is to expand the solution of the all-electron problem in terms of smooth wavefunctions for the interstitials and auxiliary localized functions for the core regions. This is the starting point in many pseudopotential schemes. The projector-augmented waves (PAW) approach [108] is, in this respect, a generalized scheme for the reformulation of the electronic structure equations (3.15) and making its solution feasible with modern numerical techniques. It combines the advantages of the other pseudopotential approaches and allows for additional flexibility. However, the PAW method is different from its ancestors, since the full all-electron wavefunction can be restored at any point of the calculation using a linear transformation \hat{T} applied to the smooth pseudo-wavefunction.

Within each atomic sphere, both all-electron wavefunction φ^v and its smooth part φ^{ps} can be expanded in partial waves ψ_m^v and ψ_m^{ps} :

$$\varphi^v = \sum_m c_m \psi_m^v, \quad \varphi^{\text{ps}} = \sum_m c_m \psi_m^{\text{ps}}, \quad (3.40)$$

so that the full all-electron wavefunction is expressed as follows:

$$\varphi^v = \varphi^{\text{ps}} + \sum_m c_m (\psi_m^v - \psi_m^{\text{ps}}). \quad (3.41)$$

At the next step, biorthogonal projectors $|\tilde{p}_m\rangle$ are introduced that give the coefficients $c_m = \langle \tilde{p}_m | \psi_m^{\text{ps}} \rangle$ in each sphere. This allows to generalize the linear transformation \hat{T} as a sum of non-overlapping atom-centered contributions:

$$\hat{T} = 1 + \sum_m (\varphi_m^v - \varphi_m^{\text{ps}}) \langle \tilde{p}_m |. \quad (3.42)$$

Knowing the form of the transformation \hat{T} and the appropriate projectors, one can write, for any all-electron operator \hat{A} , the corresponding operator $\hat{A}^{\text{ps}} = \hat{T}\hat{A}\hat{T}$ that acts only on the smooth part of the full wavefunction. This transformation offers a degree of flexibility in a sense that particular terms can be added to it without changing the expectation value of the quantity represented by the original operator \hat{A} . One of the applications of this property relates to “polishing” the Coulomb singularities near the nuclei in order to simplify the numerical solution of the electronic problem. Similarly to alternative pseudopotential approaches, one can express the total electron density as the sum of the usual term (3.13) with the smooth wavefunctions φ_m^{ps} and the additional augmentation part. The latter comes from the localized contributions in the core regions and is calculated routinely as integrals in spherical coordinates. The implementation aspects of the PAW method are largely the same as for the other pseudopotential-based methods, especially, the ultrasoft formulations [100]. On the other hand, the PAW approach makes it possible to generate more accurate and transferable pseudopotentials without considerably increasing the computational cost of the calculations.

3.2.4 Structural optimization

In DFT calculations of the ground-state properties the knowledge of the equilibrium structure is of huge importance. The standard procedure for optimizing the lattice structure and the atomic positions in the unit cell can be split into the following steps⁹:

1. Crystal lattice with a certain symmetry and atomic bases is assumed for the studied compound.
2. The total energy is calculated for different volumes of the unit cell. At this step, full structural relaxation of the internal atomic positions is performed for the fixed volume and the lattice vectors and, subsequently, the total electronic energy is estimated using the tetrahedron method [109] for the integration over the volume of the BZ.
3. The resulting total energy vs. the lattice volume dependence is fitted to the Murnaghan equation of state [110] in order to estimate the equilibrium volume.
4. Finally, the atomic positions are optimized for the equilibrium volume.

This procedure has become customary and widely accepted, since it provides reliable and accurate results and avoids many numerical problems that are inherent to other structural optimization methods. As the structural optimization is frequently used in the present work, let us consider in more detail the basic steps described above.

At each step of optimization, the ionic forces $\{\mathbf{F}_i\}$ can be evaluated from the self-consistent electronic solutions according to the *Hellmann-Feynman theorem* [111]. In the Born-Oppenheimer approximation, the electronic Hamiltonian depends parametrically on the positions of the nuclei $\{\mathbf{R}_i\}$ and, therefore, the ionic forces can be defined

⁹In the following, we consider only solids at zero temperature and zero pressure.

through the first derivatives of the total energy E_{tot} with respect to the nuclei positions $\{\mathbf{R}_i\}$:

$$\mathbf{F}_i = -\frac{\partial E_{\text{tot}}}{\partial \mathbf{R}_i}. \quad (3.43)$$

Here, the total energy is the expectation value of the Hamiltonian with the wavefunctions $|\Psi_m\rangle$ that are solutions to the ground-state many-body problem¹⁰:

$$E_{\text{tot}}(\{\mathbf{R}_i\}) = \sum_m \langle \Psi_m | \hat{H}(\{\mathbf{R}_i\}) | \Psi_m \rangle. \quad (3.44)$$

In this expression, the most general form of the electron wavefunction $|\Psi_m\rangle$ is used, and, in this context, it has nothing to do with the Kohn-Sham orbitals. Taking into account the conservation of the norm of the wavefunctions $|\Psi_m\rangle$ with respect to the nuclei motion ($\langle \Psi_m | \Psi_m \rangle = 1$), one can arrive at the expression for the partial derivatives (3.43). The Hellmann-Feynman theorem states that the ionic forces are calculated as the expectation values of these parametric derivatives of the Hamilton operator:

$$\mathbf{F}_i = -\frac{\partial E_{\text{tot}}}{\partial \mathbf{R}_i} = \sum_m \left\langle \Psi_m \left| \frac{\partial \hat{H}}{\partial \mathbf{R}_i} \right| \Psi_m \right\rangle. \quad (3.45)$$

With the ionic forces being known, one can optimize the atomic positions until the absolute values of the forces are lower than a certain threshold. The obtained structure corresponds, however, to a *local energy minimum*, which means that, in principle, there could exist other structures that have a lower energy. Unfortunately, there is no general method of finding the structure representing *the global minimum* and, therefore, comparison with experimental data should be done for each studied system. The same applies to the very first step of the aforementioned procedure, namely, assigning a symmetry group to the lattice. Unless there is a solid experimental background with reliable data on the symmetry properties of the studied lattice, different candidate-phases should be compared with each other and the structural optimization has to be performed for each of them separately. The structure with the lowest ground state energy should be considered then as a prediction for the investigated system.

Finally, a word should be said about Murnaghan's equation of state (EqS). The physical background of this universal EqS is the assumption of a linear dependence of the bulk modulus on pressure [110, 112]. For moderate values of strain relative to the equilibrium volume, this assumption holds approximately, which explains the applicability of this EqS to a wide range of materials, irrespective of the particular

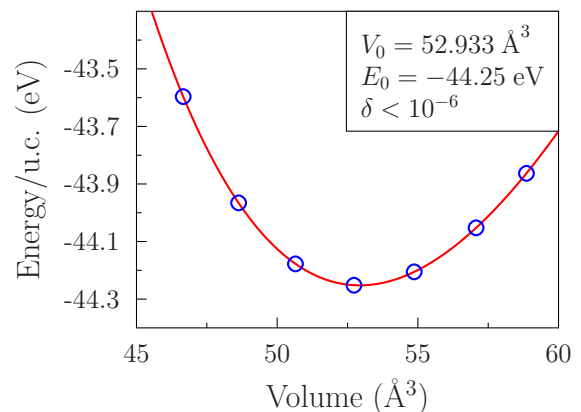


Figure 3.3: The total energy vs. volume for the bulk cubic LaAlO_3 within the local density approximation. Comparison of the calculated values (blue open circles) and the fitting curve (red line) is presented. The relative mean square deviation of the fit is $\delta < 10^{-6}$.

¹⁰Possible degeneracy of the ground state is taken into account by summing over the m index.

composition or nature of the interatomic bonding. In terms of the equilibrium volume V_0 and energy E_0 , the isothermal bulk modulus $B_0 = -V_0 \frac{\partial P}{\partial V}$ and its derivative with respect to pressure $B'_0 = \frac{\partial B_0}{\partial P}$, the Murnaghan equation of state and the corresponding total energy vs. volume dependence for a fixed number of particles and zero temperature can be written in the following form:

$$\begin{cases} P(V) = \frac{B_0}{B'_0} \left[\left(\frac{V_0}{V} \right)^{B'_0} - 1 \right] \\ E(V) = \frac{B_0 V}{B'_0 (B'_0 - 1)} \left[B'_0 \left(1 - \frac{V_0}{V} \right) + \left(\frac{V_0}{V} \right)^{B'_0} - 1 \right] + E_0 \end{cases} \quad (3.46)$$

The volume dependence of the total energy is nowadays accessible using different *ab initio* electronic structure methods. The four parameters V_0 , E_0 , B_0 and B'_0 in equation (3.46) are assumed to be independent of each other and are to be adjusted in order to fit the theoretical curve $E(V)$ to the calculated one $E_{\text{calc}}(V)$. Fig. 3.3 shows a comparison between the total energy values from first-principle calculations and a fit to the Murnaghan EqS for the bulk cubic LaAlO_3 ¹¹. The chosen range of lattice volumes has to be close to the equilibrium value to provide a reliable fit to the equation of state. In these conditions, the accuracy of the EqS is found to be high enough for the subsequent atomic relaxations and electronic structure calculations.

The structural optimization procedure sketched in this paragraph provides, in many cases, reliable results for oxide interfaces and bulk systems. Further on in the present work, this procedure will be applied to all studied compounds at the first step of investigation.

¹¹These calculations were performed in this work with an LDA exchange-correlation energy and serve only as an example of the application of the Murnaghan equation of state.

3.3 Green's function method

Although the plane-wave pseudopotential methods excels other *ab initio* approaches in terms of simplicity of the implementation, there is a number of inherent problems related to the description of strongly correlated electronic states. In this respect, different basis set and an appropriate formalism for the solution of the effective single-particle problem might be needed in order to overcome these problems. The Korringa-Kohn-Rostoker Green function (KKR-GF) method [113, 114] provides an alternative way to study the electronic structure of condensed matter. It has acquired large popularity in the last decades and is now a method of choice for accurate description of magnetic solids. The flexibility of the KKR method allows a systematic treatment of non-periodic systems, such as disordered alloys, impurities, finite atomic and molecular clusters, crystal surfaces, layered systems etc. that are not accessible by other electronic structure methods. Recent developments in the field also provided a framework for the estimation of finite-temperature effects (for details, see review [102]).

3.3.1 KKR equations for periodic solids

The main idea of the KKR-GF method is in many ways similar to that of the original DFT. In the KKR approach, the physical properties of the studied quantum system are expressed in terms of a single-particle Green function $G(\mathbf{r}, \mathbf{r}', \varepsilon)$, which contains, in principle, a comprehensive information about the electronic states and even provides some insights into the character of excitations. In contrast to DFT, where the central quantity – single-particle electron density – is derived by applying the variational principle to the total energy, the single-particle GF in the KKR method is derived from the Schrödinger equation. It is convenient and, at the same time, physically meaningful to search for the solution of this equation within the framework of multiple scattering theory (MST) [115]. In this theory, the whole system is described as an array of scatterers, each defined, in the simplest approximation, by a sphere of a certain radius (also called muffin-tin radius) surrounded by the interstitial regions. In a more general case, the Voronoi cell is ascribed to each scatterer. The problem of determining the Green function can be approached in a two-step procedure:

1. *Single-site problem* within a muffin-tin sphere (or Voronoi cell) embedded in vacuum is solved for a particular choice of the interacting potential $V^{(n)}(r)$ on site n . The effect of the site potential can be viewed as scattering of the incoming electronic wave into the outgoing one, which is fully characterized by the corresponding phase shift $\delta_l(E)$ (see the left panel in Fig. 3.4). By matching the solutions inside the muffin-tin sphere with the free-particle wavefunctions in the vacuum, one obtains the scattering matrix $t_l(E)$, which represents the scattering properties of the single-site potential $V^{(n)}(r)$.
2. *Multiple scattering problem* is addressed using the Dyson equation, which describes the effect of the disturbing potential $\Delta\hat{V}$ on the Green function:

$$\begin{aligned}\hat{G} &= \hat{G}^{(0)} + \hat{G}^{(0)}\Delta\hat{V}\hat{G} = \\ &= \hat{G}^{(0)} + \hat{G}^{(0)}(\Delta\hat{V} + \Delta\hat{V}\hat{G}^{(0)}\Delta\hat{V} + \dots)\hat{G}^{(0)},\end{aligned}\tag{3.47}$$

where $\hat{G}^{(0)}$ is the Green function of the free propagating particle, and the expression in the round brackets defines the t-matrix operator \hat{T} that satisfies the

relation:

$$\hat{T} = \Delta\hat{V} + \Delta\hat{V}\hat{G}^{(0)}\hat{T}. \quad (3.48)$$

Whereas the free-particle Green function $\hat{G}^{(0)}$ can be expressed analytically, the access to the full scattering operator \hat{T} is computationally more demanding. This problem can be solved in an elegant way in the framework of the MST. By considering the whole variety of the interaction processes as a composition of single-site scatterings and the free propagation in the interstitial regions (see the right panel in Fig. 3.4), one can decompose the \hat{T} -operator accordingly using the scattering path operator $\hat{\tau}^{nn'}(E)$:

$$\hat{T} = \sum_{nn'} \hat{\tau}^{nn'}(E). \quad (3.49)$$

The physical meaning of the scattering path operator $\hat{\tau}^{nn'}(E)$ can be understood, if one imagines the transfer of an electronic wave from site n' to site n , which includes all possible propagation paths and the corresponding scattering events in-between [116]. The $\hat{\tau}$ -operator is given, then, by matrix inversion of the so-called KKR-matrix $\hat{M} = \hat{t}^{-1} - \hat{G}^{(0)}$.

Once the single-particle Green function has been obtained, many properties of the studied system can be accessed straightforwardly. For example, the band structure is determined from the poles of the Green function $E_n(\mathbf{k})$. It is convenient to represent the electronic structure of periodic systems using the Bloch spectral function, which is derived by mapping the Green function onto the \mathbf{k} -space:

$$A_B(\mathbf{k}, E) = -\frac{1}{\pi N} \text{Im Tr} \sum_{nn'} \exp[i\mathbf{k}(\mathbf{R}_n - \mathbf{R}_{n'})] \int G(\mathbf{r} + \mathbf{R}_n, \mathbf{r} + \mathbf{R}_{n'}, E) d\mathbf{r}, \quad (3.50)$$

where the summation runs over all pairs of lattice vectors in real space.

For periodic solids without disorder, the $A_B(\mathbf{k}, E)$ function is a sum of Dirac delta-functions $\delta(E - E_n(\mathbf{k}))$ that depict the spectrum of the eigenvalues. The Bloch function becomes very useful in the presence of defects, which can be also treated by the KKR-GF approach and lead to smearing of peaks inherited from the ideal parent compound.

A number of other helpful quantities, such as density of states $n(E)$ and the real-space particle density $\rho(\mathbf{r})$, can be calculated using the Green function¹²:

$$\begin{cases} n(E) = -\frac{1}{\pi} \text{Im Tr} \int_{\text{u.c.}} G(\mathbf{r}, \mathbf{r}, E) d\mathbf{r} \\ \rho(\mathbf{r}) = -\frac{1}{\pi} \text{Im Tr} \int^{E_F} G(\mathbf{r}, \mathbf{r}, E) dE \end{cases} \quad (3.51)$$

Working with the Green function from the very beginning is not only a matter of a convenient representation of the electronic structure, but also includes further advantages related to the application of the Dyson equation (3.47). Using this equation one can describe the electronic properties of a perturbed system (e.g. a solid doped

¹²As the Green function is not restricted to the real energies, the integration in (3.51) can be effectively performed using a contour in the complex energy plane.

with impurities) using the Green function G_{ref} of the reference (unperturbed) system (e.g. a periodic crystal) and the perturbing potential ΔV :

$$G(\mathbf{r}, \mathbf{r}', E) = G_{\text{ref}}(\mathbf{r}, \mathbf{r}', E) + \int d^3r'' G_{\text{ref}}(\mathbf{r}, \mathbf{r}'', E) \Delta V(\mathbf{r}'') G(\mathbf{r}'', \mathbf{r}', E). \quad (3.52)$$

Since the choice of the reference system is not restricted by any conditions, the solution of the multiple scattering problem within the framework provided by the Dyson equation might become quite efficient with an appropriately chosen reference state. For instance, an auxiliary reference system with repulsive potentials provides a good starting Green function, which demonstrates a short-range character in real space and can be represented by a relatively sparse matrix. This facilitates the evaluation of the scattering path operator $\hat{\tau}^{nn'}(E)$ and the KKR matrix \hat{M} .

One of the simplest applications of the Dyson equation refers to the substitutional embedding of an impurity in a perfect host system [115]. In this defect system, the translational symmetry is obviously broken and the concept of the band structure is no longer valid. In standard plane-wave-based methods, this problem is circumvented by investigating supercells with sufficiently large dimensions, so that the spurious interaction between the impurity and its periodic images can be neglected. For most real systems, this approach becomes very demanding on the computational resources and, furthermore, relies on the erroneous assumption that the impurities form an ordered structure.

In contrast to this, the KKR-GF method is not restricted to periodic systems and allows for a consistent description of disordered solids with defects of different kind. A common procedure here, in case of a single embedded impurity, is to calculate first the Green function and the scattering path operator for the host system. Then, a region in the host Ω_{pert} is chosen that is assumed to be affected by the impurity. At the next step, the t-matrices of the host atoms in Ω_{pert} are replaced by that of the impurity and distorted host. This means that for the potentials of the host atoms in the Ω_{pert} -region charge relaxation is allowed. Finally, the multiple scattering problem is solved for the embedded cluster within the perturbed volume and the corresponding Green function is evaluated straightforwardly. To improve the quality of the described model, one has to guarantee among all the convergence with respect to the cluster dimensions.

3.3.2 Exchange coupling parameters

The nature of the magnetic ordering in solids, especially in transition metal oxides, is closely related to the character of exchange interactions between magnetic atoms. In case of magnetic insulators, these interactions can be described by an effective Heisenberg Hamiltonian within the approximation of localized spins:

$$H = \sum_{ij} J_{ij} \mathbf{s}_i \mathbf{s}_j, \quad (3.53)$$

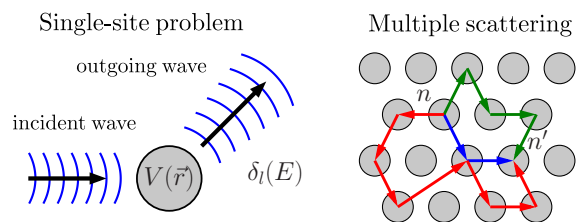


Figure 3.4: Schematic representation of the KKR Green function method for the effective one-electron problem in periodic solids. The solution of the single-site problem is applied to the multiple scattering picture to determine the scattering path operator between two sites n and n' .

where J_{ij} stands for the magnetic interaction between the spins \mathbf{s}_i and \mathbf{s}_j on sites i and j . The Heisenberg model is widely applied in combination with first-principle calculations due to the simplicity and physically transparent meaning of the model Hamiltonian (3.53). However, this kind of description fails or gives inconsistent results for itinerant magnets, such as ferromagnetic metals and double exchange perovskites [117]. This calls for a generalized approach to the estimation of the exchange coupling parameters.

The exchange energy for two sites i and j can be determined from the variation of the total energy caused by a small deviation in the relative spin orientation. Let us assume that the spins in the system form an ordered magnetic structure in z direction. If the two spins \mathbf{s}_i and \mathbf{s}_j become inclined by infinitesimal angle θ relative to the chosen quantization axis, then the magnetic energy changes by δE_{ij} . The latter includes both the intersite exchange $\delta E'_{ij}$ and the interaction δE_i of each spin with the environment (the rest of the system):

$$\delta E_{ij} = \delta E'_{ij} + (\delta E_i + \delta E_j). \quad (3.54)$$

For the intersite exchange, the phenomenological Heisenberg model is still valid in the first order terms, which gives the expression:

$$\delta E'_{ij} = J_{ij}(1 - \cos \theta). \quad (3.55)$$

By calculating the total energy variations for such low-energy spin excitations one can compute the exchange parameter J_{ij} for the two considered sites. This can be done using Andersen's "local force theorem" [118]:

$$\delta E = - \int_{occ.} d\varepsilon \delta N(\varepsilon), \quad (3.56)$$

where the integration is carried over the occupied single-particle density of states and $N(\varepsilon)$ is the number of states with the energy lower than ε . The variation $\delta N(\varepsilon)$ is easily accessible within the multiple scattering approach from the single-site t-matrix and the scattering path operator \hat{T} :

$$J_{ij} = \frac{1}{4\pi} \int_{occ.} d\varepsilon \text{Im Tr}_L \left\{ \Delta_i \hat{T}_{\uparrow}^{(ij)} \Delta_j \hat{T}_{\downarrow}^{(ji)} \right\}, \quad \Delta_i = \hat{t}_{i\uparrow}^{-1} - \hat{t}_{i\downarrow}^{-1}, \quad (3.57)$$

which is the famous *Lichtenstein formula* [117]. It describes the exchange interaction between two arbitrary sites independent of the concrete magnetic configuration.

3.3.3 Coherent potential approximation

One of the huge advantages of the KKR-GF method over other techniques is its ability to deal with disordered systems, where the supercell-based DFT approaches cannot be applied efficiently. The KKR method can be appropriately formulated for substitutional alloys and magnetically disordered lattices with a random distribution of components over the volume. I sketch here the main ideas standing behind this extension of the method on the example of binary alloys $A_c B_{1-c}$ ¹³.

In a random binary alloy, one has to deal with a chemical disorder, which means that each site of an ideal lattice is occupied with an atom either of sort A or sort

¹³The generalization for an arbitrary number of components is straightforward.

B with probabilities proportional to the concentrations of the individual components ($c_A = c$ and $c_B = 1 - c$, respectively). In spite of the periodicity of the underlying host lattice, the whole system with randomly distributed A and B atoms obviously does not possess any translational invariance. This renders all attempts to describe such systems with conventional electronic structure methods absolutely meaningless, since the very concept of the band structure does not apply to disordered solids. There is, however, a couple of possible subterfuges, such as the supercell approach [119] and the virtual crystal approximation (VCA) [120], the former being frequently applied by many researchers. Clear disadvantage of the supercell approach in case of random alloys is the necessity to go over all possible atomic configurations and the subsequent averaging to come up with an estimate for the studied properties, not to mention larger dimensions of the supercell in comparison to the primitive unit cell of the host lattice. Opposed to it, the VCA-based approach does not require enlarged crystal cells, however, the component specific information is lost in the final result. Because of the absence of the translational invariance, the configurational average of the electron wavefunction is not particularly sensible. On the other hand, this averaging procedure makes perfect sense for the single-particle Green function that represents the solution of the multiple scattering problem.

Historically, the first suggested approximation was based on the concentration-weighted average of the single-site scattering matrix of a binary alloy over the two components:

$$\hat{t}_{ATA} = c \cdot \hat{t}_A + (1 - c) \cdot \hat{t}_B. \quad (3.58)$$

This average t-matrix approximation, however, does not guarantee a positive density of states for real energies and, for that reason, was soon replaced by the coherent potential approximation (CPA) [121] that is nowadays widely used. The CPA method relies on the concept of the so-called CPA effective medium, which possesses the following property: the concentration-averaged properties of the CPA medium with one of the components embedded into it should reproduce the properties of this medium itself (3.5). In the KKR-GF formalism, this condition leads to a set of matrix equations for the scattering path operators that has to be solved self-consistently:

$$\begin{cases} \hat{\tau}_{CPA} = x \cdot \hat{\tau}_A + (1 - x) \cdot \hat{\tau}_B \\ \hat{\tau}_A = [\hat{t}_A^{-1} - \hat{t}_{CPA}^{-1} - \hat{\tau}_{CPA}^{-1}]^{-1} \\ \hat{\tau}_B = [\hat{t}_B^{-1} - \hat{t}_{CPA}^{-1} - \hat{\tau}_{CPA}^{-1}]^{-1}, \end{cases} \quad (3.59)$$

where the operator $\hat{\tau}_{CPA}$ implicitly determines the scattering matrix \hat{t}_{CPA} of the effective medium. The solution of these coupled equations is usually done iteratively starting from a good guess for the effective medium, which could be, for example, $\hat{\tau}_{CPA} = \hat{\tau}_{ATA}$. Finally, the Green function of the alloy is expressed in a natural way in terms of the concentration-weighted average over the individual components:

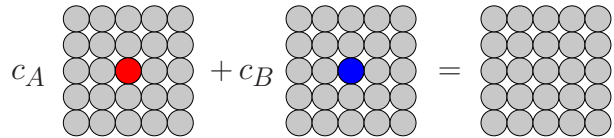


Figure 3.5: Schematic representation of the CPA approach for describing disordered solids within the KKR-GF formalism. The grey-colored atoms represent the effective CPA medium and the red/blue atoms stand for individual atomic species.

$$G(\mathbf{r}, \mathbf{r}', E) = \sum_{i \in \{A, B\}} c_i G_i(\mathbf{r}, \mathbf{r}', E). \quad (3.60)$$

The CPA method provides the most accurate description of disorder within the single-site approximation and has also the advantage that the component specific information is contained in the resulting Green function. This allows direct comparison with the results of nuclear magnetic resonance (NMR), Mößbauer, and X-ray absorption spectroscopy [102]. Although the original version of CPA applies to crystal structures with one atom per unit cell, the method has been already generalized onto a much larger variety of systems, such as complex perovskite alloys, disordered alloy layers on top of a substrate, interfaces with interdiffusion and cation intermixing etc. (for review, see [102]). Moreover, due to the general form of the CPA equations (3.59), this scheme can be also applied to thermal fluctuations of magnetic moments, which forms the basis for the disordered local moment theory (DLM) [122, 123].

CHAPTER 4

Electronic transport

General features of the electronic transport in quantum systems are discussed in this chapter.

First, a classification of different types of transport is introduced according to the dominant mechanism of carriers transfer. Then, the theoretical foundations of the ballistic transport in nanosystems are described on the example of the Landauer-Büttiker theory [124, 125]. Finally, the consequences of this theory and several noteworthy effects are examined in details in the last section. Several exemplary studies of electronic transport in oxide nanostructures are reviewed and the perspectives of these nanostructures for spintronics applications are analyzed.

4.1 Transport regimes

Electronic transport as the process of charge transfer in a certain direction under the application of an external electric field can happen on different time and length scales.

The important length scales are:

- l_e – the elastic mean free path,
- l_i – the inelastic mean free path,
- l_φ – the phase-coherence length.

The two parameters l_e and l_i determine the average distance between two scattering events (either energy-conserving or with energy loss) and the phase-coherence length l_φ characterizes the evolution of the phase of the electronic wavefunction in the course of propagation. Depending on the relation between these quantities and the characteristic size of the system L , different transport mechanisms will dominate.

One distinguishes basically between the diffusive and the ballistic transport (see Fig. 4.1), both of which can also have either classical or quantum character. If the system is sufficiently large ($L \gg l_e, l_i$), then the diffusive regime is set on, where the electrons propagate randomly through the crystal and are subject to scattering on the lattice itself, possibly on defects and quasiparticles. As the dimensions of the system decrease, the number of scattering events becomes smaller and eventually the electrons can propagate almost without scattering – the ballistic transport dominates. Additionally, if the Fermi wavelength of electrons (λ_F) is comparable to the size of the

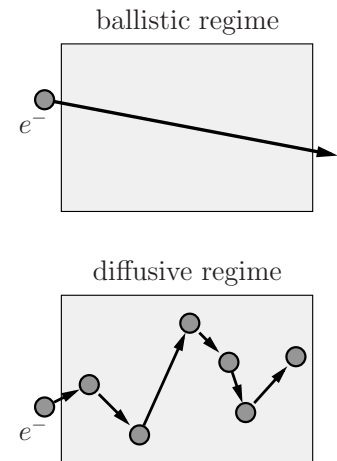


Figure 4.1: Schematic representation of the electronic transport in diffusive and ballistic regimes.

system, then the transport acquires quantum character. In this work, the transport properties of nanostructured junctions functioning in the ballistic quantum regime are of particular interest.

In the next section, I give a short review of the Landauer-Büttiker approach to the tunneling problem.

4.2 Ballistic tunneling transport



Figure 4.2: The two-terminal scheme for measuring the tunneling conductance of a barrier between two ideal leads in one-dimensional case.

The electronic transport can be measured using the two-terminal scheme¹ (see Fig. 4.2) where the conductor is connected via ideal leads to two reservoirs [126, 127]. The latter serve as source and drain for charge carriers, i.e. some reservoirs supply electrons that flow in the conductor and, after crossing it, enter the other lead, which is connected to

a drain. At the end, the electron will be adsorbed completely by the other reservoir. To put it in simple terms, I consider here the one-dimensional case at zero temperature. In these conditions, each of the two reservoirs can provide electrons with the energy up to the Fermi level μ_i ($i = 1, 2$), which is also the chemical potential of the corresponding lead. The total current in the left lead (1 in Fig. 4.2) has the following contributions:

1. carriers injected from reservoir 1:

$$I_0 = e \int_0^{\mu_1} n_{1D}(E)v(E) dE = \frac{2e}{h}\mu_1, \quad (4.1)$$

where due to the one-dimensionality of the problem the product of the density of states $n_{1D}(E)$ and the velocity of the electrons $v(E)$ remains constant;

2. electrons reflected from the conductor back into the considered lead:

$$I_R = -\frac{2e}{h}R_{11}\mu_1, \quad (4.2)$$

3. electrons transmitted from another lead through the conductor:

$$I_T = -\frac{2e}{h}T_{12}\mu_2. \quad (4.3)$$

The total current takes the form:

$$I_1 = \frac{2e}{h} [(1 - R_{11}\mu_1) - T_{12}\mu_2]. \quad (4.4)$$

¹In practice, the four-terminal scheme is applied where the current and voltage are measured using different pairs of electrodes.

The above expression can be simplified due to relations

$$T_{12} = T_{21} = T = 1 - R_{11} = 1 - R_{22} \quad (4.5)$$

to the following form:

$$I_1 = I = \frac{2e}{h} T(\mu_1 - \mu_2). \quad (4.6)$$

Dividing the current by the applied voltage $U = (\mu_1 - \mu_2)/e$, one arrives at the general expression for the conductance:

$$G = \frac{2e^2}{h} T. \quad (4.7)$$

In the Landauer-Büttiker theory, the ballistic electronic current is, therefore, expressed in terms of the single-particle tunneling probability.

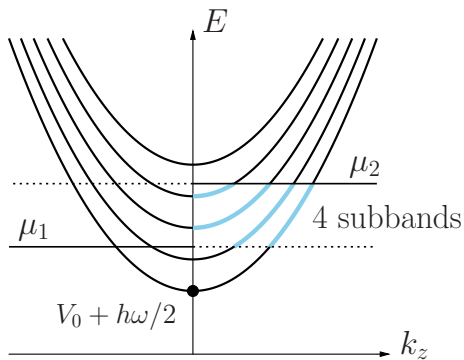


Figure 4.3: Schematic representation of the dispersion relation for different transverse subbands of a quasi-one-dimensional conductor. Position of the chemical potential in each lead ($\mu_{1,2}$) mark the relevant energy range $\mu_1 < E < \mu_2$, with 4 subbands in this example (marked with the lightblue color), that contribute to the tunneling current.

For the considered two-terminal scheme (Fig. 4.2), only those subbands that lie in-between the energy levels defined by the chemical potentials μ_1 and μ_2 contribute to the tunneling current. The $+k_z$ and $-k_z$ states moving in opposite directions are compensated for energies below μ_1 . The remaining uncompensated subbands are often called *transmission channels*. If N such channels are present in the ideal conductor, then the total conductance is given by

$$G = \frac{2e^2}{h} N. \quad (4.8)$$

In general case of a conductor with the transmission coefficients T_{ij}^σ characterizing the tunneling of states from the i th channel of the left lead into the j th channel of the right lead, the total conductance is expressed as the sum over all participating transport channels (for both spins σ) in the considered energy range:

$$G = \frac{e^2}{h} \left(\frac{1}{\mu_2 - \mu_1} \right) \int_{\mu_1}^{\mu_2} \left[\sum_{\sigma; i, j} T_{ij}^\sigma(E) \right] dE. \quad (4.9)$$

The total charge carried between the electrodes is restricted by the number N of the available transverse modes, each carrying the so-called quantum of conductance $G_0 = 2e^2/h$ (or, alternatively, e^2/h for each spin channel). For a ballistic conductor ($T =$

1) sandwiched between two contacts, the number of the transverse modes decreases, as the dimensions of the barrier go down, and the tunneling resistance changes in discrete steps approaching the value of approximately $12.9 \text{ k}\Omega$ [127]. The number of the contributing modes is determined approximately by the ratio between the Fermi wavelength λ_F and the dimensions of the barrier. In metals, one usually observes thousands of such modes due to the relatively small value of λ_F .

The Landauer-Büttiker approach can be successfully realized within the pseudopotential plane-wave method. A variation of this scheme, described in [128], proceeds as follows. First, the system is subdivided into the scattering region and two semi-infinite leads on both sides. Since the translational invariance is valid now only for two spatial directions perpendicular to the tunneling path, the electronic subbands can be described by the set of wavenumbers $\mathbf{k}_\perp = (k_x, k_y)$. In this formulation, the scattering problem can be solved separately for each \mathbf{k}_\perp point and each spin channel, which is advantageous for parallel calculations.

The scattering state Ψ is found as a linear combination of the solutions of the Kohn-Sham equations with a non-local pseudopotential inside the scattering region. The so-defined wavefunction has to be matched, for each energy, to the asymptotic form in both electrodes at the region boundaries:

$$\Psi = \begin{cases} \psi_j + \sum_i r_{ij} \psi_i, & \text{left lead} \\ \sum_i t_{ij} \psi_i, & \text{right lead} \end{cases} \quad (4.10)$$

where the transmission (t_{ij}) and reflection (r_{ij}) coefficients appear, and the indices i and j have here the same meaning as in (4.9).

The correct description of the tunneling transport constitutes the complex band structure of the system [129], which is formulated in terms of the generalized Bloch states. The latter represent, in case of an insulating barrier, the usual Bloch states in the xy plane, but decay in the z direction due to the energy gap in the band structure of the scattering region:

$$\psi_j(\mathbf{k}_\perp, z + d) = e^{(\kappa + ik_z)d} \psi_j(\mathbf{k}_\perp, z). \quad (4.11)$$

The generalized wavevector is now a complex number where the imaginary part κ characterizes the decay rate of the wavefunction in the insulator and k_z describes its oscillations in the direction of propagation. The analysis of the complex band structure of the leads and the barrier allows a qualitative understanding of the electronic transport.

After the matching conditions have been satisfied for specific conducting channels in both electrodes, the transmission matrix is constructed from the probability currents of the propagating Bloch states and the transmission coefficients t_{ij} . If the spin flip process is not allowed, then the transmission matrix is diagonal in spin indices. In this work, the plane-wave implementation [128] of the Landauer-Büttiker theory will be used to study the tunneling transport in oxide heterostructures.

4.3 Tunneling effects in oxides

Since the first success in growing oxide nanostructures with high precision on the atomic scale their application in spintronics and memory devices has been gradually

becoming more promising. The great majority of such devices contain tunnel junctions of different type. In the following, I shall discuss, first, the fundamentals of two effects that can be observed in tunnel junctions: the *tunneling electroresistance* (TER) and the *tunneling magnetoresistance* (TMR). Subsequently, the details of the tunneling electromagnetic resistance (TEMR) effect in multiferroic tunnel junctions that combine the two aforementioned phenomena will be discussed.

4.3.1 Tunneling electroresistance

In metal-ferroelectric-metal (M-FE-M) junctions with a sufficiently small thickness of the FE barrier the dominant transport mechanism is the direct quantum-mechanical tunneling of electrons from one electrode to another. The probability of this process depends largely on the effective potential profile that electrons experience in this junction. This potential is affected by the ferroelectric polarization that creates surface charges in the ferroelectric barrier, which are partially screened by the metallic electrodes on each interface [46, 130, 131]. For electrodes with different screening lengths, the electrostatic potential across the tunneling region is asymmetric for opposite directions of the spontaneous polarization. Therefore, the polarization reversal changes the effective height of the potential barrier and, consequently, the tunneling resistance. This is the mechanism of the tunneling electroresistance (TER) effect [132].

In a simple electrostatic model, where the screening in the electrodes is introduced by means of effective screening lengths δ_1 and δ_2 , the profile of the effective potential² in the junction along the propagation direction (Fig. 4.4) is described by the system of equations [132]:

$$\varphi(z) = \begin{cases} \frac{\sigma_S \delta_1}{\varepsilon_0} \exp\left(-\frac{|z|}{\delta_1}\right), & z \leq 0 \\ \frac{\sigma_S \delta_1}{\varepsilon_0} + U - \Delta\varphi \cdot \left(\frac{x}{d}\right), & 0 < z < d \\ -\frac{\sigma_S \delta_2}{\varepsilon_0} \exp\left(-\frac{z}{\delta_2}\right), & z \geq d, \end{cases} \quad (4.12)$$

where the effect of the insulating barrier with a thickness d is represented by an abrupt jump of the potential by $+U$ on both interfaces and the surface density of the screening charge σ_S is derived from the continuity condition for the electrostatic

²Additional factors might appear in real systems, where the details of the potential barrier created by the ferroelectric as well as the position of electronic bands and the Fermi level must be taken into account.

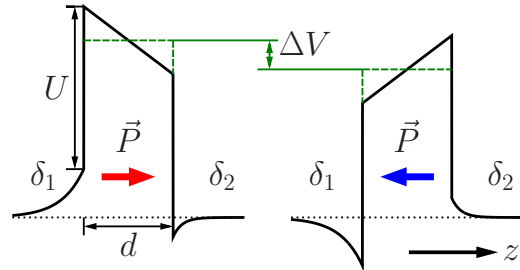


Figure 4.4: The effective potential profile in a metal-ferroelectric-metal junction for two opposite polarizations \vec{P} pointing either to the right or to the left. The screening lengths of the electrodes are δ_1 and δ_2 . The width and the height of the ferroelectric barrier are denoted by d and U , respectively.

potential $\varphi(z)$:³

$$\sigma_S = \frac{dP}{\varepsilon(\delta_1 + \delta_2) + d}. \quad (4.13)$$

The potential drop in the barrier $\Delta\varphi$ indicates the existence of the depolarizing field E_{dep} inside the ferroelectric, which is due to incomplete screening of the polarization charges by the electrodes. It is straightforward to derive the expression for this field starting from (4.12):

$$E_{\text{dep}} = \frac{1}{\varepsilon_0} \frac{P(\delta_1 + \delta_2)}{\varepsilon(\delta_1 + \delta_2) + d} = \frac{1}{\varepsilon_0} \frac{P}{\varepsilon + d/(\delta_1 + \delta_2)}. \quad (4.14)$$

For ideal electrodes ($\delta_i = 0$), the surface charges are fully screened and the depolarizing field vanishes. In this case, there is no critical thickness for the ferroelectricity and the spontaneous polarization is preserved from any size effects. In contrast to this, a real system with imperfectly screening electrodes shows the paraelectric transition below some critical thickness h_{cr} , the value of which can be derived from general considerations regarding the total electrostatic energy [25]. As it can be seen from expression (4.14), bulk behaviour is restored either for $\delta_i \rightarrow 0$ (ideal screening) or $d \rightarrow \infty$ (thick barrier).

The difference in the average height of the effective tunneling potential for two polarization directions, as follows from the construction (4.12), is given by

$$\Delta V = \frac{1}{\varepsilon_0} \frac{dP(\delta_1 - \delta_2)}{\varepsilon(\delta_1 + \delta_2) + d}. \quad (4.15)$$

The average potential appears to be higher for the polarization pointing to the electrode with a smaller screening length ($\delta_2 < \delta_1$ in Fig. 4.4). The tunneling resistance for this state (G_R) is accordingly larger than for another one (G_L), which explains the aforementioned TER effect. The strength of this effect is usually characterized by the TER ratio:

$$\text{TER} = \frac{G_L - G_R}{\min(G_L, G_R)} \times 100\%, \quad (4.16)$$

which is sometimes called the optimistic TER ratio, since in certain systems it can exceed 100% by orders of magnitude, whereas putting $\max(G_L, G_R)$ in the denominator restricts the TER ratio to the interval between 0 and 100%. Generally, the TER ratio increases with the thickness of the barrier due to different decay rates of G_L and G_R . However, larger thickness also means lower tunneling conductance. Another way to enhance the TER ratio, as seen from (4.15), is to use a ferroelectric material with higher spontaneous polarization. It should be kept in mind that the TER effect vanishes for perfect metallic electrodes ($\delta_i = 0$) or in case of the electrodes with the same screening length $\delta_1 = \delta_2$, which gives $\Delta V = 0$. In both cases, the potential profile described by the system of equations (4.12) is symmetric with respect to the switching of the ferroelectric side and, therefore, the TER ratio equals zero in this model. In order to let the tunneling resistance effect set on, one could take either dissimilar electrodes, like in Fe/BTO/LSMO junctions [133], or choose the two opposite interfaces to be chemically or structurally different, as is the case for SrRuO₃/BaTiO₃/SrRuO₃ junctions [134]. Numerous experimental studies, supported also by first principles calculations, have

³In these equations, ε_0 and ε represent the vacuum permittivity and the relative permittivity of the barrier, respectively.

reported high TER values in similar M-FE-M junctions with ferroelectric oxides like BaTiO_3 and the disordered perovskite alloy $\text{PbZr}_x\text{Ti}_{1-x}\text{O}_3$ as the tunneling barrier with a characteristic thickness of several nanometers.

The consistent description of tunneling in ferroelectric junctions remains a challenging problem for *ab initio* methods. In the simple phenomenological model discussed above the TER effect is ascribed solely to the change of the effective tunneling potential. However, a real junction would show much richer physics: under the application of a finite bias voltage lattice relaxations due to the piezoelectric response [135] and changes in the chemical potentials of the electrodes, as well as the band bending near the interfaces emerge [136, 137], which should be introduced into the model. This appears to be currently problematic within the DFT scheme due to some intrinsic limitations:

- The fundamental band gap of the insulating barrier is usually underestimated within the LDA and GGA approaches.
- The Fermi level is often located near the edge of the conduction band, which leads to incorrect values for the Schottky barrier and, therefore, an overestimated tunneling current.
- Metallization of the ferroelectric layers near the interface with a metal, which is often observed in oxide tunnel junctions, reduces the effective thickness of the tunneling region and thereby enhances the current exponentially.
- Most currently used implementations of DFT are restricted to the zero-bias limit and, for that reason, give no information on the voltage dependence of the tunneling conductance.

These and other factors should be taken care of in every particular case.

4.3.2 Tunneling magnetoresistance

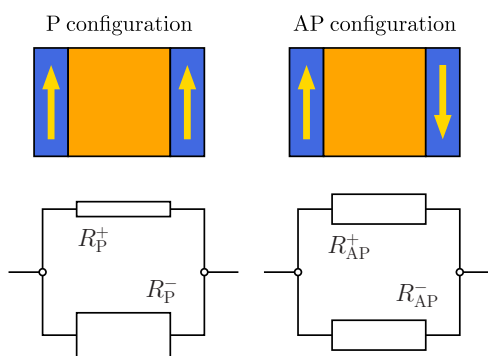


Figure 4.5: Schematic representation of the two-current model for the metal-insulator-metal tunnel junction with the parallel (P) and the antiparallel (AP) alignment of the magnetizations in the electrodes.

Similar to systems showing the TER effect, junctions consisting of an insulating barrier sandwiched between two ferromagnetic electrodes demonstrate interesting tunneling properties as well. In these systems, the tunneling conductance depends on the relative orientation of the magnetizations in the electrodes. If the electron scattering occurs only in the electrodes and there are no spin-flip processes in between, then the transport properties of such junctions can be described using the two-current model proposed by Mott [138, 139] and extended by Campbell and Fert [140, 141]. The spin-up and spin-down channels are decoupled from each other, if there are no spin flip processes, and, therefore, they contribute to the total effect like two resistances connected parallel to each other (Fig. 4.5).

For the parallel orientation of the magnetizations, the electrons in the spin-up channel move through the junctions almost without scattering, whereas the electrons in the

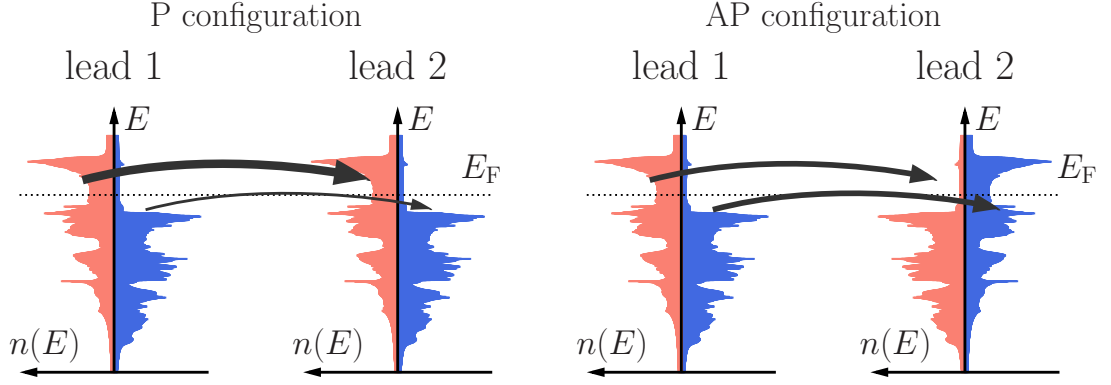


Figure 4.6: Jullière's model for the tunneling magnetoresistance phenomenon. Density of states (DOS) for the majority (blue) and the minority (red) spin channels in each electrode is represented for the parallel (P) and the antiparallel (AP) configurations. The intensity of current between the two leads (shown by the thickness of the arrow) is determined by the product of the corresponding densities of states at the Fermi level (marked by dashed lines).

spin-down channel are strongly scattered in both electrodes ($R_p^- > R_p^+$ in Fig. 4.5). The contributions of the two spin channels to the total tunneling resistance may differ by several orders of magnitude in systems with highly spin-polarized density of states at the Fermi level. For the antiparallel configuration, on the other hand, we see that considerable scattering takes place in both spin channels: spin-up electrons are mostly scattered in the right electrode and spin-down electrons – in the left one. Correspondingly, both spin channels contribute equally to the total resistance ($R_{AP}^+ = R_{AP}^-$). The two-current model predicts the *normal tunneling magnetoresistance* (TMR) effect, which constitutes the fact that the parallel configuration has a lower resistance than the antiparallel one.

In full analogy with tunneling electroresistance, the TMR ratio is defined by

$$\text{TMR} = \frac{G_P - G_{AP}}{G_{AP}} \times 100\%, \quad (4.17)$$

where G_{AP} is, in most cases, lower than G_P , so that the defined TMR ratio can become larger than 100%.

Some features of the tunneling magnetoresistance phenomenon can be interpreted in terms of the spin polarization of charge carriers. For each electrode, the spin polarization $P^{(s)}$ of the density of states at the Fermi level ($n = n(E_F)$) is derived as the asymmetry coefficient between the spin-up and spin-down channels:

$$P^{(s)} = \frac{n^+(E_F) - n^-(E_F)}{n^+(E_F) + n^-(E_F)} = \frac{n^+ - n^-}{n^+ + n^-}. \quad (4.18)$$

According to *Jullière's model* [142], the tunneling conductance for each spin channel is proportional to the product of the corresponding densities of states in the left (1) and the right (2) leads at $E = E_F$. From the schematics in Fig. 4.6 it is clear that:

$$\begin{aligned} G_P &\sim n_1^+ n_2^+ + n_1^- n_2^-, \\ G_{AP} &\sim n_1^+ n_2^- + n_1^- n_2^+. \end{aligned} \quad (4.19)$$

Substituting it into (4.17) and using the definition of the spin polarization one

arrives at the Jullière expression for the relative conductance variation:

$$\text{TMR} = \frac{\Delta G}{G_{\text{AP}}} = \frac{2 P_1^{(s)} P_2^{(s)}}{1 - P_1^{(s)} P_2^{(s)}}, \quad (4.20)$$

where $P_{1,2}^{(s)}$ are the spin polarizations of the two electrodes.

The TMR ratio can be effectively increased by using half-metallic electrodes where $n(E_F) = 0$ in one spin-channel. A good candidate for this is the widely discussed doped manganite series with the $\text{La}_{1-x}\text{Sr}_x\text{MnO}_3$ compound being the most studied [35]. High spin polarization of this material (up to 95%) has been measured up to room temperature, and the LSMO/STO/LSMO tunnel junctions show extremely high TMR ratios reaching 1800% at 4 K [143]. Another reason for the wide use of LSMO electrodes is the high Curie temperature of over 270 K. The FM structure of doped manganites above the critical Sr-concentration persists up to the temperature, which increases as a function of doping level x and reaches its maximum $T_c = 370$ K at $x = 0.30 - 0.35$ (see Fig. 2.7 in chapter 2).

Julliere's model obviously neglects the electronic structure of the insulating barrier and its interfaces with the electrodes and, therefore, will be referred to in this work only for interpreting the transport properties of the studied oxide junctions (see chapter 5.2 with the results for the Co/PZT interface). The aforementioned effects appear to be extremely important for the tunneling processes in oxide systems, as confirmed by both experimental and theoretical findings on the extensively studied example of epitaxially grown Fe/MgO/Fe junctions [144–148]. To capture the subtle features of the electronic transport in oxide-based junctions, the Landauer-Büttiker approach to the tunneling problem is chosen in this work.⁴

4.3.3 Multiferroic tunnel junctions

In view of the rich physics at multiferroic oxide interfaces, which was briefly touched in chapter 2, the idea of enhancing the qualities of modern tunneling devices by incorporating such oxide structures appears to be natural. The concept of multiferroic tunnel junctions (MFTJs) as an object of spintronics has been attracting researchers during the last years. These quantum systems combine the outstanding properties of both TER- and TMR-active systems and offer additional degrees of freedom related to possible couplings between the ferroelectric barrier and the magnetic electrodes.

First, let us consider the new functionality that the MFTJs provide. In multiferroic junctions with two different electrodes (or chemically different interfaces), the electrostatic potential profile along the transport direction is asymmetric for the two opposite polarizations, which leads to the onset of the

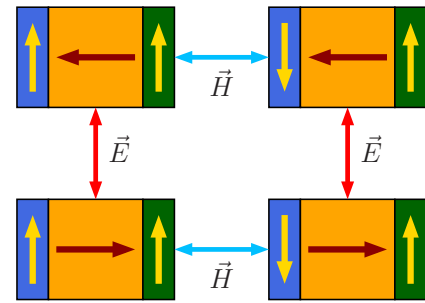


Figure 4.7: Four-resistance state of a multiferroic tunnel junction and possibilities of switching between them (double arrows connecting different junctions). The lead magnetizations are shown by vertical arrows and the spontaneous polarization – by horizontal ones.

⁴Refer to chapter 5.4 for the results concerning the Co/PTO(PZT)/Co and LSMO/PTO/Co multiferroic junctions.

tunneling electroresistance (see paragraph 4.3.1 above). On the other hand, the spin-dependent transport is controlled by the spin polarization of charge carriers and the orientation of the magnetizations in the electrodes. Coexistence of these two effects – TER and TMR – in multiferroic tunnel junctions leads to the realization of a four-state junction (Fig. 4.7). Switching between these states can be achieved by both electric and magnetic fields. The TER ratio depends now on the conjugate order parameter (magnetic field), whereas the TMR ratio depends on the external electric field and the spontaneous polarization of the barrier [149]. This behaviour was predicted by first-principle calculations for such all-oxide MFTJs as $\text{SrRuO}_3/\text{BaTiO}_3/\text{SrRuO}_3$ [134] and has been experimentally confirmed, for example, for $\text{Co}/\text{PZT}/\text{LSMO}$ junctions [11] where LSMO stands for the $\text{La}_{1-x}\text{Sr}_x\text{MnO}_3$ double-exchange perovskite.

The role of a strong magnetoelectric coupling at the interfaces of such junctions is discussed in the literature by different groups [10, 62]. As suggested by Tsymbal et al. [150], the existence of a strong interfacial ME coupling can significantly enhance the strength of the TER effect in certain MFTJ. Based on first-principle calculations, the authors predict the realization of the giant resistive switching effect in $\text{LSMO}/\text{BaTiO}_3/\text{LSMO}$ tunnel junctions. It was explained in paragraph 2.2.2 that the electrostatic doping due to the proximity of the ferroelectric surface initiates a magnetic phase transition in the manganite, which causes a sizeable change in the magnetization. In the aforementioned tunnel junction, the magnetically reconstructed layers of LSMO act as an atomic-scale spin valve that dramatically suppresses the tunneling of electrons through the junction for one polarization, thereby significantly enhancing the strength of the TER effect. This and other examples discussed above convince that the ME coupling effect can improve the functionality of multiferroic tunneling devices.

CHAPTER 5

Selected results

In this chapter, selected results of my PhD work are discussed in detail. The general question which is underlying all presented *ab initio* studies concerns the influence of the local structure and the interplay between different ferroic order parameters on the electronic properties and, especially, coherent transport in multiferroic oxide nanostructures.

First, the phenomenon of a field-induced two-dimensional electron gas (2DEG) is discussed on the example of the interface between the antiferromagnetic oxide SrTcO₃ and the ferroelectric BTO surface in relation to a similar effect in the prototype LaAlO₃/SrTiO₃ (001) nanostructure. Additional information regarding the origin of magnetism and the mechanism of exchange interactions in Tc-based 4d perovskites ATcO₃ can be found in [151]. The rest of this work is motivated by the recent observation of a robust four-resistance state in the LSMO/PZT/Co multiferroic tunnel junctions where the sign of the tunneling magnetoresistance can be reversibly switched by an external electric field [11]. Multiferroic properties of the two chemically different interfaces in these junctions (LSMO/PTO and Co/PZT [51]) are studied in the present work using first-principle DFT-based methods. The mechanism of the strong interfacial magnetoelectric (ME) coupling and the local structural features are analyzed, and the possibilities of tuning the ME coupling are proposed. The chapter closes with a discussion of the spin-dependent coherent transport in the Co/PTO(PZT)/Co and LSMO/PTO/Co tunnel junctions, for which four-resistance states were obtained.

For the investigation of electronic effects at multiferroic oxide interfaces, different *ab initio* techniques were applied to produce reliable results. Electronic structure calculations for all studied interfaces were performed using the plane-wave pseudopotential method of the Vienna *Ab initio* Simulation Package (VASP) [152–154]. Electron transmission in the tunnel junction was calculated within the Landauer-Büttiker formalism available in QUANTUM ESPRESSO [155]. Electronic and magnetic properties of bulk ATcO₃ perovskites [151] were investigated using the KKR Green function method of the HUTSEPOT code [156].

5.1 2DEG at the SrTcO₃/BaTiO₃ (001) interface

As it was stressed already in chapter 2, the interfaces between insulating oxides can behave exotically. One of the prominent examples is the observation of a two-dimensional electron gas (2DEG) in the LaAlO₃/SrTiO₃ system (LAO/STO) for the LaO/TiO₂-terminated interface [12, 67, 73, 157]. Until now, the nature of 2DEG in LAO/STO has not been completely understood, although many scenarios were suggested in the literature (see, for example, [68, 71, 158]). When the paraelectric SrTiO₃ component of the 2DEG composite system is replaced by a robust ferroelectric (FE), such as BaTiO₃ (BTO), this may create an extra functionality due to its switchable polarization, as confirmed recently in experiments [159]. In general, the interplay of the electronic and structural properties seen at the interface between ferroelectrics and metals (or gapless oxides) has been well understood during the last decade [160, 161]. For the FE/ferromagnet multiferroics, strong magnetoelectric coupling can be realized at the microscopic level near the interface [60]. However, *ab initio* studies of composite multiferroics where the role of a magnetically ordered oxide on the phenomenon of 2DEG is investigated remain sparse [162], and further work is needed in this direction.

In the present work, recently synthesized antiferromagnetically ordered SrTcO₃ perovskite [33, 34] is combined with the robustly ferroelectric BTO to form a multiferroic interface. The reasonably good lattice match better than 1% makes it possible to grow this AFM/FE oxide interface epitaxially. The expected window of the multiferroic functionality is large in comparison to most single-phase multiferroics, since BTO is strongly ferroelectric up to 390 K and SrTcO₃ remains AFM ordered until 1000 K [33, 34].

According to the available experimental data [33, 34], SrTcO₃ is antiferromagnetic, with surprisingly high Néel temperature T_N of about 1000 K and the Tc magnetic moment of $1.87 \mu_B$ measured at room temperature. The compound possesses an orthorhombically distorted perovskite structure, with $Pnma$ symmetry where the Tc nearest neighbors are ordered antiferromagnetically, forming thereby the G -type AFM configuration similar to that seen in SrMnO₃ [13]. It was suggested [33] that the anomalously high T_N of SrTcO₃ is due to the particularly strong covalency of Tc–O bonds demonstrated by first-principle calculations [33, 151, 163]. Until now, the experimental value of the band gap of SrTcO₃ is not available. However, the *ab initio* calculations of SrTcO₃ that use moderate values for the Hubbard parameter yield simultaneously the optimal set of all magnetic properties including T_N and suggest that the band gap is rather small $\Delta E_g < 0.5$ eV [151]. From this point of view, SrTcO₃ might be considered as an antiferromagnetic semiconductor rather than an insulator when the transport properties are studied.

Below, the *ab initio* results for the structural, magnetic and electronic properties of BTO/SrTcO₃ (001) are presented focusing on how the proximity of the two ferroic phases changes the electronic states near the Fermi energy. In the beginning, the structural model applied for this interface is described. The specific features of the relaxed atomic structure near the interface and its influence on intrinsic antiferromagnetism of SrTcO₃ are analyzed. Here, I discuss the geometry of the oxygen octahedra and the cation-oxygen bonds in connection with chemical environment of the interface. Afterwards, the focus will be shifted onto the electronic states that are localized on the interfacial cations and appear near the Fermi level due to the charge transfer. The effect of strong electronic correlations is studied within the Hubbard parametrization.

The 2DEG effect is illustrated by the local density of states and band structure. Finally, a summary of the *ab initio* study is given and some important implications are mentioned.



Figure 5.1: The side view of the supercell with vacuum (a) and without vacuum, i.e. superlattice (b), both of which were used to model the $\text{BaTiO}_3/\text{SrTiO}_3$ (001) interface. The two different terminations, SrO/TiO_2 and TcO_2/BaO , are marked as TiS and BT, respectively. The numeration of atomic layers outward the interface, as shown in the panel (a), is used throughout all further figures and text. The electric polarization of BaTiO_3 is oriented along the [001] direction (shown by the horizontal arrow).

The parameter values are ranging between $U = 0$ and 3 eV, including $U = 0.5$ eV, which was optimized previously for bulk SrTiO_3 [151].

The analysis of *ab initio* calculations published so far on LAO/STO [12, 67, 68, 71, 73, 157, 158, 165], shows that the structural model has been transformed from the initially used superlattice to the slab geometry with a vacuum layer, which separates the two insulating materials. It seems that the latter approach is more accurate and reliable, since it allows to simulate the correct electrostatic boundary conditions for the studied interface and confirms the thickness-dependent transition from the insulating to 2DEG behavior. Extra parametrization, namely, LDA+U is used then to model the mixed-valency Ti state at the interface [69]. Regarding composite ferroelectrics, it is experimentally established that BTO films grow in complete unit cells on an atomically clean substrate [47]. For that reason, the interface between BaTiO_3 and SrTiO_3 can be dually terminated, namely, either SrO/TiO_2 (TiS) or TcO_2/BaO (BT). In our work, these two terminations were simulated separately within the supercell with vacuum (SwV), whereas the use of the superlattice (SL) mimics the terminations TiS and BT simultaneously as shown in Fig. 5.1b. For the SL model, its supercell combines 5-u.c. thick BTO and 7-u.c. thick SrTiO_3 stacked along the [001] direction, as shown in Fig. 5.1. In the case of SwV, the vacuum of 17 Å prevents spurious interactions between the periodic images. In all calculations, each planar (x, y)-layer contains two formula units to adopt the AFM ordering and tilting patterns of oxygen octahedra seen in SrTiO_3 . The 8-u.c. SrTiO_3 was found to be thick enough to separate the interface from the free surface, using the SwV model, and the two interfaces from each other for the SL model. The in-plane lattice parameter was fixed to the experimental value of bulk BaTiO_3 ($a_0=3.991$ Å) to simulate the epitaxial growth of SrTiO_3 on the ferroelectric substrate. According to the recent experimental data [33], the lattice

The calculations were performed using the Vienna *Ab initio* Simulation Package (VASP) [152–154] within the generalized-gradient approximation (GGA) to the exchange-correlation potential [94]. The electron-ion interactions were described by projector-augmented wave pseudopotentials [108], and the electronic wave functions were represented by plane waves with an energy cutoff of 460 eV. For ionic relaxation, the Γ -centered $4 \times 4 \times 2$ k -point Monkhorst-Pack [164] mesh was used. After relaxation the calculated forces are always less than 10^{-2} eV/Å. The use of a denser k -mesh yields essentially the same atomic positions. For the density of states (DOS), the tetrahedron method and the $8 \times 8 \times 2$ k mesh were utilized with no smearing. To take into account the effect of strong electronic correlations, the GGA+ U parametrization [96] was applied on the $4d$ orbitals of technetium. The U parameter

parameter of SrTcO_3 is 3.976 Å, which, in view of the larger lattice constant of BTO, may lead to a moderate tetragonal contraction along [001] of about 0.5%. Our GGA-PBE calculations give a similar result: the estimated equilibrium lattice constants equal approximately 4.04 Å and 3.98 Å for BTO and SrTcO_3 , respectively, meaning, similarly to experiment, that a tetragonal deformation of the magnetic oxide is anticipated in this structure.

In our SwV calculations, the two most distant BTO unit cells from the interface were fixed during relaxation to keep the certain polarization state, while all other ions were allowed to relax. In the superlattice, the three central unit cells of each oxide were fixed and all other atoms were relaxed, but when all BTO ions were allowed to relax their coordinates were almost the same. It should be noted that, BTO films thinner than 5 unit cells are ferroelectrically unstable and the depolarization effect takes place, in accordance with recent findings [60, 160, 166]. Here, I do not focus on the BTO free surface and depolarization field effect. Although the intralayer cation-oxygen displacements may be detected in ultrathin BTO films with less than 4 unit cells [48], such films are not ferroelectric. Some authors suggest a critical thickness of a robust FE film might be about 10 nm [167–170]. The discussion goes beyond the scope of this study. Instead, the polarization reversal in BTO is modelled using relatively thin slabs and the scheme described in [50]. Thus, one can construct the two dually polar supercells corresponding to P_\downarrow and P_\uparrow , in which the BTO part contains at least 5 unit cells where the ionic displacements in each atomic layer before relaxation were equal to the corresponding values in the bulk material. For the polarization state P_\downarrow , oxygen atoms are placed above the cations in each layer, and *vice versa*, the state P_\uparrow means that all intralayer displacements $\Delta z = z_{\text{cation}} - z_{\text{O}} > 0$. Additionally, the paraelectric state of BTO ($P = 0$) was calculated, starting from zero intralayer ionic displacements $\Delta z = 0$. After relaxation, the structural changes near the two chemically different interfaces, referred below as TiS and BT, are analyzed. Most importantly in this context, to know whether the existence of electric polarization and/or its direction affect the electronic states at the interfaces. For each polarization, the energies of all possible magnetic configurations of SrTcO_3 , namely, the G-, C- and A-type AFM ordering [34] were collected for comparison. Below, I present mainly the results obtained within the SwV model, while the less reliable SL model is used to reveal the similarities and differences between these two options.

Table I. Relaxed Ti–O and Tc–O separations at the TiS and BT interfaces for the three polarization states, simulated within the SwV model.

	termination	P_\downarrow	$P = 0$	P_\uparrow
Ti-O (Å)	TiS	2.04	1.95	1.90
	BT	2.16	2.01	1.93
Tc-O (Å)	TiS	1.96	2.01	2.02
	BT	2.00	2.07	2.10

Chemical bonding at the TiS and BT interfaces is mediated by oxygen atoms placed in the layers TiS and (BT-1) atop Ti and Tc, respectively, as shown in Fig. 5.1. Both the SL and SwV models suggest that the interfacial Ti–O and Tc–O separations are rather sensitive to the \mathbf{P} -reversal of BTO since the change of the corresponding bond lengths is about 9% (see Table I). Such large variations affect the strength of the orbital hybridization and exchange

interactions at the interface. Paraelectric BTO results in the interfacial bond lengths whose values are varied between those of the two polar states, P_\uparrow and P_\downarrow . The BT termination shows the most significant changes upon the \mathbf{P} -reversal, as compared to the TiS termination.

To demonstrate the structural changes occurring in BTO below the interface one can use the intralayer cation–oxygen displacements along [001], which visualize the depolarization effect. These Δz 's were calculated as the average z -coordinate separation between the Ti/Ba cations and oxygen atoms. In bulk BTO for its optimized tetragonal elongation $c/a = 1.013$, $\Delta_{\text{Ti-O}} = 0.13 \text{ \AA}$ and $\Delta_{\text{Ba-O}} = 0.10 \text{ \AA}$. At the interfaces, for P_{\uparrow} the relaxed Δz are reduced, especially, in the TiS case, but for the opposite polarization their Δz are almost the same as in the bulk (Fig. 5.2). The SL model shows similar trends. Moreover, when the initial BTO displacements are forced to be zero ($P = 0$), the relaxation results in notably distinct and negative Δz within the first two u.c. near the interface. Such behavior might be related to intrinsic features of the 2DEG system. For instance, the paraelectric STO side of $\text{LaAlO}_3/\text{SrTiO}_3$ behaves similarly. For $P = 0$ in $\text{BTO}/\text{SrTcO}_3$, the relaxed interfacial O ions which belong formally to cubic BTO are pulled away by Tc that introduces further displacements near the interface. When the BTO side is polar, this environmental mechanism enhances the displacements that correspond to the P_{\downarrow} polarization and suppresses those that appear for the P_{\uparrow} polarization pattern.

Regarding the tilting pattern of SrTcO_3 , all relaxed O octahedra seen near the interfaces and free surface, tend to be less rotated compared to the bulk material. It should be noted here that each TcO_2 layer of the supercell contains two Tc and, accordingly, there are two pairs of altered Tc-O-Tc angles, Θ . In bulk SrTcO_3 , all Θ values are the same: $\Theta = 167.4^\circ$. However, near the interface and surface

the altered-angle values of each pair become slightly different and, for that reason, the average $\langle \Theta \rangle$ is used in Fig. 5.3 to characterize the tilting degree. For the surface $\text{SrTcO}_3(001)$, the illustration and details are given in [151]. In general, among the four Θ s there are two types that differ from each other, and this is due to BTO which breaks the Pnma symmetry of SrTcO_3 , so that the alternating tilting angles are deformed differently near the interface. For the TiS termination, (i) the tilting variation is not sensitive to the polarization reversal, and (ii) the interfacial $\langle \Theta \rangle$ is increased by almost 9° over the bulk value and, then, outward the interface $\langle \Theta \rangle$ quickly approaches its bulk value. For another interface (BT), the interfacial tilting is significantly suppressed ($\Theta \rightarrow 180^\circ$) while the polarization reversal of BTO yields a minor effect. Such tilting variations were reproduced using the superlattice and, hence, both structural models suggest that the tilting flattens within a couple of unit cells near the interface. The bond flattening near the $\text{SrTcO}_3(001)$ surface was discussed in [151] as well. The Tc layers, which are distant from both the interface and surface, are characterized by the uniform distribution of their tilting angles whose values are close to that of bulk SrTcO_3 [33].

As noted before, the structural changes may affect the exchange interactions and magnetic ordering near the SrTcO_3 interface. The relation between structure and magnetism has been recently discussed for the $4d \text{ ATcO}_3$ family [163, 171]. Our results also show that the magnetic moments of the AFM-ordered Tc cations can be tuned near the interface by the BTO polarization reversal, although the overall magnetic

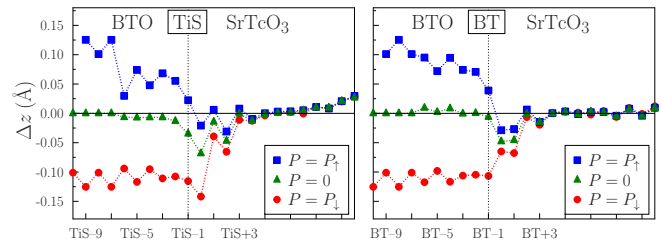


Figure 5.2: The relaxed layer-resolved ionic displacements Δz are shown for each monolayer of BTO and SrTcO_3 for the three P states: P_{\downarrow} , $P = 0$ and P_{\uparrow} . The topmost BTO layer near the TiS (BT) interface is shown by a dashed line and labeled as TiS-1 (BT-1).

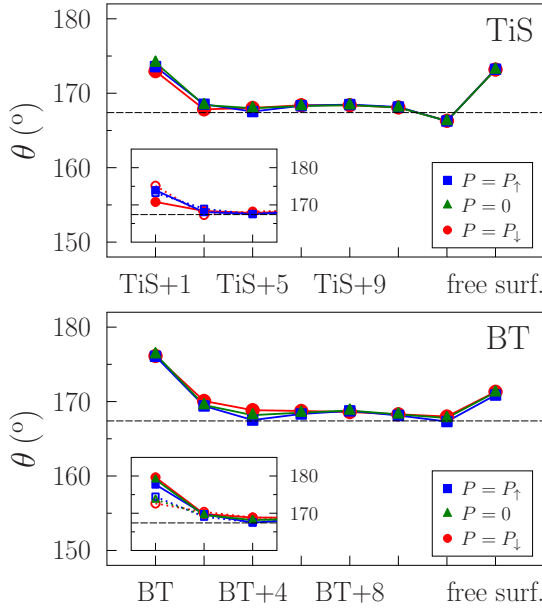


Figure 5.3: The Tc–O–Tc tilting angles, $\langle \Theta \rangle$, calculated for each of the three P states and plotted vs the layer position outward the interface. The angle in bulk SrTiO₃, $\Theta = 167.4^{\circ}$, is indicated by the horizontal dashed line. The insets show the two differently altered Θ 's, seen near the interfaces and plotted by solid and dashed lines.

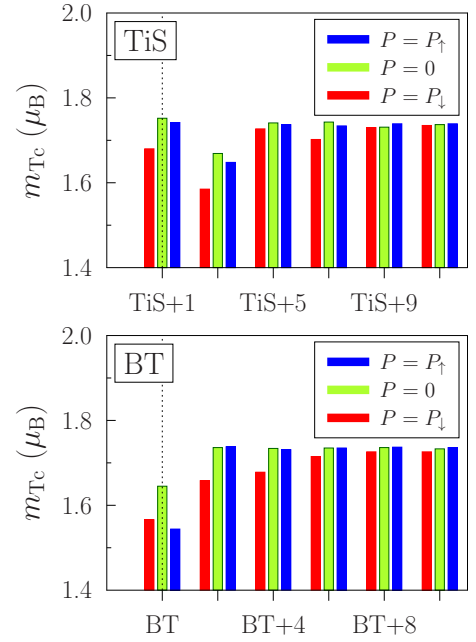


Figure 5.4: The layer-resolved magnetic moments of Tc calculated for the three P states, which are presented for each layer by the left (red), middle (green) and right (blue) bars.

symmetry appears to be robust. This issue is discussed below.

As an illustration of the magnetic properties of the studied BaTiO₃/SrTiO₃ system, the distribution of the Tc magnetic moments m_{Tc} in the subsequent TcO₂ layers near the TiS and BT interfaces is plotted in Fig. 5.4 for the three different polarizations of the BTO side. In all cases, the energetically favorable AFM ordering has the G-type, with antiparallel alignment of the nearest Tc neighbors. In general, the 10%-reduction of the Tc magnetic moments was obtained within few unit cells of SrTiO₃. These magnetic moment changes, which depend on the interface termination and P -state of BTO, can be viewed as the result of the interfacial magnetoelectric coupling. For $P = 0$, the relations between the Tc moments and tilting angles, which are shown in Fig. 5.3, can be formulated as follows: the larger the angle the smaller the moment is. This behavior seen also near the (001) surface of SrTiO₃ is typical for superexchange interaction since the magnitude of the Tc-moment decreases with increasing Tc–O–Tc angle.

Regarding the magnetic moment induced on Ti near the interfaces, this appears due to orbital hybridization with nearest (interfacial) oxygen along $[00z]$, whose nearest neighbour is Tc along the same chain of atoms: Ti–O–Tc. The Ti moment varies between 0.004 and 0.014 μ_B while the O magnetic moment is larger and varies between 0.02 and 0.08 μ_B depending on the interface composition and polarization of BTO. The two Ti atoms within the same layer are ordered antiferromagnetically to each other and ferromagnetically to both the nearest O and Tc partner along $[001]$. It should be also noted that the AFM ordering of SrTiO₃ induces the alteration of positively and negatively oriented moments within the interfacial Ti–O–Tc chains. When the BTO polarization changes, the magnetic moments of each chain change their values but the total magnetic moment calculated per magnetic supercell is close to zero, varying

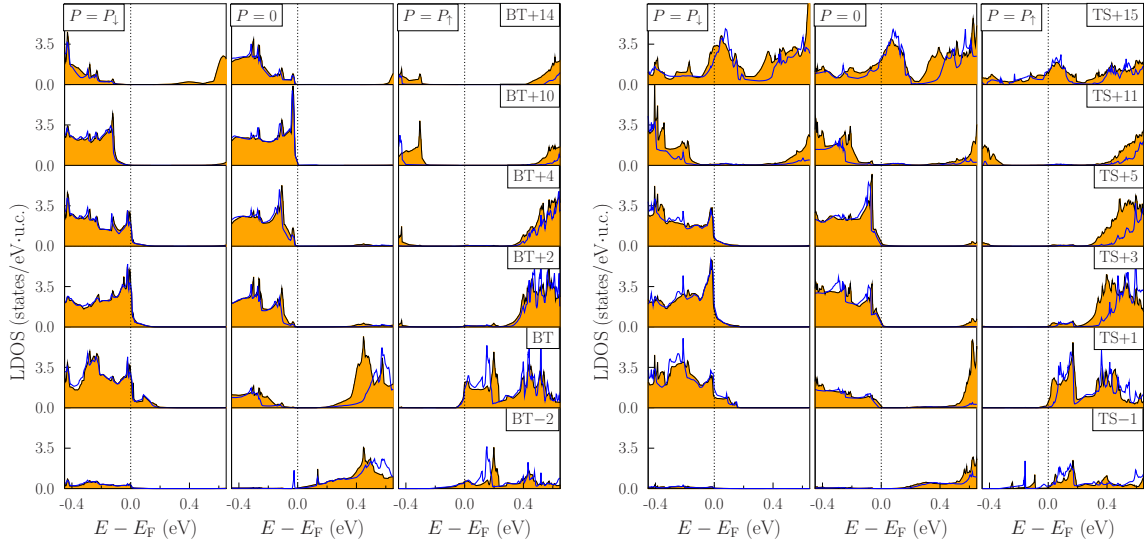


Figure 5.5: The total DOS, computed for each ABO_3 unit cell outward the BT (TiS) interface and labeled as BT (TiS+1), BT+2 (TiS+3) etc., are shown in the left (right) panels. The lower panels represent the topmost unit cell of the BTO substrate, whereas the upper panels correspond to the topmost $SrTcO_3$ cell near the (001) surface. For each P -state, the site- and orbital-projected contributions were accumulated from the two spin channels. The electronic $4d$ states of Tc were calculated within the GGA+ U , and the DOS plotted correspond to $U = 0$ (shaded area) and $U = 0.5$ eV (solid line).

within $\sum m_i < 10^{-2} \mu_B$. Thus, the magnetoelectric coupling coefficient, α , estimated for the AFM unit-cell interface area is relatively small.

On the other hand, the change of the total moment, ΔM , becomes valuable when the BTO unit-cell surface area is considered, which includes a single Ti–O–Tc chain perpendicular to the interface. Hence, $\alpha = \Delta M / (E_c \cdot A) > 0$, where A is the surface area of BTO and coercive field $E_c \sim 10$ kV/cm. For the BT interface, the largest $|\Delta M|$ of $0.12 \mu_B$ is obtained between the P_\uparrow -poled and paraelectric BTO, whereas for the TiS interface its largest $|\Delta M| = 0.05 \mu_B$ corresponds to the switching from P_\downarrow to $P = 0$. The corresponding α varies in the range $(1.8 - 4.0) \cdot 10^{-10}$ G cm²/V which is comparable to the values reported for the prototype multiferroic Fe/BaTiO₃ [60]. In the case of BTO/SrTcO₃, it should be kept in mind that each two atomic chains couple antiferromagnetically so that their contributions to the total ME effect almost cancel each other.

In the case of BTO/SrTcO₃, one should realize that robust manipulation with the BTO polarization is not obvious. Although the dielectric properties of SrTcO₃ have not been reported so far, *ab initio* calculation anticipates that the band gap is significantly smaller [151] than that of BTO. For that reason it is not clear how the coercive field of BTO affects the insulating state of SrTcO₃. This issue goes beyond the scope of our theoretical work. Nevertheless, there always is an option to change the BTO polarization, namely, by heating the system above its FE critical temperature of 390 K when BTO becomes paraelectric ($P = 0$) while SrTcO₃ remains strongly antiferromagnetic until 1000 K. Thus, the case of $P = 0$ becomes also important when the electronic properties and 2DEG are discussed.

To clarify the 2DEG effect at the BTO/SrTcO₃ interface, I discuss further the site-projected densities of states (DOS) as well as the layer-resolved DOS for each termination and for each polarization state of BTO. Each layer of the supercell contains two formula units of ABO_3 . Since the magnetic order within each layer is antiferro-

magnetic, the spin contributions were summed up. It appears that the DOS, $n(E)$, near the Fermi level (E_F) is dominated by the Tc $4d$ states hybridized with the p states of oxygen atoms. This is similar to bulk SrTcO₃ [151] but, in our case, some of these oxygen atoms are interfacial and belong to BTO. As a result, $n(E)$ of BTO/SrTcO₃ shows rather unusual features.

For the P_{\downarrow} -state of BTO and for both interfaces (TiS and BT), there is a non-vanishing density of states at the Fermi level, and the latter crosses the top of the valence band as shown in Fig. 5.5. Therefore, the system is not insulating and it should be similar to a p -doped semiconductor where holes dominate as charge carriers. Switching of the polarization to P_{\uparrow} shifts E_F towards the bottom of the conduction band. Those Tc $4d$ orbitals which were unoccupied in the bulk material are filled now, and the n -type charge carriers appear in the system. For the TiS interface and P_{\uparrow} , the population of the conduction band is smaller compared to the BT termination. Interestingly, the metalization is confined within several atomic layers near the interface, including the topmost BTO layer whose ions form chemically strong bonds with interfacial ions of SrTcO₃. These bonds show a significant degree of covalency depending on the P state of BTO.

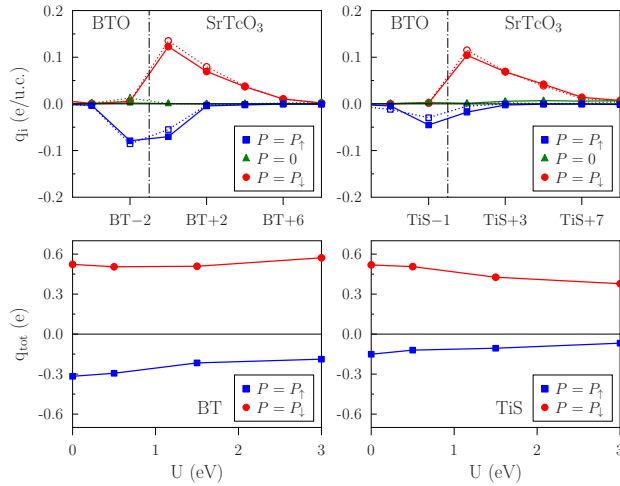


Figure 5.6: The charge induced into the band gap by polar BTO and accumulated near the BT (TiS) interface of BTO/SrTcO₃. For each complete unit cell of BTO and SrTcO₃ the DOS tails which occur in the band gap were integrated, and the results are plotted in the upper panels for each \mathbf{P} -state of BTO and for two U : $U = 0$ (solid line) and $U = 0.5$ eV (dashed line). In the lower panels, the total band-gap charge summed over all layers is plotted as a function of the U parameter.

the thickness of the region where $|q_i| > 0$ is confined within the 2–3 unit cells near the interface. For the interfacial cell, $|q_i|$ is maximal and then the charge gradually decreases outward the interface. In the case of P_{\downarrow} , one finds the hole carriers which are mostly localized within the SrTcO₃ interfacial region. The P_{\uparrow} state switches the charge character to electrons while their localization region is shifted towards the BTO side that is seen as the increase of $|q_i|$ in the topmost BTO layers. Interestingly, the paraelectric state of BTO results in marginal charges for both terminations of BTO/SrTcO₃. Thus, the 2DEG effect appears mainly due to the ferroelectricity of BTO. However, the role of the modest gap width of SrTcO₃ needs further clarification.

The electric field penetrates from BTO into the SrTcO₃ side and this penetration

In view of these results, one can conclude that the character of the 2DEG carriers is changed from electrons to holes upon the P reversal. The estimated charge, q_i , which is induced into the band gap due to polar BTO and which is accommodated in each complete unit cell i of BTO and SrTcO₃ near the interfaces, is plotted in Fig. 5.6. The DOS tails seen in the band gap in Fig. 5.5 were integrated for each i and P within the gap to the Fermi level. Although one deals with electrons in all cases, one can formally assign q_i as negative (n -type carriers) when the DOS tail comes into the gap from the conduction band and, *vice versa*, $q_i > 0$ (hole carriers) when the DOS tail comes from the valence band. The corresponding results plotted in the upper panels of Fig. 5.6 show that

can be traced by analyzing the electrostatic potential energy profile $-eV(z)$ ($e > 0$), calculated along [001] (z axis), as shown in Fig. 5.7. The profile was obtained from the Kohn-Sham effective potential by averaging the VASP outputs over the xy plane within the supercell. The points of the potential profile along [001], which are plotted in Fig. 5.7 across the BTO/SrTcO₃ slab, correspond to the layers BaO or SrO. These results were modeled for dually polar and paraelectric BTO. The plotted potentials were calculated within the Hubbard parametrization, namely, $U = 1.5$ eV.

Let us analyze the potential features. For any polar BTO side, its potential profile shows a remarkable slope, the sign of which changes upon the P reversal, as expected from electrostatics. Near the interface, the picture becomes complicated, since the depolarizing field \vec{E}_{depol} acts against the intrinsic polarization of BTO. In the paraelectric case ($P = 0$), there is a small slope of the potential, which persists in the two interfacial BTO cells due to the structural displacements discussed above. For the deeper layers of paraelectric BTO the slope is zero. The first two cells of SrTcO₃ near the interface also exhibit the structural displacements seen in Fig. 5.2 and, therefore, the polarization is locally induced even if the BTO side is paraelectric. The corresponding features of the potential are shown in Fig. 5.7.

The continuity condition for \vec{D} is fulfilled at the interface, so that $\vec{D}_1 = \vec{E}_{\text{depol}}$ in BTO and $\vec{D}_2 = 4\pi\vec{P}_{\text{ind}}$ in SrTcO₃ are equal to each other at the boundary. The results shown in Fig. 5.7 indicate that the local potential in SrTcO₃ is flat far away from the interface. In the case of P_{\downarrow} , i.e. when the hole carriers were induced into SrTcO₃, the potential slope in BTO is positive and, as a result, the potential adjustment goes smoothly. For $P = 0$, the ‘‘artificial’’ slope near the interface, from its BTO side, is modestly negative that results in a potential shift in the first layer of SrTcO₃ and, outwards the interface, the SrTcO₃ potential rapidly approaches its bulk value. In the case of P_{\uparrow} , the interface shift of the potential is about 1 eV. As a result, the electric field of BTO penetrates deeply into the SrTcO₃ side and few unit cells more are needed to screen the field and flatten the potential profile. The shift seen in the potential profile at the interface is not so dramatic compared to the free surface. It should be noted that near each surface of the composite film the potential profile exhibits polar discontinuity widely discussed in the literature, whereas in vacuum $V \rightarrow 0$ after the dipole correction.

Paraelectric BTO provides an extra option. For $P = 0$, there is no field which needs to be screened. Indeed, the DOS calculated for the two terminations (Fig. 5.5) show that the interface is robustly insulating. However, there are only some marginal and spatially extended charges seen in Fig. 5.6, which appear after structural relaxations. When the 4d orbitals of Tc were treated as strongly correlated the insulating behavior of the multiferroic system enhances, since the band gap of SrTcO₃ widens. In practice, the paraelectric state of BTO can be obtained by heating the system above the T_C of BTO and keeping the temperature below the Néel temperature of SrTcO₃. This

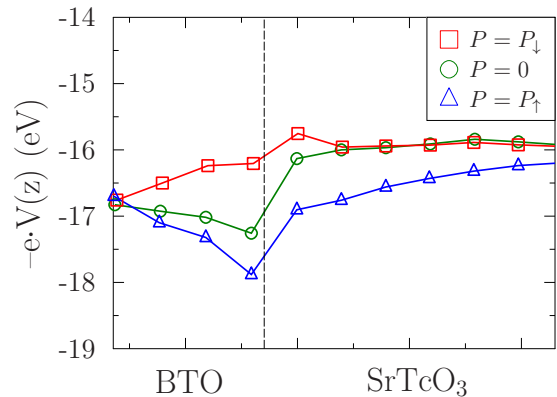


Figure 5.7: The electrostatic potential profile along [001], which was calculated for the BT-terminated interface of BTO/SrTcO₃. Each point plotted corresponds to the BaO or SrO layers while the interface is shown by the vertical dashed line. Dually polar and paraelectric BTO were modeled. The negative charge of electrons was included.

suggests another scenario of thermally switchable 2DEG in BTO/SrTcO₃, which differs from that of the P reversal in BTO. The polarization reversal switches the 2DEG charge carries from electrons to holes. In contrast, the 2DEG can be switched thermally on and off.

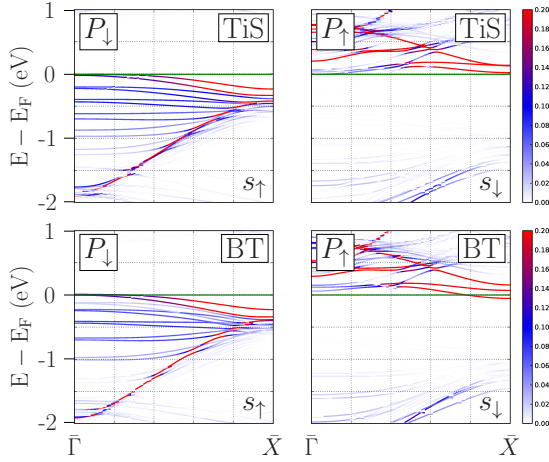


Figure 5.8: The quasi-two-dimensional band structure calculated for the BT and TiS interfaces and two polarizations P_{\downarrow} (left panels) and P_{\uparrow} (right panels) using GGA+ U with $U=0.5$ eV. The dispersion curves $E_n(\vec{k}_{\parallel})$ that contribute to the DOS at $E = E_F$ are plotted along the $\bar{\Gamma}$ - \bar{X} in-plane direction of the 2D Brillouin zone. The bands $E_n(\vec{k}_{\parallel})$ with a significant partial charge of the Tc 4d spin-up (for P_{\downarrow}) or spin-down (for P_{\uparrow}) states are presented using the colored curves where the red color corresponds to the largest partial charge.

the insulating SrO termination is energetically favorable that resembles in general the bulk properties. In this context, the geometry suggested for the BT interface, with its SrO-surface might be preferable for further experimental studies and applications. Concerning the BTO termination within the SwV model of the BT interface, it is insulating in our calculations for $P = 0$ and P_{\uparrow} and metallic for P_{\downarrow} . Nevertheless, in the latter case, the second BTO unit cell outward the surface was insulating that allows to keep the key properties of BTO.

To get a better insight into the band structure of BTO/SrTcO₃(001) and to show how the electronic states depend on the BTO polarization, I plot in Fig. 5.8 the dispersion curves, $E(\vec{k}_{\parallel})$, as a function of the in-plane \vec{k}_{\parallel} -vector along the $\bar{\Gamma}$ - \bar{X} direction in the quasi-two-dimensional Brillouin zone¹. Here, the analysis of the Tc-projected contributions of each 4d orbital shows that the spin majority d_{xz}/d_{yz} and $d_{x^2-y^2}$ orbitals of Tc (the majority and minority channels were defined in accordance with the sign of the local magnetic moment) are responsible for the hole character of the 2DEG both at the TiS and the BT interfaces calculated for the P_{\downarrow} -state of BTO. This is in accordance with the mechanism proposed to explain the formation of 2DEG. In bulk SrTcO₃, the top of the valence band is formed by the strongly spin-polarized ($> 90\%$) 4d states of Tc hybridized with the ligand p states. In BTO/SrTcO₃, the P_{\downarrow} -poled BTO induces positively charged holes in the interface layers of SrTcO₃ (Fig. 5.8). After switching to

Using the SwV geometry, one should pay attention to the properties of the free surfaces involved. In the chosen model, I assumed that both oxides are grown in complete unit cells. It means that the supercell, which mimics the BT (TiS) interface, has the SrO (TcO₂) termination of SrTcO₃(001) and TiO₂ (BaO) termination of BTO(001). Regarding SrTcO₃(001), its SrO-termination appears to be insulating, whereas the TcO₂-terminated free surface is metallic due to the dangling Tc-O bonds. By inspecting layer-by-layer DOS one can determine the electronic states of BTO/SrTcO₃(001) outward the surfaces and interfaces. This shows that the discussed 2DEG is spatially localized and the chosen supercell was thick enough to simulate the isolated interface. Simulations of the free-standing SrTcO₃(001) surface demonstrate that the metallic character is intrinsic for the TcO₂ termination, whereas

¹For the preparation of these figures, the PyProcar code provided by Francisco Muñoz was used (for details, refer to <http://sourceforge.net/projects/pyprocar>).

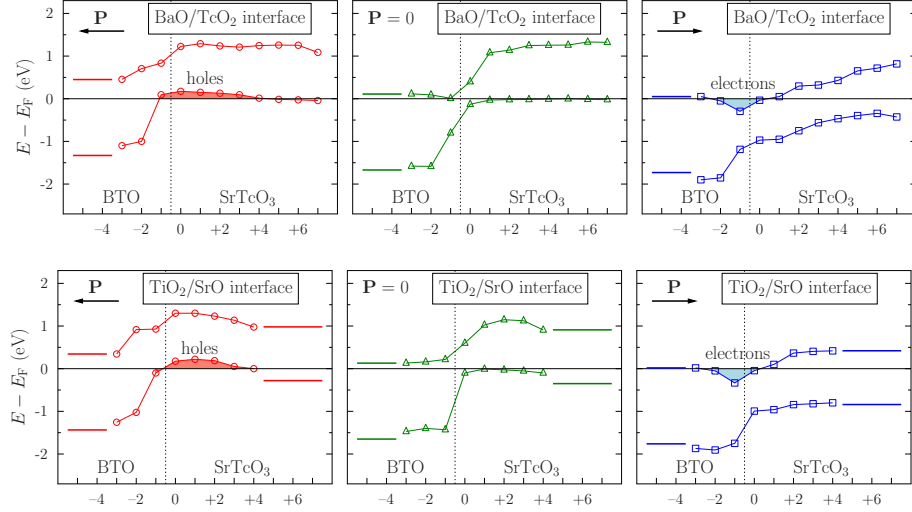


Figure 5.9: The layer-resolved energy positions of the top valence and bottom conduction bands with respect to $E_F = 0$ that are calculated for the three BTO polarizations and differently terminated BTO/SrTcO₃ heterostructures. The hole (electron) charge carriers induced in the band gap are shown by red (blue) shaded area. The interface between the two oxides is marked by the vertical dashed line. The asymptotic valence and conduction band edges far from the interface region are shown by solid horizontal lines. The GGA+ U results for $U=1.5$ eV are shown.

P_{\uparrow} , the induced charge carriers in SrTcO₃ become negative (electrons) which obviously populate the bottom of the conduction band which were formed in the bulk phase by the spin minority d_{xz}/d_{yz} and $d_{x^2-y^2}$ states. However, near the interface, the latter are shifted away from $E = E_F$ towards higher energies, so that the only contribution comes from the states whose symmetry is d_{xz}/d_{yz} . In all cases, the corresponding Tc-projected bands crossing the Fermi level are relatively flat that might suggest the importance of treating them within the limit of strong electronic correlations.

To summarize the discussion above, the robust 2DEG effect is anticipated at the two differently terminated and atomically sharp BTO/SrTcO₃ interfaces. The effect might be controlled by the ferroelectric state of the BTO substrate. Based on the presented findings, one may conclude that the electronic properties of the studied interface are governed by the induced charge carriers whose sign changes upon the polarization reversal in BTO. The suppression of polarization in BTO to its paraelectric state destroys the 2DEG. The specific structural tilting and AFM ordering of modestly insulating SrTcO₃ support the 2DEG effect, although they play a minor role compared to the polar BTO. The electronic properties of BTO/SrTcO₃ may be understood in terms of the bulk electronic states affected by the electric field of BTO, which leads to the band alignment at the interface. In Fig. 5.9, one can see how the top valence band and the bottom conduction band vary toward the interface for each termination. The upward (downward) shift of the valence (conduction) band above (below) the Fermi level, which is seen for P_{\downarrow} (P_{\uparrow}), forms the charge carriers distributed predominantly within the 1–2 interfacial cells of SrTcO₃. In contrast to polar BTO its paraelectric state prevents the charge transfer and indicates the insulating behavior of the system. In case $P = 0$, one can also clearly see how the bands flatten away from the interface, and the observed difference between the asymptotic valence band boundaries in both materials is due to the different average electrostatic potentials in BTO and SrTcO₃. The ratio between this potential step ΔV and the band gaps of both materials is one of the main factors for the emergence of the 2DEG behavior. In the studied system, as seen from the middle panels in Fig. 5.9, these three quantities (band gaps in BTO

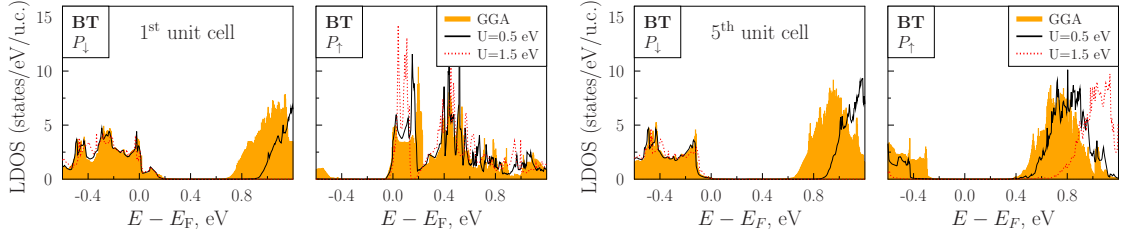


Figure 5.10: The DOS curves of the first (fifth) SrTcO₃ cell from the polar BT interface are plotted in the two left (right) panels for P_{\downarrow} and P_{\uparrow} . The $U = 0$ option is shown by shaded area and the use of $U = 0.5$ eV and $U = 1.5$ eV are shown by the solid and dashed lines, respectively.

and SrTcO₃, and the potential step ΔV) are comparable to each other. Nevertheless, the detailed picture of the 2DEG should account for the electronic orbital symmetry, spin population and correlation effects for all interfacial species.

In our study of bulk SrTcO₃ within the GGA+ U parametrization, it has been pointed out that a relatively small U parameter is needed to improve the calculated magnetic properties, in particular, the local moments and Néel temperature [151]. In this work, I analyzed the influence of electronic correlations on the 2DEG of BTO/SrTcO₃. Within the GGA+ U scheme applied on the $4d$ states of Tc the value of the U parameter was varied between 0.5 eV and 3 eV. Comparison of the calculated DOS with that of $U = 0$ (Fig. 5.10) can reveal how the degree of electronic correlations affects the whole band structure and d -states of Tc. The main effect of U is the band gap widening. This is similar to what was found previously for bulk SrTcO₃. [151] The gap widening is clearly seen in the layer-resolved DOS. For instance, the DOS corresponding to the fifth SrTcO₃ unit cell from the interface looks like the bulk material. With increasing U up to 3 eV, the band gap increases by almost a factor of three compared to $U = 0$. This agrees well with the bulk calculation where the gap value increases from 0.7 eV for $U = 0$ to 1.8 eV for $U = 3$ eV.

The total charge q_{tot} accumulated at the interface (Fig. 5.6) is more sensitive to the U variation for the TiS termination than for the BT interface. The number of holes ($q_{tot} > 0$) near the TiS interface, which are induced by P_{\downarrow} , decreases by about 0.2 electron with increasing U between $U = 0$ and 3 eV while for the BT interface its q_{tot} is stable and remains above 0.5 electron upon the U variations. Regarding the electron carriers, induced by P_{\uparrow} and shown as $q_{tot} < 0$ in Fig. 5.6, this number (which never exceeds 0.3 electron at $U = 0$) decreases gradually when the U parameter increases. However, for the BT interface, the number of induced electrons is about two times larger as compared to the TiS interface. Variation of U parameter in the range $0 \leq U \leq 3$, far above its optimal value for SrTcO₃, reveals that the 2DEG is robust against the degree of electronic correlations for both interfaces, whereas the \vec{P} reversal changes the carrier character from electrons to holes. As mentioned above, for the P_{\uparrow} -state of BTO, the electron-type 2DEG is spatially shifted towards the BTO side. This shift becomes more pronounced for the larger U and, therefore, the 2DEG is mostly localized within the interfacial BTO cell. Regarding the paraelectric state of BTO, for which the interface seems to be insulating, strong electronic correlations enhance the insulating properties since the larger U , the larger the gap of the SrTcO₃ side.

The tilting of the Tc-O-Tc bonds in bulk SrTcO₃ is a key structural feature for its antiferromagnetism. To estimate the total induced charge q_{tot} at BTO/SrTcO₃, I used the magnetic surface-cell area. After relaxation, the two pairs of tilted angles are not identical near the interface depending on the polarization and, hence, the type of

carriers transferred from BTO. It seems that these flexible bond lengths and angles may support the accumulation of extra charge near the interface. The induced charge was redistributed between several interfacial cations, oxygen atoms and interstitials of SrTcO₃ along the chemical bonds. Unfortunately, the charge variations projected on each site are too small to make accurately the corresponding charge analysis.

To conclude this part, I presented the *ab initio* calculation of the structural, magnetic and electronic properties of differently terminated interfaces between a typical ferroelectric BaTiO₃ and strongly antiferromagnetic perovskite SrTcO₃. The spin-polarized DOS projected on the interfacial species were calculated in response to the polarization state of BTO. The most important effect of polar BTO is the formation of a 2DEG where the character of charge carriers can be switched from the p- to n-type by the polarization reversal. The dominant mechanism of the 2DEG effect is electron/hole charge transfer induced from dually polar BTO into a Slater insulator SrTcO₃, where charge carries are accumulated within a few atomic layers near the interface. When BTO is paraelectric the 2DEG disappears. There is another important factor needed to create the 2DEG conditions: a modest band-gap width of SrTcO₃ (less than 1.5 eV) which allows the band bending effects to induce a shift of electronic states that is sufficient for the emergence of the 2DEG. It might happen that, for abnormally large gap in SrTcO₃, one of the two interface terminations would become completely insulating while, for another one, the 2DEG may be still conserved only for P_{\downarrow} .

The tilting of oxygen octahedra and related AFM ordering in SrTcO₃, which support the insulating bulk properties, might also contribute to the 2DEG effect. The charge induced from polar BTO is redistributed between several interfacial cations, oxygen atoms and interstitials of SrTcO₃ along the chemical bonds. Here, the tilting angles and the bond lengths seem rather flexible to accommodate all excessive charges of both characters. For the BaO/TcO₂ termination, because of its interfacial Tc and flexible tilting, one can anticipate that the 2DEG effect is more pronounced and stable with respect to the model variations, such as the film thickness and degree of electronic correlations. This opens an opportunity to control the transport properties of BaTiO₃/SrTcO₃ either by switching the polarization state of BTO or, alternatively by heating the system above the FE transition temperature to the paraelectric state which suppresses the 2DEG.

It should be noted that both oxides studied here are assumed to grow in complete unit cells. Since the surface termination and interfacial composition are correlated, then, using some appropriate bottom termination of the substrate, the target BaO/TcO₂ termination and, hence, the 2DEG can be designed. So far, the 2DEG effect was reported for the TiO₂/LaO termination of LaAlO₃/SrTiO₃ [12], which is formed by a paraelectric and paramagnet and which is not externally switchable. The results of this work suggest that the robustly controlled 2DEG may appear at the BTO/SrTcO₃ interface. The anticipated 2DEG is localized within the few-nm-thick layer. Since the 2DEG effect is ferroelectrically driven, it can be (i) switched off completely by heating or (ii) adjusted from the hole-type carriers to electrons by the P reversal of BTO. These findings offer further promising applications in spintronics and oxide-based nanoelectronics.

5.2 ME coupling in Co/PZT (001)

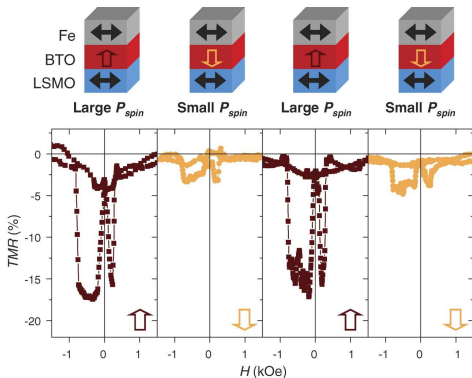


Figure 5.11: Change of the TMR magnitude under the ferroelectric switching in the multiferroic Fe/BTO/LSMO tunnel junction (reproduced from [133]).

PbZr_{0.2}Ti_{0.8}O₃ (Fig. 5.12). In both cases, the observed phenomenon is attributed to the change of the spin polarization of the tunneling electrons due to the strong interfacial ME coupling effect at the interface between the oxide barrier and the simple metal. In case of LSMO/PZT/Co, another interface between La(Sr)MnO₃ (LSMO) and PZT, as the authors suggested [11], may not contribute too much to the effect.

Theoretical studies of the Co/PZT interface from first principles were not reported so far. It would be worthwhile to investigate the role of the Zr impurities in PZT on the interfacial bonding and the magnetoelectric coupling anticipated for this multiferroic system. In this work, both [001]-oriented Co/PZT and Co/PTO (PbTiO₃) interfaces were computed using *ab initio* methods, focusing on the electronic mechanism of the interfacial magnetoelectric coupling (MEC) and its role in the spin-dependent transport properties of related tunnel junctions.

Experimentally, the SrTiO₃ (001) (STO) substrate was used to grow epitaxially the multiferroic LSMO/PZT/Co structures [11]. Since the in-plane STO lattice parameter (3.898 Å) is very close to that of bulk PTO (3.892 Å), $a=3.892$ Å was fixed for all supercells, keeping $c/a = 1.071$ within the ferroelectric side before relaxation. This configuration may simulate epitaxial growth on the STO substrate, as performed in [11]. Thus, the starting intralayer displacements between the cations and anions of PTO were optimized as 0.45 Å and 0.33 Å for the PbO- and TiO₂-layer, respectively. This is in reasonable agreement with experiment. The Co/PTO (001) interface was simulated by supercells which contain 5 u.c. of PTO stacked along [001] and a different number, n , of cobalt layers, as shown in Fig. 5.13. Additionally the effect of Au-capping was simulated by adding 2 Au layers above the Co _{$n=5$} structure that allows to exclude the effect from the ferromagnetic Co surface. Each Co/Au layer contains two atoms per unit cell surface area of PTO. Vacuum of about 15 Å added above the metallic

Multiferroic tunnel junctions (MFTJ) with ferroelectric barriers offer the possibility of tuning the spin-dependent electronic transport by an external electric field, which, in the presence of a strong interfacial magnetoelectricity, fabricates the so-called four-state memory device. For example, recently studied Fe/BTO/LSMO tunnel junction [133] demonstrates a negative tunneling magnetoresistance effect which can be controlled by the electric polarization of the BTO barrier (Fig. 5.11). Similar effect was later observed in LSMO/PZT/Co tunnel junction [11] where the sign of the TMR effect can be robustly switched by the polarization reversal in the ferroelectric PZT barrier which has a composition

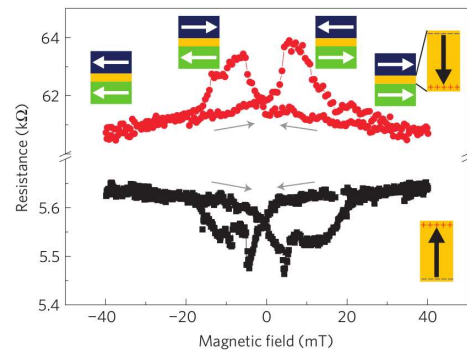


Figure 5.12: Change of the TMR sign under the ferroelectric switching in the multiferroic LSMO/PZT/Co tunnel junction (reproduced from [11]).

layers is sufficiently large to eliminate any interactions between the periodic images of the supercell along the $[001]$ axis.

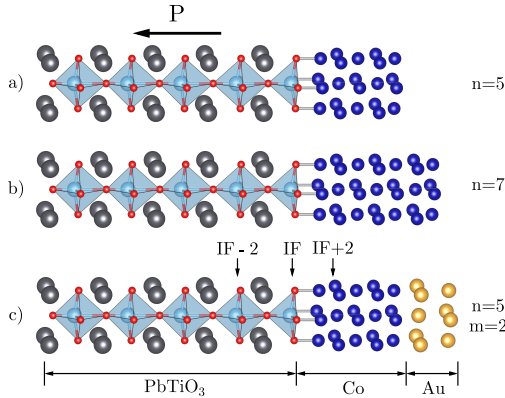


Figure 5.13: The side view of the $(\text{Co}_2)_n/(\text{PbTiO}_3)_5$ (a,b) and $(\text{Au}_2)_m/(\text{Co}_2)_n/(\text{PbTiO}_3)_5$ (c) supercells, where n and m denote the number of cobalt and gold layers, respectively. The interfacial TiO_2 -layer that terminates PTO is labeled IF, whereas the Co layers outward the interface are labeled IF+1, IF+2 and so on. The polarization of PTO, P_\downarrow , is shown by the horizontal arrow.

interface for each polarization state. The most important issue is, however, the variation of the the electronic states and magnetic properties of the Co/PTO system upon the polarization reversal.

The crystal structure of the Co film in the chosen model needs special attention. Each interfacial Co atom is relaxed above the oxygen ion, which belongs to the TiO_2 termination of PTO, as Pantel *et al.* [11] suggested. Surface X-ray diffraction studies of thin BaTiO_3 (BTO) films [47, 48] grown on $\text{Fe}(001)$ also show that the interface bonding is mediated between the O atoms atop the Fe atoms. These experimental findings, confirm all previous *ab initio* studies for the energetically favorable termination of Fe/BTO [50, 58, 60, 61, 64, 65], Co/STO [172] and Co/BTO [173]. For thin Co films on PTO (001), the atomic arrangements of Co formally mimic the face centered tetragonally distorted structure, with the in-plane lattice parameter of 3.892 \AA that corresponds to the in-plane Co–Co distance of 2.75 \AA . In the bulk hcp-Co, the nearest Co atoms are separated by 2.51 \AA . However, experimental studies on the epitaxial cobalt films with the *fcc* structure give 2.82 \AA for the lattice constant, and, therefore, the epitaxial Co film is subject to in-plane compressive strain of approximately 2.5%.

Before studying the Co/PZT interface, Zr-doped bulk $\text{PbZr}_x\text{Ti}_{1-x}\text{O}_3$ (PZT) was simulated within the supercell approach. The structure and ferroelectricity of bulk PZT critically depend on the Zr/Ti composition. Below the concentration $x < 0.52$, it adopts tetragonally distorted perovskite structure, with the spontaneous polarization

The atomic positions of the first three PTO unit cells next to the interface were fixed during the relaxation to conserve the chosen electric polarization state, whereas all atoms of the two PTO unit cells near the interface were allowed to relax (for details, refer to [51]). To mimic the polarization reversal, the procedure described in [50] was applied. That allows to compute and compare the two cases of polarization in PTO: P_\downarrow and P_\uparrow , where the cations and anions of each atomic layer were displaced along $[001]$ in accordance with the polarization state. For the polarization state P_\downarrow , for instance, all oxygens are placed above the cations in each monolayer, as shown in Fig. 5.13, and *vice versa*. Regarding the Co side, the positions of all metal atoms in the supercell were fully optimized along the z axis. After that, one can compare the structural changes near the

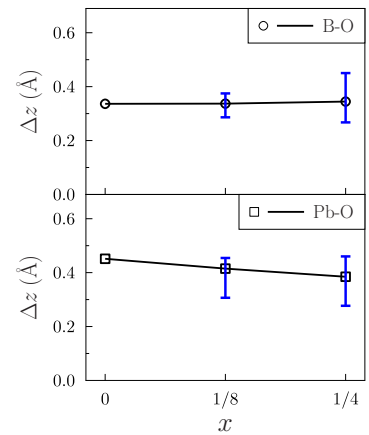


Figure 5.14: Relaxed ionic displacements Δz in $\text{PbZr}_x\text{Ti}_{1-x}\text{O}_3$ calculated for $x = 0, 1/8$ and $1/4$. Solid line corresponds to the Δz average. The variation range of Δz in the supercell is marked by vertical bars.

of $(50 - 60) \mu\text{C}/\text{cm}^2$ oriented along $[001]$ [174]. In this work, the two compositions $x = 1/8$ and $x = 1/4$ were modelled using the $(2 \times 2 \times 2)$ perovskite supercell, which contains 8 unit cells of PTO. The experimental lattice parameters were used. For $x = 1/8$, one of the Ti cations was replaced by Zr and the positions of all atoms were completely relaxed. For $x = 1/4$, there are five possibilities to distribute two Zr atoms across the eight B sites. Each case was inspected after relaxation. The ferroelectric displacements, Δz , are important in this context, while the presence of Zr changes them locally. In particular, for a single Zr impurity in the supercell the relaxed Δz is enhanced for the nearest Ti cations, whereas it becomes slightly diminished for the next nearest Pb cations. In general, the Zr doping leads to variations of Δz across the supercell. The larger x , the stronger vary the Δz , as shown in Fig. 5.14. For the two Zr dopants ($x = 1/4$), after the configurational average it was found that the Δz displacements for the B cations were not changed significantly, while for the A cations the corresponding Δz were moderately decreased.

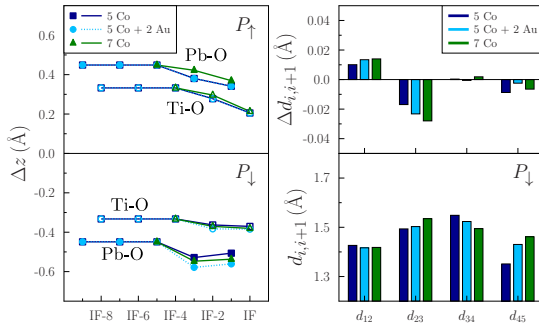


Figure 5.15: The intralayer cation-anion displacements along $[001]$, $\Delta z(\text{Pb} - \text{O})$ and $\Delta z(\text{Ti} - \text{O})$, calculated for the PTO side of the interface, are shown in the left panel for the electric polarization directions P_\uparrow and P_\downarrow . The interlayer distances in the Co film for the P_\downarrow -state and its variations $\Delta d_{i,i+1}$ upon the polarization reversal are plotted in the right panel for varied number of cobalt monolayers. The case of the two-ML-thick Au-capped Co/PPTO is shown as well.

most BO_2 layer of PZT that is put in contact with the cobalt film. This effective doping can be achieved by replacing randomly one of every four titanium cations by a Zr impurity. Thus, one can mimic the effect of substitutional disorder on the ferroic and structural properties of Co/PZT (001). The topmost 1 u.c.-thick PZT oxide layer and all 7 metal layers, each consisting of 8 atoms, were fully relaxed.

As the first step, the structure of the Zr-doped Co/PZT interface was studied after atomic relaxation and compared to that of the undoped Co/PPTO.

The intralayer ionic displacements in the PbO- and Ti(Zr)O₂-layers along $[001]$ can characterize the local ferroelectric properties. Near the Co/PPTO interface in the polarization state P_\downarrow , i.e. for \vec{P} pointing away from the Co film, the cation-oxygen displacements were increased after relaxation (especially, for the second PbO layer IF-1) as compared to the bulk displacements. This is shown in the lower left panel of Fig. 5.15. However, the same system in the polarization state P_\uparrow shows a noticeable local suppression of ferroelectric displacements for the interfacial TiO₂ layer IF, as shown in the upper left panel of Fig. 5.15. It should be noted that the state P_\downarrow is

The Co/PZT (001) interface was simulated with two different models. The first model corresponds to a digital ZrO monolayer, whose position near the interface was varied using the supercell shown in Fig. 5.13c. When ZrO₂ terminates PTO(001), it corresponds to the composition $2 \times \text{Au}_2 / 5 \times \text{Co}_2 / \text{ZrO}_2 / \text{PbO} / \text{TiO}_2 \dots$. Another type of structure can be obtained by replacing the third PTO layer from the interface by a ZrO₂ monolayer. Obviously, the Zr dopant forms in this case a periodically repeated plane of ZrO₂ perpendicular to the growth direction.

For the second model of Co/PZT (001), I started from a $(2 \times 2 \times 2)$ bulk perovskite supercell. It contains 4 u.c. of perovskite in the $x - y$ -plane and allows to simulate the $\text{Zr}_{0.25}\text{Ti}_{0.75}\text{O}_2$ composition in the top-

energetically favorable by 1.2 eV per supercell which is shown in Fig. 5.13 (c). The energy disbalance between the two polarizations is qualitatively similar to the case of the TiO_2 terminated free PTO(001) surface discussed previously in [50]. The perovskite surface prefers the atomic arrangement with oxygen ions placed slightly above the larger in size cations to form a flat charge isosurface. Thus, for the Co/PTO interface, its structural features appear rather different from the PTO (001) surface. Obviously, the interfacial Co-O bonds and related charge screening from the multiple cobalt layers introduce all structural changes, which are plotted in Fig. 5.15 and which, in general, were not expected from the ferroelectric surface consideration.

For the Co/PZT interface, with the structure of a digital alloy, i.e. when Zr substitutes all Ti in the layer IF or IF-2, the relaxed displacements Δz were enhanced locally almost by factor of 2 on the sites occupied by Zr atoms even for the energetically unfavorable polarization state (Fig. 5.16). These results were supported by the calculations for the 2×2 in-plane supercell which mimics the 25%-Zr composition in each TiO_2 layer. In this case and for layer IF, the corresponding Δz increases locally by $\sim 56\%$. Such behaviour has been already expected from the simulations of the bulk alloy $\text{PbZr}_x\text{Ti}_{1-x}\text{O}_3$.

The electronic properties of multiferroics strongly depend on the interfacial bond length, which, in our case, are the interatomic distances between Co and oxygen. For pure Co/PTO, the corresponding distance, $d(\text{Co}-\text{O})$, depends on \vec{P} and increases from 1.90 Å to 1.98 Å upon switching, as shown in Table II. The variation of the Co–O bond length affects the orbital hybridization changing, therefore, the interplay between ionic character and covalency. When the Zr impurity is placed at the interface the \vec{P} -dependent effect is enhanced. For the latter case, a remarkable change of the Co–O distance upon the polarization reversal is obtained within the digital alloy model: the bond length changes from 1.91 Å to 2.98 Å, i.e. by more than 1 Å. This remarkable structural effect of doping is directly related to the large ionic radius of the Zr cation compared to that of Ti. The inherent feature of Zr-based oxide, namely, large ionic displacements in the ZrO-planes, together with the polarization reversal brings the interface oxygen atoms away from the Co cations for the P_{\uparrow} -state. The interface bonding is mediated, therefore, only through the Co-Zr pairs. On the other hand, the Zr digital doping in the third perovskite layer, IF-2, changes the interfacial bond length insignificantly. This implies the localized character of the effect. The predicted structural features should play an important role for the fabricated composite multiferroics, where the Zr impurities are randomly distributed across the PZT interface.

Using the 2×2 in-plane supercell, I simulated also the 25%-Zr concentration at the interface, which mimics the experimental composition [11]. After relaxation both interfaces Co/PTO and Co/PZT possess some degree of roughness seen as variation of their Co–O distances in Fig. 5.17. Whereas the roughness of the Co/PTO interface

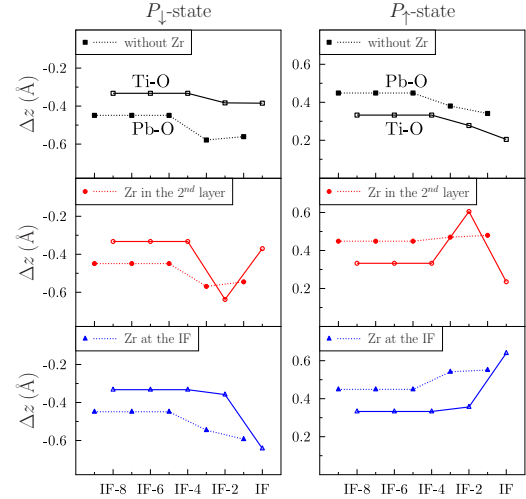


Figure 5.16: The intralayer displacements $\Delta z(\text{Pb}-\text{O})$ and $\Delta z(\text{Ti}-\text{O})$ in the ferroelectric $\text{PbZr}_{0.2}\text{Ti}_{0.8}\text{O}_3$ side calculated for two polarizations P_{\downarrow} (left panel) and P_{\uparrow} (right panel). The two different positions of the Zr impurity in PZT are shown in comparison with the pure Co/PTO interface.

Table II. Interatomic distance $d(\text{Co-O})$ and energy difference $\Delta E = E(P_{\uparrow}) - E(P_{\downarrow})$ of the Co/PTO and Co/PZT interfaces, calculated within the digital alloy model. For Co/PZT, the two different Zr positions are labeled by IF and IF-2 that corresponds to the interface and third PZT layer, respectively.

	Co/PTO	Co/PZT (IF-2)	Co/PZT IF
$d_{\text{Co-O}}^{P_{\downarrow}}$ (Å)	1.897	1.890	1.913
$d_{\text{Co-O}}^{P_{\uparrow}}$ (Å)	1.980	2.003	2.981
ΔE (eV/u.c.)	1.21	1.30	2.08

varies within 5–6%, the presence of 25%-Zr leads to rather significant variations in the Co–O bond length of up to 40–50% for the energetically less preferable P_{\uparrow} -state. Doping with larger Hf cations, which are isovalent to Zr and Ti, was analyzed as well. Surprisingly, the Co/PHT system with its larger species at the interface is much closer structurally to the Co/PTO system than to Co/PZT. In all three systems studied here with the use of extended supercells, the average Co–O bond length increases under polarization reversal. The result is consistent with that of the digital alloy model.

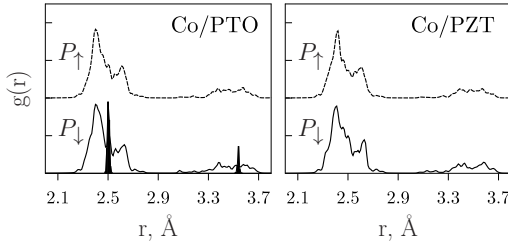


Figure 5.18: The Co–Co radial distribution functions calculated for the Co/PTO and 25%-doped Co/PZT interfaces in comparison with that of bulk hcp-Co which presented as sharp shaded peaks in the left panel.

contraction between the topmost atomic planes. The side effect from the surface on the interface region was significantly weakened or even completely removed in our calculations for $n = 7$ and for 5 Co ML capped by a Au bilayer.

For the (1×1) in-plane supercell with two cobalt atoms in each Co layer, minor changes of $d_{i,i+1}$ upon the polarization reversal are anticipated, depending on the Zr(Hf) position beneath the interface. The more degrees of freedom the Co layers had in the studied model, the more deviations were obtained. For instance, the use of (2×2) supercell can already result in the Co structural reconstruction. The relaxed Co layers are not only contracted along $[001]$, as one would expect because of strain, they also show rather noticeable in-plane displacements. This leads to a structure which differs considerably from the tetragonally distorted *fcc* arrangement (Fig. 5.13).

To illustrate the structural differences caused by this reconstruction, I performed *ab initio* molecular dynamics (MD) simulations, implemented in VASP, on the statically

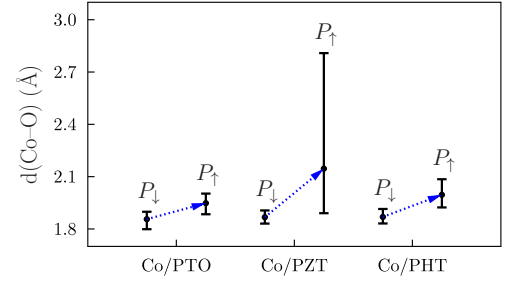


Figure 5.17: The Co–O distances for Co/PTO and also for 25% Zr(Hf) doped Co/PZT (Co/PHT) interfaces, modeled within the (2×2) in-plane supercell. The average values $\langle d \rangle$ are shown by points and the spread of d is marked by vertical bars. Changes of $\langle d \rangle$ due to polarization reversal are additionally shown by dashed arrows.

There is another important issue concerning the structure of the cobalt film. For all studied structures, the distance between atomic planes of cobalt ($d_{i,i+1}$) shows some pronounced variations along the $[001]$ direction. Near the interfaces the interlayer separation, d_{12} , between the first two Co ML is considerably less than the next interlayer separation d_{23} . For the case of Co/PTO this is shown in the right panel of Fig. 5.15. For 5 Co ML ($n = 5$), the effect of the free cobalt surface is observed as a remarkable contraction between the topmost atomic planes. The side effect from the surface on the interface region was significantly weakened or even completely removed in our calculations for $n = 7$ and for 5 Co ML capped by a Au bilayer.

relaxed (2×2) supercells. For the MD simulations, the Γ -point Brillouin-zone sampling was used. To obtain adequate statistics for thermodynamic equilibrium, I ran the simulations with a total duration of 1.5 ps and a time step of 1 fs at finite temperature equal to 1 K. All metal atoms were allowed to move. The first 0.1-ps outputs were excluded from the statistics. As the MD output, the radial distribution functions (RDF) were computed to characterize the average Co-Co distance between nearest neighbors (Fig. 5.18). The similarity of RDF seen in all simulations indicates that the same type of structure in the cobalt film was obtained. Comparison of the main RDF peak for the reconstructed cobalt film with that of bulk *hcp* Co shows that the average nearest neighbor Co-Co distance in Co/PTO and Co/PZT nanostructures is close to the bulk value 2.51 Å. One can conclude that the distorted *hcp* crystal structure is stabilized in the epitaxially grown few-nm-thick Co film. However the *c*-axis direction differs from [001]. Indeed, for all studied interfaces, the characteristic *hcp*-motive could be identified which is inclined to the interface, as shown in Fig. 5.19 for the case of Co/PTO (P_{\downarrow} -state). The estimated lattice parameters a and c/a of this *hcp* unit cell are very close to the corresponding values for the bulk material, although the unit cell itself is moderately distorted with respect to the ideal structure.

The “easy growing direction” for this *hcp*-structure can be described by two angles: the polar angle θ measured relative to [110] direction and the azimuthal angle φ determined relative to [100] in-plane axis. The absolute values of the so-defined angles θ and φ are close to 45° . Within the four-fold in-plane C_{4v} symmetry of the metallic layer, the orientation of the *hcp*-element and, generally, the structure of the cobalt film are not affected by Zr(Hf)-doping, nor by the polarization reversal. It would be worthwhile to study the structure of thick cobalt films experimentally.

By inspecting the distribution of the calculated magnetic moments in the Co film for the three cases of Co/PTO shown in Fig. 5.20, one can see that for the supercell with $n = 5$ there is the surface effect, which is significantly weakened when n is increased. For both polarization directions in PTO (P_{\downarrow} and P_{\uparrow}), the Co film is strongly ferromagnetic.

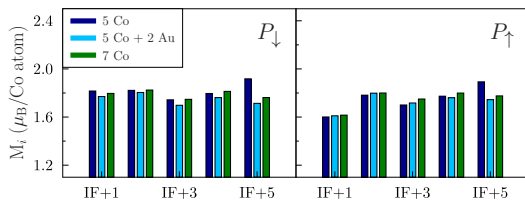


Figure 5.20: The distribution of the magnetic moments in the Co film along [001] calculated for the two polarizations P_{\downarrow} (left panel) and P_{\uparrow} (right panel) of the PTO substrate. The results for the three different Co films (see Fig. 5.13) are shown.

distance for the P_{\uparrow} -state (see Table I). It is instructive to have a look at the spin density imbalance $[n^+(\mathbf{r}) - n^-(\mathbf{r})]$ distribution for the two polarized cases (Fig. 5.21). Slices of this spin density within the (010) plane cutting through the Ti atoms and the neigh-

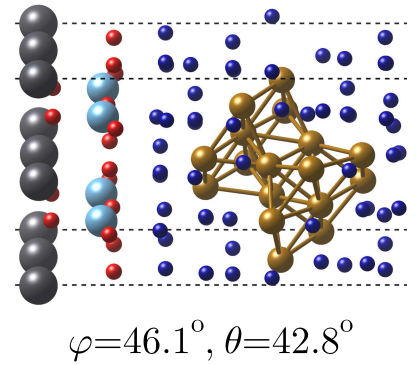


Figure 5.19: The formation of the Co-*hcp* structural motive near the Co/PTO (001) interface for the polarization P_{\downarrow} .

For the Co/PTO interface, a relatively strong magnetoelectric coupling is to be anticipated. There is a noticeable change of the magnetic moments in the interfacial Co layer IF+1 under polarization reversal (right panel of Fig. 5.20). On the other hand, as the system is switched to P_{\uparrow} , the induced magnetic moment of about $0.3 \mu_B$ appears on the topmost Ti while the small magnetic moments induced on interfacial oxygens became weaker due to the larger Co-O distance

boring oxygens explicitly show that the overall spin polarization in the topmost TiO_2 layer is always opposite to that of Co, although its magnitude is significantly higher for the P_{\uparrow} -state. Obviously, the magnetoelectric coupling shows the localized character since it was observed in our calculations within the two atomic layers at the interface, namely, IF and IF+1 as shown in Fig. 5.13. The total magnetic moment, ΔM_{IF} , counted for the Co/PTO supercell as $\text{Co}_2 \cdot \text{TiO}_2$, decreases by $0.65 \mu_B$ upon polarization reversal. The observed MEC effect can be ascribed to the spin-dependent charge transfer from the Co film into the Ti d orbitals. Before, the same effect was discussed and illustrated for such multiferroics, as Fe/BTO and Fe/PTO [60, 61].

Based on the geometry of the interface bond orbitals and their symmetry, one may conclude that the dominant interaction at the interface is the hybridization between Ti and Co d states, as well as between O p and Co d states. The results of our *ab initio* study indicate that this interaction induces magnetic moments on the interfacial Ti sites which are antiparallel to the magnetic moments of the neighboring Co cations. For the P_{\downarrow} -state, the topmost Ti cation is relatively further away from the first Co layer, so that the corresponding orbital hybridization is suppressed. The Co-O bond distance, however, allows for strong $p-d$ hybridization, which leads to the marginally induced positive magnetic moments on oxygen. As the ferroelectric polarization is reversed to the state P_{\uparrow} , the Co-O separation increases that reduces the O moments, and, more importantly, the Ti cations reach the proximity of the ferromagnetic Co layer. Due to the hybridization between the d states of these cations the negative spin polarization on the Ti site is significantly enhanced and, thereby, contributes to the MEC. The spin polarization of the interfacial Co itself is not much affected by this process.

It is worthwhile to study the effect of Zr on the strength of MEC at the Co/PZT interface. The results obtained within the digital alloy model (Fig. 5.22) indicate a possibility of tuning the ME coupling at the interface by changing the position of the impurity. In case of a Zr atom placed in the third atomic layer away from the interface, the total change in the interfacial magnetization is slightly enhanced in comparison with the original undoped system ($\Delta M_{\text{IF}} = -0.68 \mu_B$). This enhancement of the interfacial MEC effect is related to (a) the local increase of the ionic Ti-O displacement at the interface by 0.03 \AA compared to the pure PTO substrate and (b) a contraction of the Ti-Co direct exchange distance, which facilitates the spin-dependent charge transfer. A larger effect can be achieved by realizing the doping directly on the interface. Because of the lower degree of localization of Zr d orbitals only a small magnetic moment is induced on the topmost Zr-site for the P_{\uparrow} -state: $-0.077 \mu_B$ against $-0.292 \mu_B$ on Ti at the Co/PTO interface (Fig. 5.22). On the other hand, the MEC effect is now spanned over three atomic layers, including the second cobalt layer IF+2. The estimated value $\Delta M_{\text{IF}} = -0.58 \mu_B$ is again very close to that of the pure Co/PTO interface ($-0.65 \mu_B$).

This picture is supported by the simulations of the 25%-doped interface, for which the induction of magnetic moments on the topmost B -sites ($B=\text{Ti, Zr, Hf}$) and charge transfer from the metallic side are expected, similar to the mechanism described above for the pure Co/PTO system. The induced moments on the 4d (5d) cations are twice

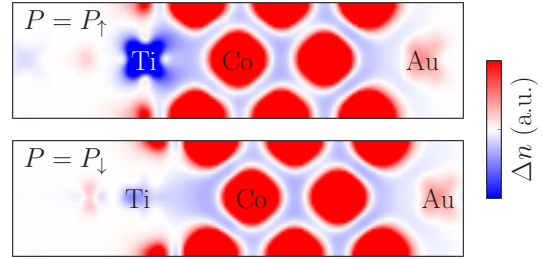


Figure 5.21: The spin density imbalance $[n^+(\mathbf{r}) - n^-(\mathbf{r})]$ distribution (in arbitrary units) near the Co/PTO (001) interface for the P_{\downarrow} - and P_{\uparrow} -states. The density is calculated in the (010) cross-section of the supercell.

as large as that found for the digital alloy arrangement of impurities: $-0.141 \mu_B$ and $-0.131 \mu_B$ for Zr and Hf impurities, respectively. The total change of the interfacial magnetic moment for the 25%-doped case is confined to 2-3 atomic layers and lies in the range from $-0.74 \mu_B$ to $-0.83 \mu_B$ per surface area of 1 perovskite unit cell.

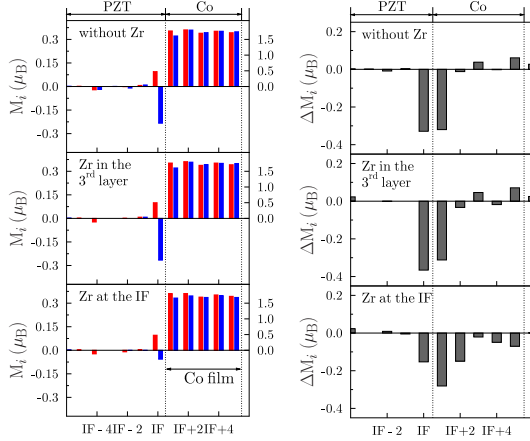


Figure 5.22: The layer-resolved magnetic moments M_i (left panel) of atomic planes near the Co/PZT (001) interface (marked with the vertical dashed line between IF and IF+1 ticks), as compared to chemically clean Co/PTO (001). The polarizations P_{\downarrow} (P_{\uparrow}) are shown by red (blue) bars. The total change of the magnetization $\Delta M_i = M_i(P_{\uparrow}) - M_i(P_{\downarrow})$ for each atomic layer in all three systems is presented in the right panel.

of the doped ferroelectric should be different from the bulk value of the pure PTO. Indeed, according to experimental data [175] the coercive field of the PZT compound with 50/50 composition equals 10 kV/cm, which means that for the composition studied in this work this value could be lower than previously assumed and correspondingly the estimated MEC coefficient for the Co/PZT interface would be even higher. It would be beneficial to get more insight into the actual values of E_c for the considered structures.

The Co/PHT interface might be applicable for two reasons. Firstly, the MEC effect on this interface exceeds that of both Co/PTO and Co/PZT structures (Fig. 5.23) and, secondly, the interface itself is characterized by a moderate roughness (Fig. 5.17), which is beneficial for growing well-ordered nanostructures. Furthermore, the ferroelectric parameters of the PHT perovskite alloy [176] are comparable to the characteristics of the widely used PZT. This can motivate the researchers to grow the PHT based multiferroic interfaces.

Since the MEC effect expected for the studied interface has an electronic origin, it is necessary to understand, how the electronic properties of the interface depend on the ferroelectric polarization. From the site-projected density of states (Fig. 5.24) one can see that there is an injection of states in the minority d channel in the energy range from $E_F - 2.0$ eV to E_F leading to enhanced induced moments on the B -sites for the P_{\uparrow} -state, whereas the occupied d states are not significantly modified for the opposite polarization. This is accompanied by only minor changes of the electronic states for the interfacial Co atoms. The spin-dependent charge transfer across the multiferroic interface involves the t_{2g} orbitals with the d_{yz} (d_{xz})-symmetry, which provide the strongest overlap between the electronic states of the transition metal cations. The Ti d_{yz} orbitals are dominating in this process, since the d states of Zr (Hf) dopants are

From the change of the calculated interfacial magnetic moments $M_{\text{IF}}(P_{\downarrow})$ and $M_{\text{IF}}(P_{\uparrow})$ (Fig. 5.23) one obtains the value of the empirical MEC coefficient α using expression $\alpha = \Delta M_{\text{IF}} / (A E_c)$, where the coercive field is taken to be equal to 33 kV/cm (valid for bulk PTO) and A is the surface area across the interface. Our findings demonstrate the possibility of tuning the MEC effect as well as the interface structure by introducing impurities on B -sites with larger ionic radius, such as Zr and Hf dopants. Although the induced magnetism on 4d (5d) transition metal cations is rather marginal, enhancement of the spin polarization of the neighboring 3d cations compensates for this and the resulting MEC strength averaged over a large surface area differs by 7% at most from the undoped system. However, one could argue here that the coercive field E_c

relatively delocalized and, as expected, contribute marginally to the LDOS near the Fermi level.

Based on the electronic features of the studied interface, the recently observed reversible change of sign of the TMR effect in multiferroic LSMO/PZT/Co tunnel junctions [11] might be explained within the limitations of the Julliere model [142]. The latter allows to estimate the TMR ratio from the spin polarizations $SP_{L,R}$ of charge carriers on the two opposite interfaces of the considered junction:

$$\text{TMR} = \frac{R_{\uparrow\downarrow} - R_{\uparrow\uparrow}}{R_{\uparrow\downarrow}} = \frac{2 SP_L \cdot SP_R}{1 + SP_L \cdot SP_R}, \quad (5.1)$$

where $R_{\uparrow\uparrow}$ and $R_{\uparrow\downarrow}$ are the resistances for the parallel and antiparallel alignment of the lead magnetization, respectively. In this part of my work, I study the interface between Co and PZT and the sign of the corresponding spin polarization can be related to the spin imbalance $SI = n_{\uparrow}(E) - n_{\downarrow}(E)$, i.e. the difference between the spin-up and spin-down density of states for the chosen energy.

The fact that the TMR effect is inverse for the polarization pointing towards the Co film (P_{\uparrow} in our set-up) indicates opposite signs of the considered spin polarizations. Since the LSMO/PZT interface is not expected to be affected by the ferroelectric side due to almost 100% half-metallic character and high magnetic stability for the chosen composition $x = 0.33$, one may conclude that the spin polarization of the other interface (Co/PZT) should be negative for the P_{\uparrow} -state to explain the observed effect. Indeed, as seen from the energy-dependent spin imbalance SI near the Fermi level (Fig. 5.25), the d_{yz} states of the interface Ti cations acquire a large negative polarization in the energy range from $E_F - 2.0$ eV to E_F . Due to the large overlap and, accordingly, the strong hybridization between the Co and Ti d orbitals (also responsible for the MEC effect), one would expect the tunneling electrons at this interface to be predominantly of d-character with $SP_R < 0$ for a moderate negative bias voltage that samples the above-mentioned energy range.

Since the TMR effect has been observed to change its sign under the polarization reversal [11], it can be assumed that the considered interface becomes positively spin-polarized for the P_{\downarrow} -state. In this case, the Ti cations are too distant from the first cobalt layer and the orbital hybridization is suppressed, whereas the Co-O bond is now shorter and the orbital hybridization in the Co-O pair is enhanced. Therefore, the tunneling is likely to be governed by the delocalized s and p states of these cations. In this work, the largest contribution to the spin polarization was identified, coming mainly from the p states of oxygen, and this contribution is positive in the energy range from $E_F - 2.0$ eV to $E_F - 0.7$ eV for the P_{\downarrow} -state (Fig. 5.25). The combined sp states of cobalt cations contribute only marginally. Upon the polarization reversal the

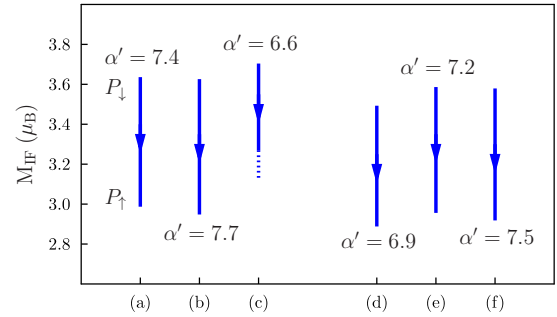


Figure 5.23: The total magnetic moment of the interfacial composition $\text{Co} \cdot \text{BO}_2$ ($B=\text{Ti}, \text{Zr}, \text{Hf}$) in the digital alloy model: (a) Co/PZO, (b) Co/PZT with Zr in the interface layer and (c) Co/PZT with Zr in the third layer as well as for the larger supercells: (d) Co/PZO with reconstructed cobalt film, (e) Co/PZT and (f) Co/PHT with 25% Zr/Hf-doping in the interface layer, respectively. Changes of the magnetization under the polarization reversal from P_{\downarrow} to P_{\uparrow} are shown by two points one above another and an arrow connecting them. The estimated values of the MEC coefficient are given in units of $10^{-10} \text{ G cm}^2 \text{ V}^{-1}$.

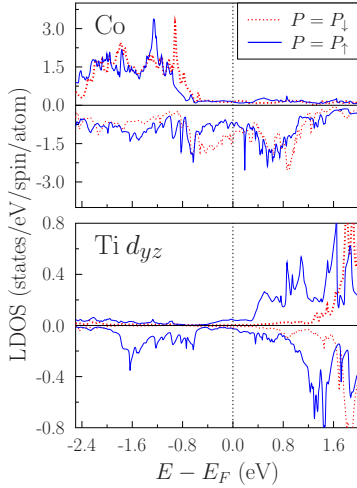


Figure 5.24: Spin-polarized density of states projected onto the Co cations (upper panel) and d_{yz} orbitals of Ti (lower panel) near the Co/PTO interface for the P_{\downarrow} and P_{\uparrow} polarization states (red dashed and blue solid curves, respectively).

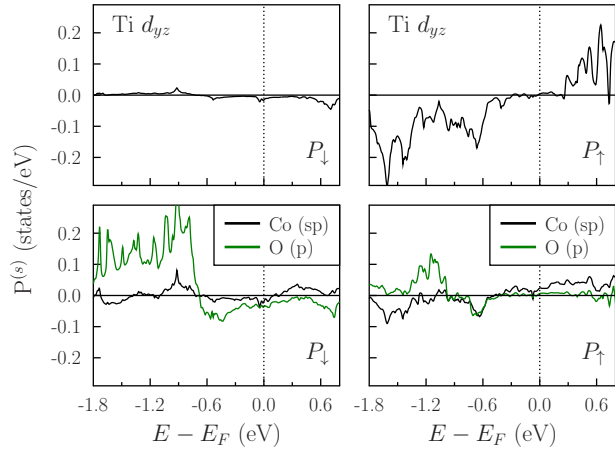


Figure 5.25: Energy-dependent spin imbalance of the hybridized sp electronic states of cobalt and p states of oxygen in the Co-O bonds and the d_{yz} states of the interface Ti cations for the P_{\downarrow} - and P_{\uparrow} -states of the Co/PTO (001) undoped interface.

effect of spin polarization in the ligand p states weakens considerably, which lets the Ti d_{yz} states prevail, as discussed above.

To summarize this part, the tunneling in the P_{\uparrow} -state occurs mostly due to hybridized Co-Ti bonds with a negative spin polarization leading to the inverse TMR. For the P_{\downarrow} -state, the tunneling is likely due to covalent Co-O bonds with a positive spin polarization of the ligand p states, which would explain the observation of the normal TMR effect. Our explanation of the polarization-dependent TMR ratio in LSMO/PZT/Co junctions is similar to that proposed by De Teresa et al. [177] also in relation to possibly voltage-dependent character of this effect.

As a conclusion, the present *ab initio* study clarifies the influence of Zr- and Hf-doping on the structural features and the magnetoelectric coupling at the multiferroic interface Co/Pb B_x Ti $_{1-x}$ O $_3$ (001) (B =Ti, Zr, Hf). Independent of the concrete interface composition, the MEC effect originates in the spin-dependent charge transfer from the metallic side into the d orbitals of the interfacial B transition metal cations, similarly to the previously studied Fe/BaTiO $_3$ and Fe/PbTiO $_3$ systems [60, 61]. The change of the interfacial magnetization in response to the polarization reversal was estimated to be of the order of 0.6–0.8 μ_B . The Zr/Hf-doping was found to affect the Co-O and Co-Ti bonding distances and to enhance locally the ferroelectric polarization. The highest interface roughness has been found for the Co/PZT system with energetically less preferable P_{\uparrow} -state. Our simulations of the 25%-doped interface demonstrated the tendency of the cobalt layers to reconstruct in such a way to approach the original bulk structure, which is totally different from the perfect epitaxially grown *fcc* structure. Formation of a nicely shaped *hcp*-like element in the structure of the cobalt film is observed for all studied interfaces. The MEC effect averaged in the in-plane direction appears to be robust with respect to weakly magnetic Zr and Hf impurities. The newly considered system Co/PHT (001) with the 5d transition metal cations of Hf should have a comparable application potential as the more widely discussed Co/PZT interface. In view of the recent experimental findings concerning LSMO/PZT/Co tunnel junctions [11] and similar LSMO/PZT heterostructures [178, 179], I also discussed here

the relation of the magnetoelectric coupling effect to the spin polarization of tunneling electrons and the observed change of the sign of the TMR effect induced by the polarization reversal.

5.3 Magnetization modulation in LSMO/PTO

The *ab initio* results for the Co/PZT interface presented above indicate that the anticipated magnetoelectric coupling in this system might account for the observed transport properties of the LSMO/PZT/Co tunnel junction. On the other hand, the contribution of the complex LSMO/PZT interface to the observed tunneling phenomena needs to be clarified as well. In the original paper [11], it was suggested that the other interface between La(Sr)MnO₃ (LSMO) and PZT plays only a minor role in the inversion of the TMR effect. Recent findings [178, 179] support this hypothesis for the chosen composition $x=0.33$ of LSMO, which proves to be magnetically robust. However, the data on the microscopic phenomena at this multiferroic LSMO/PZT interface presented in the literature lack completeness, especially in relation to transport phenomena in the corresponding tunnel junctions [150, 179, 180].

In this part of my work, I will present first-principle results on the electronic and magnetic properties of the [001]-oriented LSMO/PTO interface with two chemically different terminations. Special focus is put on the effect of the ferroelectric polarization on the electronic behaviour near the interface which gives rise to a particularly strong direct magnetoelectric coupling. As it would become clear, the mechanism of this coupling phenomenon is in part different from what was suggested previously for Fe/BaTiO₃ [60] and similar systems [10].

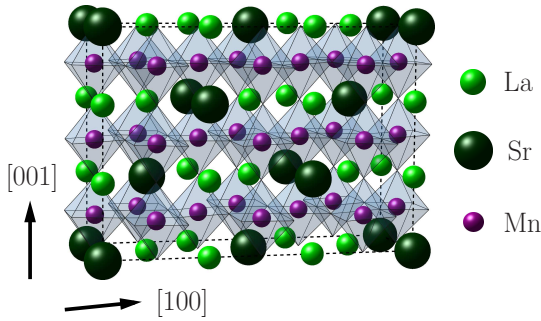


Figure 5.26: Supercell of the bulk $\text{La}_{1-x}\text{Sr}_x\text{MnO}_3$ for $x = 1/3$ and the La-Sr distribution with the lowest total energy. Oxygen octahedra are shown around each Mn cation.

At the first step, bulk LSMO material was simulated using a rhombohedral cell with 6 formula units and 2 Sr cations replacing La cations on different positions. All possible Sr distributions were studied and compared with each other with respect to the total electronic energy. Then, the Sr configuration with the lowest energy was transformed into a $(2 \times 3 \times 3)$ -supercell (Fig. 5.26) with the tetragonal lattice symmetry in order to accommodate the epitaxial growth conditions on the PTO substrate. The structure was fully optimized to obtain the equilibrium volume and bond lengths using the same electronic structure method as for the Co/PZT system (see paragraph 5.2) with the Γ -centered $6 \times 2 \times 3$ k-point Monkhorst-Pack [164] mesh and the conjugate-gradient algorithm until the Hellmann-Feynman forces became less than $10^{-2} \text{ eV}/\text{\AA}$. The cutoff energy for the plane-wave representation of the electronic wave functions was chosen to be 400 eV. The density of states (DOS) was calculated using the tetrahedron method on the same \mathbf{k} -mesh with no smearing for the electronic occupations. To take into account the effect of electronic correlations, the Dudarev approach to the GGA+ U parametrization [96] was applied on the $3d$ orbitals of all Mn cations, with the values of the U parameter ranging between $U=0$ eV and 2 eV.

From the GGA calculations, the equilibrium volume $V_{\text{eq}} = 59.41 \text{ \AA}^3/\text{f.u.}$ is 2% larger than the experimental value $V_{\text{eq}} = 58.23 \text{ \AA}^3/\text{f.u.}$ [181]. The chosen arrangement of La and Sr cations in different atomic planes shown in Fig. 5.26 provides a relatively uniform distribution of the Sr dopant. However, in the chosen supercell two types of magnetic

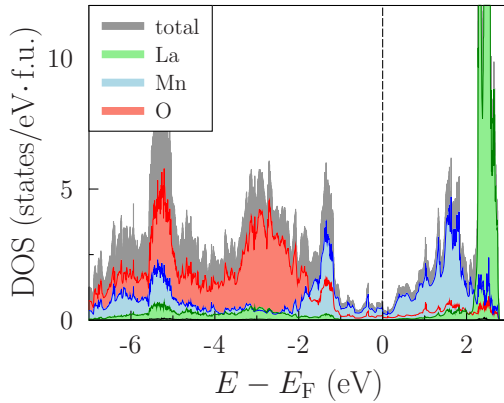


Figure 5.27: Total density of states of the bulk LSMO (grey-shaded area) and different atomic contributions (DOS of Sr is marginal and is not shown here). In each case, the sum over both spin channels is presented.

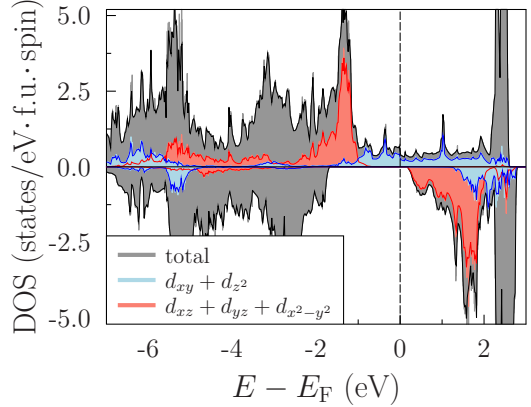


Figure 5.28: Spin-resolved total density of states of the bulk LSMO (grey-shaded area). Site-projected contributions to the DOS from the Mn d states with different symmetry are presented separately in each spin channel.

Mn cations can be found that differ by the number of the nearest Sr cations. The type-I Mn sites have 2 Sr neighbors, whereas the type-II Mn sites have 3 Sr neighbors. In the chosen model, the average value of the Mn magnetic moments equals $m = 3.3\mu_B$ and its variation in the supercell is of the order of $\Delta m = 0.05\mu_B$. Oxygen ions and La cations contribute moderately to the total magnetization ($m(O) = 5 \cdot 10^{-2}\mu_B$, $m(La) = 6 \cdot 10^{-2}\mu_B$), whereas the Sr sites show almost no magnetism.

The electronic states near the Fermi energy are formed mostly by the d orbitals of Mn cations (Fig. 5.27). In particular, Mn orbitals with the d_{xy} and d_{z^2} symmetry give the largest contribution in the spin-up channel, whereas the spin-down channel constitutes the orbitals with d_{xz}/d_{yz} and $d_{x^2-y^2}$ symmetry (Fig. 5.28). The occupied states below $E - E_F < -2$ eV are mostly due to the hybridized Mn d and oxygen p states. The f states of La lie in the higher energy range, approximately 2 eV above the Fermi level (Fig. 5.27). For the studied structure, a moderate half-metallic band gap is obtained in the spin-down channel. Its value appears to be sensitive to electronic correlations and increases from 1.84 eV for $U=0$ eV to 2.50 eV for $U=0$ eV (Fig. 5.29). The correlations also shift the main peaks that correspond to the Mn d states and, in addition, pushes the La f states towards higher energies.

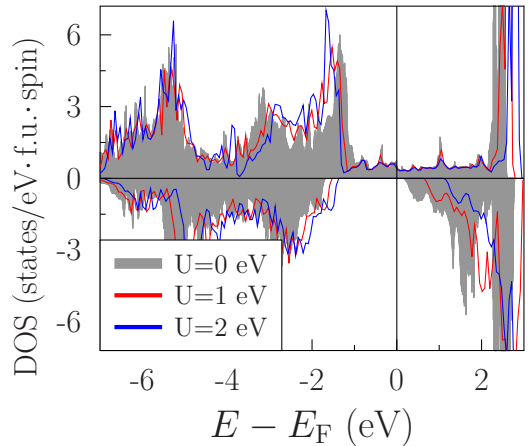


Figure 5.29: Spin-resolved total density of states of the bulk LSMO within the GGA+U approach for different values of U parameter: 0, 1 and 2 eV.

To simulate the interface between LSMO and PTO, supercells with (2×3) geometry in the xy -plane were used (Fig. 5.30). This structure simulates the epitaxial growth of the originally rhombohedral and 33% Sr-doped LSMO on the tetragonal PTO substrate. First, the $(2 \times 3 \times 3)$ supercell that was used for the simulation of bulk LSMO (see Fig. 5.26) has been attached to 5 unit cells (u.c.) of PTO stacked along $[001]$ direction. A vacuum layer of more than 13 Å was added to avoid any

spurious interactions between the periodic images of the system. Further on, different interface terminations will be considered. In experiment [11], the epitaxial growth of LSMO/PZT/Co tunnel junctions was realized on the SrTiO₃ (001) (STO) substrate. Since the in-plane lattice parameters of STO (3.898 Å) and PTO (3.892 Å) are very close to each other, the in-plane dimensions of all supercells were fixed using $a=3.892$ Å and keeping $c/a = 1.071$ [18] within the “bulk” part of the ferroelectric side before relaxation. In all calculations, the optimized Pb-O and Ti-O displacements in bulk PTO equal 0.45 Å and 0.33 Å, respectively, which is in reasonable agreement with experiment [18]. The 2 u.c. of LSMO and the 2 u.c. of PTO on both vacuum sides were fixed and the atomic positions at the interface were fully optimized using the Γ -centered $4 \times 2 \times 1$ k-point Monkhorst-Pack [164] mesh. For the density of states calculations, the denser Γ -centered $8 \times 4 \times 1$ k-point mesh was used, and other parameters were the same as in the case of the bulk LSMO (see above). To mimic the polarization reversal, two cases of polarization in PTO were computed and compared with each other: P_{\leftarrow} and P_{\rightarrow} where the cations and anions of each atomic layer were displaced along [001] in accordance with the polarization state. For more details on this procedure one may refer to [50, 51]. Additionally, the calculated properties were checked with respect to the initial distances between the two materials before relaxation, and, as a result, no sizeable differences were found within the accuracy of calculations.

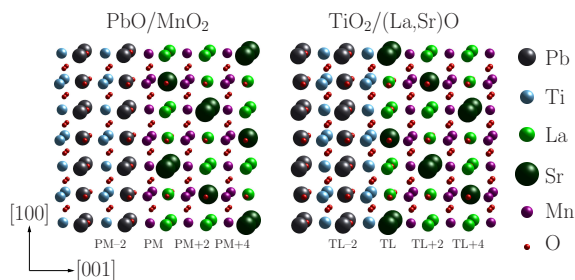


Figure 5.30: The supercells used to model the LSMO/PTO (001) interface with different terminations: PbO/MnO₂ (PM) and TiO₂/(La,Sr)O (TL). The first layer of LSMO at the interface is denoted by labels PM and TL according to the termination, and the other layers are labelled according to their relative position. The polarization of PTO is oriented along [001] direction.

polarization state P_{\leftarrow} , i.e. for \vec{P} pointing away from the LSMO film, the cation–oxygen displacements near the LSMO/PTO interface after relaxation showed a good stability for both interface termination (lower panels in Fig. 5.31). In contrast to it, the local displacements for the polarization state P_{\rightarrow} are considerably suppressed in the interface region (upper panels in the same figure). The observed features are again similar for both types of termination. The suppression of the ferroelectric displacements for one polarization was found previously for the Co/PZT interface as well [51]. Concerning the LSMO/PZT/Co multiferroic junction, this would mean that the ferroelectric displacements in the PZT barrier are non-homogeneous for both polarizations, with deviations occurring either on the Co or LSMO side.

From the structural relaxation data, one might conclude that the interface Mn-O bonds contract from 2.01 Å to 1.76 Å in response to the polarization reversal from P_{\rightarrow} to P_{\leftarrow} . This is expected to change drastically the orbital hybridization for the Mn d and oxygen p states, similar to the multiferroic Fe/BaTiO₃ interface [60]. The

In this section, I discuss the origins of the strong magnetoelectric effect anticipated for the LSMO/PTO heterostructure. The study begins with the structural analysis of the epitaxial LSMO/PTO system. For the chosen chemical compositions of the interface, the effect of the polarization reversal on the ferroelectric properties of the substrate, the interface bonding, as well as the tilting pattern in the magnetic oxide was investigated from first principles.

The intralayer ionic displacements in the PbO- and TiO₂-layers along [001] might characterize the local ferroelectric properties. It appears that, for the polar-

reversed behavior is observed for the Pb-O bonds, which become longer for the P_{\leftarrow} state. Additionally, the Ti-O bonds are subject to similar effect as the Pb-O bonds, so that the Ti-O bonds in the Ti-O-Mn atomic chains at the interface become either larger or smaller than the Mn-O bonds depending on which polarization state is established. As we shall see later on, the orbital hybridization effects in these Ti-O-Mn chains affect the electronic properties of the studied interface in the energy region close to the Fermi level, which is important for transport and magnetic phenomena.

In this part, we focus on two magnetic effects that are anticipated to be triggered at the LSMO/PTO oxide interface by the polarization reversal of the ferroelectric side.

The first effect is a modulation of the LSMO magnetization near the interface region as the polarization is switched to P_{\leftarrow} , which is seen from the layer-resolved magnetic moments in the heterostructure along the [001] direction (Fig. 5.32). The main contribution comes from the Mn 3d cations where the magnetization changes by almost $0.8 \mu_B$ in the first unit cell. There are small changes of the induced moments on Pb and O atomic sites as well in response to the stretching/contraction of the corresponding bonds. However, these effects are secondary to the modulation observed for the Mn sites. The magnetization change decays with the distance from the interface and is localized within 2 u.c. of LSMO. This phenomenon might be considered as an interfacial magnetoelectric coupling effect. The strength of this coupling, estimated from $\alpha = \Delta M / (E_c A)$, is comparable to the prototypic two-component multiferroic Fe/BaTiO₃ [60].

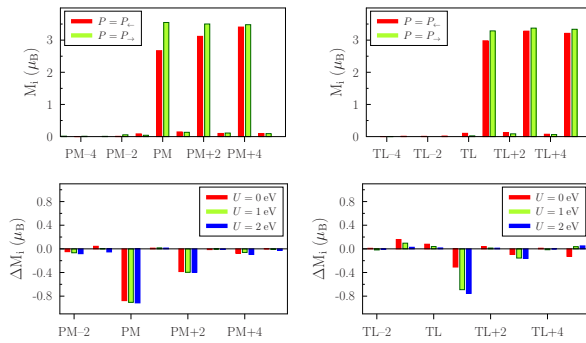


Figure 5.32: Layer-resolved magnetic moments (the upper two panels) for the two polarization states P_{\leftarrow} (red bars) and P_{\rightarrow} (green bars) together with the magnetization change $\Delta M_i = M_i(P_{\leftarrow}) - M_i(P_{\rightarrow})$ for each atomic plane (the lower two panels) in differently terminated LSMO/PTO (001) heterostructures. The magnetization difference ΔM_i is shown both for GGA (red bars) and for GGA+U approaches (green bars for $U=1$ eV and blue bars for $U=2$ eV).

moments on the Ti sites of the order of $0.04 \mu_B$. On the other hand, another interface where the TiO₂ plane is in contact with the first (La,Sr)O layer of LSMO is character-

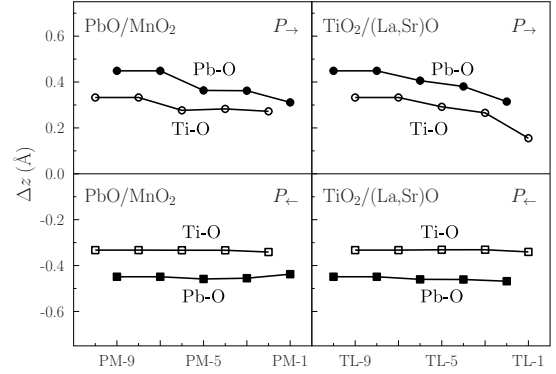


Figure 5.31: Relaxed ionic displacements Δz in PbO- and TiO₂-planes of the PTO substrate for the two polarization states P_{\leftarrow} and P_{\rightarrow} and two interface terminations.

The second effect is the induced magnetism in the PTO substrate which might be a “landmark” of the concrete interface termination. In particular, for the P_{\rightarrow} polarization, the Ti cations in the Ti-O-Mn atomic chains might become strongly ferromagnetically (antiferromagnetically) coupled to the neighboring Mn moments for the PM (TL) interface composition (see magnetization maps in Fig. 5.33). In the P_{\rightarrow} state, the Ti-O distance is much shorter than for the opposite polarization, which facilitates the orbital hybridization with the spin-polarized electronic states of LSMO. The PM interface, with the TiO₂ layer separated from LSMO by a PbO layer, shows positive magnetic moments on the Ti sites of the order of $0.04 \mu_B$. On the other hand, another interface where the TiO₂ plane is in contact with the first (La,Sr)O layer of LSMO is character-

ized by more pronounced and negative Ti moments of the order of $-0.1 \mu_B$ (Fig. 5.34). Within the GGA+U approximation, with corrections applied on all Mn cations in the system, the influence of electronic correlations in LSMO on the induced magnetism in PTO was investigated. In case of PM-terminated structure, the moment might become negative for both polarizations and $U > 1$ eV, whereas the sign change for the TL-terminated structure persists for all U up to 2 eV. It follows that different magnetic structures might be realized locally on the LSMO/PTO interface depending on its chemical composition. Therefore, by using an appropriate method for measuring the local magnetism on Ti sites, such as XMCD, one might be able to draw a conclusion on the interface termination of the epitaxially grown LSMO/PTO heterostructure, which is of great practical importance.

Each effect is a part of the observed magnetoelectric coupling at the studied multiferroic interface. Let us consider in more details different ionic contributions to this coupling.

First, due to the deformation of the Mn-O bonds the orbital overlap between the d states of Mn and p states of O is substantially changed. This affects the induced moments on the neighboring oxygen ions that are localized in the first unit cell near the interface. The ME coupling that originates in the polarization-dependent orbital hybridization has been extensively studied for similar multiferroic systems, such as (Fe,Co)/BTO and (Fe,Co)/PTO (for details, refer to [10, 60, 61]). Applying these ideas to our system, we see that, for the P_{\rightarrow} state, interfacial oxygens are relatively distant from the Mn cations and the induced moments are accordingly marginal. However, after the polarization reversal, the distance between the interacting ions is smaller and the charge transfer due to the Mn $d - O p$ orbital overlap is enhanced, so are the induced moments (lower panels in Fig. 5.33). The latter are always positive compared to those of Mn cations, which holds for both interface terminations. Additional significant contribution to the ME coupling comes from the interfacial Ti cations which, as mentioned before, might demonstrate different signs of the magnetic coupling with the neighboring Mn cations of LSMO.

The largest contribution to the interfacial ME coupling is related, however, to the spin-dependent screening of the polarization charges of PTO by the LSMO layers. Depending on the direction of the ferroelectric polarization, either positive or negative bound charges are generated on the PTO surface, which is in contact with the metallic LSMO film. The propagation of the related electric field into the metallic oxide is generally suppressed due to the formation of screening charges in LSMO over the length scale of the order of several nanometers. An important feature of the screening process in LSMO, in our case, is related to the fact that the density of states at the Fermi level, which mostly determines the effectiveness of screening, is formed solely by the spin-up electrons (Fig. 5.28 and 5.29). Therefore, the polarization charges in PTO would influence the spin-up electron density in the first few layers of LSMO, which manifests itself as a noticeable change of the Mn magnetic moments. This mechanism

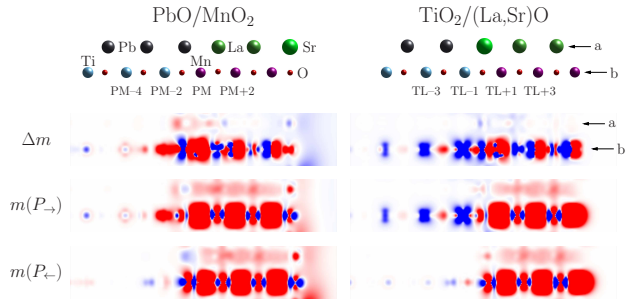


Figure 5.33: Spin-density distribution at the differently terminated LSMO/PTO (001) interface for the two polarization states P_{\leftarrow} and P_{\rightarrow} , as well as the redistribution of the spin density $\Delta m = m(P_{\rightarrow}) - m(P_{\leftarrow})$ under the ferroelectric switching. Aside the density maps, interface structures are presented to show the positions of different atomic species.

was studied recently [180] using first-principle methods and is assumed to account partially for the recent experimental findings on the metal-insulator transition and the accompanying magnetic response in the LSMO/BTO system [59]. However, due to the stronger polarization of PTO compared to BTO, this effect would be stronger for the considered LSMO/PTO multiferroic interface when temperature effects are taken into account.

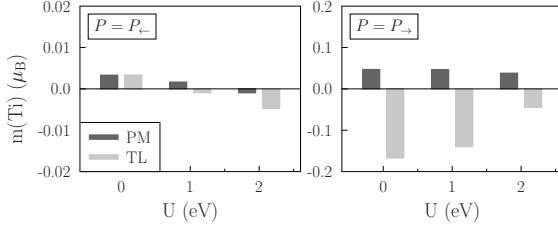


Figure 5.34: Induced magnetic moments on the interfacial Ti cations are presented vs the U parameter for the two polarization states P_{\leftarrow} and P_{\rightarrow} in differently terminated LSMO/PTO (001) heterostructures.

between the d states of Mn and the p states of the neighboring oxygen ions can be identified for both interfaces and the P_{\leftarrow} polarization (Fig. 5.35). This can be explained by the shortening of the interfacial Mn-O bonds due to the local geometry. The ferroelectric switching towards the P_{\rightarrow} state pushes the interfacial oxygen ions away from the neighboring Mn cations, thereby reducing the orbital overlap and suppressing any exchange processes between these atomic sites. This is one contribution to the aforementioned ME coupling effect.

Another contribution is related to the induced Ti moments. Opposite signs of the induced spin polarization on the interfacial Ti sites near the PM and TL terminated interfaces can be ascribed to the different atomic surroundings for the Mn and Ti cations in the interface region. On the one hand, the Ti-O and Mn-O distances do not differ much between the PM and TL structures. In both cases, the Ti-O bond becomes equally short for the P_{\rightarrow} polarization in comparison to the P_{\leftarrow} state. However, the La and Sr neighbors for the TL termination change the electronic states of the first Mn cations in a way that is different from the PM termination, where Pb cations from PTO replace the La and Sr cations. Although the hybridization of the Ti and Mn d states in the spin-down channel is strong for both types of the termination (see right panels in Fig. 5.35), the specific atomic neighborhood for the TL termination enhances the indirect interaction between the d orbitals of the aforementioned Mn and Ti cations.

The magnetization modulation, which is the largest contribution to the ME cou-

The suggested mechanism of the observed magnetoelectric coupling phenomenon finds its confirmation in the calculated electronic properties of the LSMO/PTO multiferroic system. Later on, I discuss these properties in relation to the interface chemical composition, bonding and hybridization effects, as well as band bending and electronic correlation effects.

From the site-projected density of states, strong orbital hybridization be-

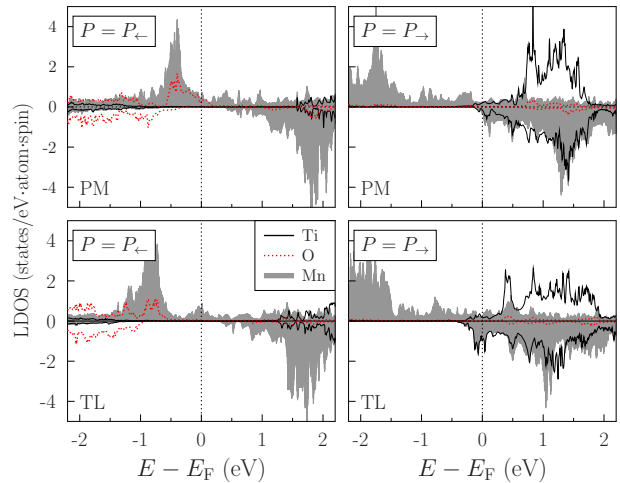


Figure 5.35: The site-projected densities of states of the interfacial cations in the Ti-O-Mn atomic chains are presented for the two polarization states P_{\leftarrow} and P_{\rightarrow} of differently terminated LSMO/PTO (001) heterostructures.

Although the hybridization of the Ti and Mn d states in the spin-down channel is strong for both types of the termination (see right panels in Fig. 5.35), the specific atomic neighborhood for the TL termination enhances the indirect interaction between the d orbitals of the aforementioned Mn and Ti cations.

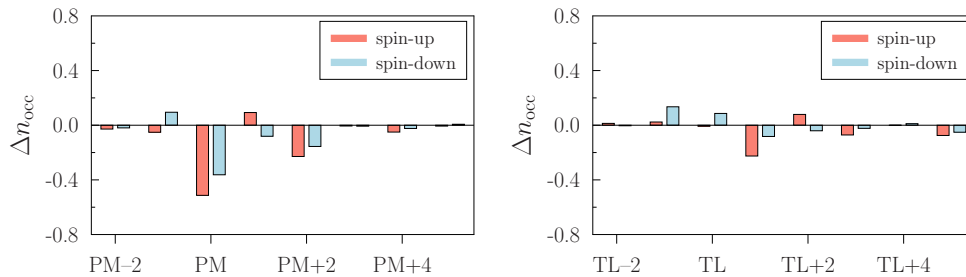


Figure 5.36: Layer-resolved change in the electronic occupations under the polarization reversal from the P_{\rightarrow} to the P_{\leftarrow} state near the LSMO/PTO (001) interface for different terminations.

pling at the LSMO/PTO interface, needs further analysis here. The main mechanism responsible for this magnetic effect is the electrostatic doping of LSMO by the ferroelectric PTO surface. In order to estimate the effect of the PTO electric field on the electronic states of the ferromagnetic LSMO film, the total change in the occupation numbers in response to the polarization reversal from the P_{\rightarrow} to the P_{\leftarrow} state was calculated for each oxide layer (Fig. 5.36). Similar to the results in Fig. 5.32, most changes are localized within 2–3 oxide unit cells, with the maximal value observed in the first MnO_2 layer. The spin-dependent character of this effect manifests itself as a pronounced difference in the spatial distributions of the majority and the minority charge carriers that are accumulated near the LSMO/PTO interface in response to the bound ferroelectric charges. Within the interface region, which consists of 1 PTO u.c. and 1 LSMO u.c., the PM terminated structure demonstrates a loss of 0.50 electrons in the spin-up channel and an injection of 0.37 electrons in the spin-down channel under the ferroelectric switching to the P_{\leftarrow} state. The TL interface shows qualitatively different features, since the occupations of the spin-up and the spin-down channels change by -0.20 and -0.14, respectively. In general, the effect of charge accumulation is anticipated to be stronger for the PM than for the TL interface. This can be understood also from the magnetization density in Fig. 5.33, where the ME coupling near the TL interface has two comparable contributions (from PTO and LSMO) of opposite signs that act against each other in the total sum.

As expected from basic electrostatics, charge accumulation in metallic LSMO is localized to the narrow region near the PTO substrate, since the electric field of PTO is effectively screened over a few atomic layers. The penetration of the electric field into LSMO can be estimated from the shift of the electronic states due to the local electrostatic potential. Calculations confirm that the ferroelectric switching from the P_{\rightarrow} to the P_{\leftarrow} state shifts the d states of the interfacial Mn cations towards higher energies (Fig. 5.37). This happens in both spin channels, so that, for the PM-terminated interface, the largest characteristic peak on the site-projected DOS is shifted by 1.3 eV in the majority channel and by 0.5 eV in the minority channel. Similar values are obtained for the TL-terminated structure where the shifts equal 1.1 eV and 0.6 eV in the spin-up and spin-down channels, respectively. The stronger influence of the PTO polarization on the spin-up states of the ferromagnetic LSMO is related to its half-metallicity and the large positive spin polarization at the Fermi level which is confirmed by the bulk calculations (Fig. 5.28 and 5.29). In the second MnO_2 layer, which is more distant from the interface, the energy shifts of the aforementioned peaks become smaller by the factor of 2 to 3. This indicates a strong suppression of the PTO electric field by the screening charges of the metallic LSMO. Finally, in the free surface layer, the effect of the energy shift becomes negligible and the ferroelectric switching

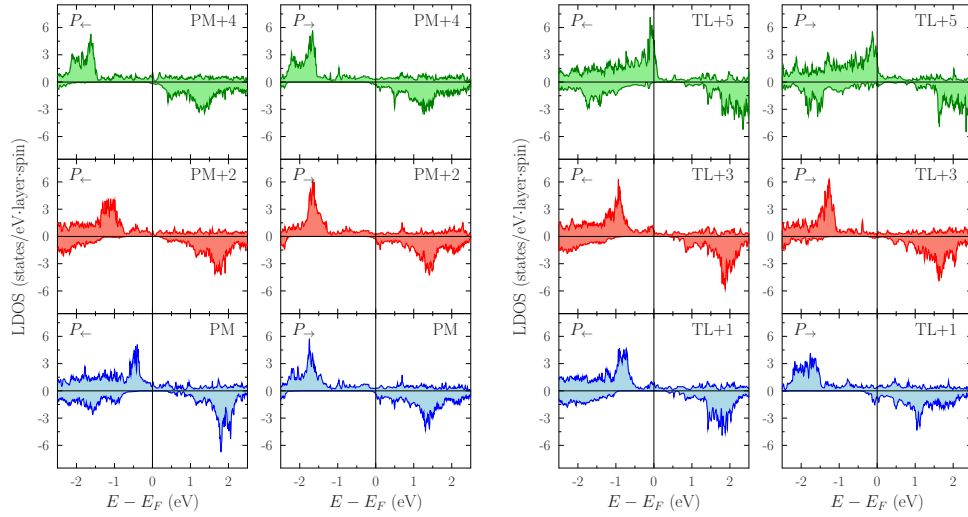


Figure 5.37: Site-projected spin-polarized density of states for the MnO_2 layers near the PM (left panels) and TL (right panels) terminated LSMO/PTO (001) heterostructures for the two polarization states of PTO (P_{\leftarrow} and P_{\rightarrow}).

has almost no influence on the electronic density of states.

To conclude this part, the multiferroic oxide interface between the ferromagnetic $\text{La}_{2/3}\text{Sr}_{1/3}\text{MnO}_3$ compound and the strongly ferroelectric PTO is studied using *ab initio* techniques. Magnetoelectric coupling for this heterostructure is anticipated to be localized within a few unit cells near the interface. Analysis of the calculated electronic and magnetic properties allowed to work out two main mechanisms that contribute to this effect. Firstly, the orbital hybridization in the Ti-O-Mn atomic chains changes in response to the polarization reversal in PTO which results in pronounced variations of the induced magnetic moments. Secondly, the spin-dependent screening effect of the PTO polarization by charge carriers in LSMO leads to a magnetization modulation that affects mostly the Mn sites, especially in the first LSMO layer. The effect is predicted to be stronger for the PbO/MnO_2 interface termination where the Mn cations are closer to the ferroelectric PTO surface. Analogous to the previously studied LSMO/BTO system [59], sizeable change of the FM Curie temperature of the epitaxial LSMO film is expected in the studied case under the influence of the ferroelectric polarization. This offers further research venues for this multiferroic system.

Another interesting feature that is worth a more detailed study is the spin polarization of the interfacial Ti sites which become magnetized under the influence of charge transfer from the LSMO side. The two studied interface terminations show the opposite sign of the Ti magnetic moments for the P_{\rightarrow} polarization state where the \vec{P} vector is oriented towards the LSMO film. This difference can be explained in view of the specific atomic environment which, in one case, includes Pb cations only and, in the other case, is composed both of La and of Sr cations. These findings offer a possibility of determining the realized interface termination by studying the local magnetic structure using, for example, XMCD characterization.

5.4 Spin-dependent transport in MFTJ

In the last part of this work, coherent electron tunneling transport in multiferroic metal/oxide heterostructures and its relation to the electronic effects and the magnetoelectric coupling at the interfaces are investigated.

For this purpose, a model system consisting of a PTO barrier sandwiched between two cobalt electrodes is chosen to study the polarization-controlled spin-dependent electronic transport. In the studied Co/PTO/Co tunnel junction, there are two chemically different interfaces (Co₂/PbO and TiO₂/Co₂) since PTO is assumed to grow in complete unit cells (u.c.), similarly to BTO [47, 48]. The thickness of the PTO barrier corresponds to 5 oxide u.c. At each side of the barrier, 5 atomic layers of cobalt as well as a vacuum layer of 20 Å were attached to separate both interfaces from each other in the self-consistent supercell calculation (Fig. 5.38). Initial ionic displacements in the barrier were fixed to the bulk values according to the polarization direction ($\Delta z > 0$ for P_{\rightarrow}). Using this supercell, the Zr-doped Co/PZT/Co junction was modelled within the digital alloy approximation where the Zr dopant is placed on the right interface in order to form a whole ZrO₂ layer. Then, atomic relaxation calculation where all atoms were allowed to move along the [001] direction of the supercell was performed using VASP [152–154] with the Γ -centered $4 \times 4 \times 2$ k-point Monkhorst-Pack [164] mesh. Afterwards, the vacuum layer was removed and additional optimization of all atomic positions in the supercell was performed.

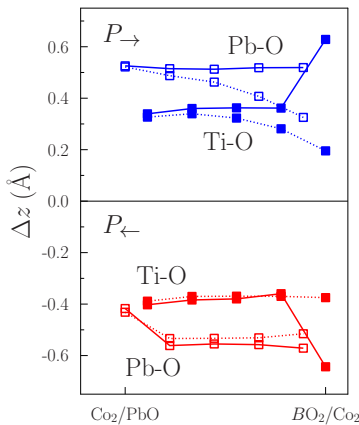


Figure 5.39: Relaxed ionic displacements Δz in the PbO and Ti(Zr)O₂ planes of the ferroelectric barrier in the Co/PTO/Co (dashed lines) and Co/PZT/Co (solid lines) tunnel junctions for the two opposite polarizations.

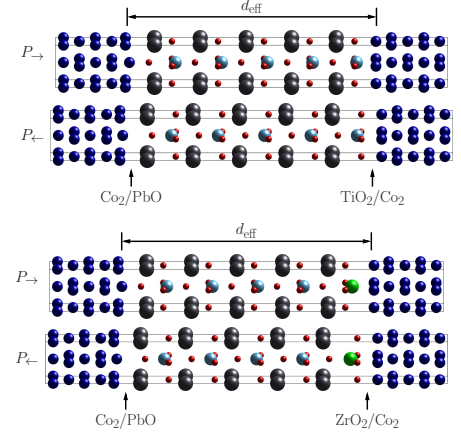


Figure 5.38: The supercells used to model the Co/PTO/Co and Zr-doped Co/PZT/Co tunnel junctions for the two opposite polarizations (P_{\leftarrow} and P_{\rightarrow}). Chemically different interfaces are marked below each structure. The effective thickness d_{eff} of the barrier, i.e. the distance between the cobalt electrodes, is shown by the horizontal arrow.

To accommodate different magnetic configurations of the electrodes, a double cell was constructed from the relaxed structure by creating a mirror image of the whole supercell with respect to the (001) plane and attaching it to the original system. Additional Co monolayers were added to the regions where the structure and its image are to be joined together. In the resulting supercell (not presented here), the polarization vectors of the two ferroelectric barriers are oppositely oriented, which compensates the total dipole moment in the system. The density of states was calculated for the double cell on the $15 \times 15 \times 1$ k-point mesh using QUANTUM ESPRESSO [155]. Energy cutoff for the wavefunction and charge density representation equal 63 Ry and 504 Ry, respectively, which provides a decent convergence of the electronic properties. The smearing for the electronic occupations is fixed to 0.02 Ry.

After relaxation, the ionic displacements in the PbO

and TiO_2 planes of PTO (Fig. 5.39) are rather homogeneous along the growth direction of the heterostructure for the P_{\leftarrow} state. In contrast to it, the structure for the opposite polarization (P_{\rightarrow}) shows a considerable suppression of these displacements near the TiO_2/Co_2 -terminated interface, which indicates a lower stability of this ferroelectric state. However, in the Zr-doped system, the local displacements become stabilized across the barrier and are considerably enhanced in the digital ZrO_2 layer at the right interface, which demonstrates again the role of Zr doping discussed previously in this work for the isolated Co/PZT interface (compare Fig. 5.39 and Fig. 5.16).

Another important structural effect has to be discussed in terms of the effective thickness of the ferroelectric barrier. Being defined as the distance between the interfacial cobalt layers on each side of the barrier, this structural parameter changes under the polarization reversal by 1.1 \AA for PTO and 0.8 \AA for PZT, so that the barrier becomes thinner for the P_{\rightarrow} polarization. This effect has been recently confirmed by transport measurements for epitaxial LSMO/PZT/Co tunnel junctions (see the private communications of A. Quindeau). In the present work, the explanation of this phenomenon is based on the bonding mechanism at both interfaces. Whereas the Co-O and Ti(Zr)-Co bonds dominate at the BO_2/Co_2 -terminated side ($B=\text{Ti, Zr}$), the Pb-Co and Co-O chemical bonds determine the structure of the Co_2/PbO -terminated interface. In both cases, the ferroelectric switching leads to either contraction or stretching of these bonds, which, in turn, changes the effective thickness of the barrier. However, electronic contributions to this quantity are equally important and should be taken into account. This issue will be discussed further on in the text.

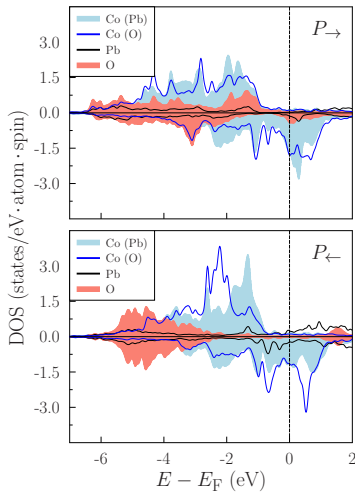


Figure 5.41: Spin-resolved density of states of the two in-plane cobalt atoms (on top of Pb and O ions), as well as oxygen and lead cations at the Co_2/PbO -terminated interface in the Co/PZT/Co tunnel junction for two opposite polarizations.

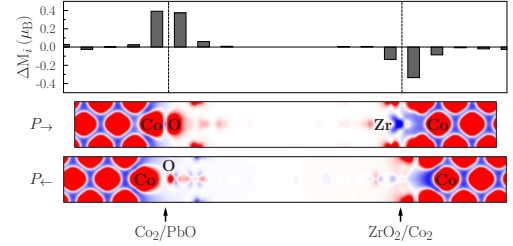


Figure 5.40: The spin-density distribution for the two opposite polarizations (P_{\leftarrow} and P_{\rightarrow}) and the layer-resolved change of the magnetization $\Delta M_i = M_i(P_{\rightarrow}) - M_i(P_{\leftarrow})$ in the Co/PZT/Co tunnel junction.

In the studied multiferroic junction, strong magnetoelectric coupling is anticipated for both interfaces. The spin-density distribution, plotted in Fig. 5.40 for one of the studied tunnel junctions, namely, Co/PZT/Co, shows the induced moments on the oxygen ions on the left side and zirconium cations on the right side in comparison with the strongly ferromagnetic cobalt leads. Similar behavior is observed also for the Co/PTO/Co junction, where even larger magnetic moments are induced on the Ti cations at the TiO_2/Co_2 interface. The latter is characterized by a strong magnetoelectric coupling that originates in the orbital hybridization effects on the Ti-Co and Co-O bonds [51]. A similar mechanism is anticipated for the Co_2/PbO -terminated interface in the studied multiferroic tunnel junction, however, in this case, the effect is attributed mostly to the Co-O bond. As the polarization is switched to the P_{\rightarrow} state, this Co-O bond is drastically shortened by more than 30% (from 2.65 \AA to 1.78 \AA). The Co-Pb bond, on the other hand, is moderately stretched from 2.51 \AA to 2.65 \AA . The combined effect of all these

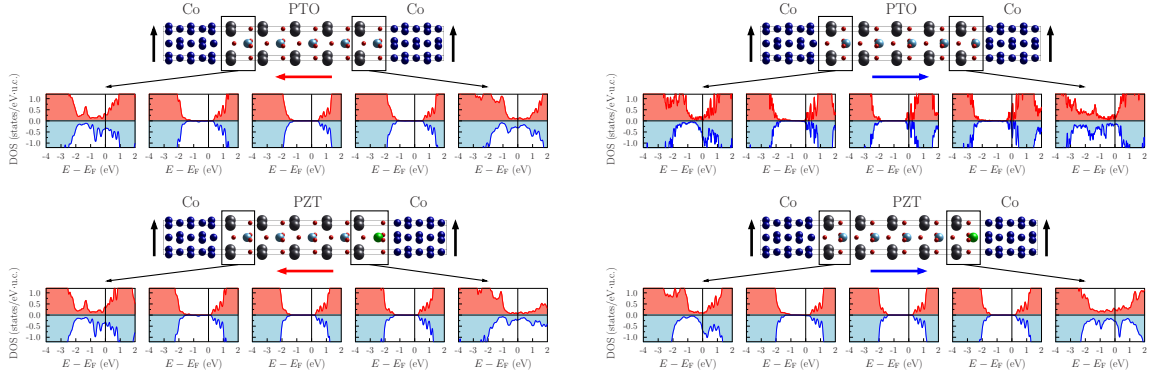


Figure 5.42: Spin-resolved density of states of the ferroelectric barrier in the Co/PTO/Co (upper panels) and Co/PZT/Co (lower panels) tunnel junctions for the two opposite polarizations (P_{\leftarrow} and P_{\rightarrow}). Subsequent unit cells of PTO (PZT) from one interface to another are presented. Magnetic configuration of electrodes is shown by the vertical arrows and the PZT polarization is shown, in each case, by a horizontal arrow.

structural changes is that the first cobalt layer near the PbO plane is not atomically flat and, accordingly, the magnetic moments of the two interfacial Co atoms are not equal. The cobalt atoms on top of the lead cations show a considerable decrease of the magnetization $\sim -0.3 \mu_B$ under the polarization reversal towards the P_{\leftarrow} state which is accompanied by a comparable increase for the Pb cations $\sim 0.2 \mu_B$. This effect is due to an increased overlap between the electronic states of these cations when the barrier polarization is P_{\leftarrow} -oriented. The magnetic moment of another cobalt site (on top of oxygen ions) is much more robust with respect to the ferroelectric switching. However, there is a strong O p -Co d hybridization in a broad energy range, as well as a sizeable delocalization on the oxygen sites observed for the P_{\rightarrow} -polarized barrier, which is also seen on the site-projected density of states (Fig. 5.41). The larger orbital overlap between the aforementioned states enhances the induced moments on the oxygen sites, which have the same sign of spin polarization as the neighboring cobalt atoms. Therefore, the magnetoelectric coupling at the considered interface has two contributions: firstly, the induced moments in the first PbO oxide layer and, secondly, the local change of cobalt magnetization. From the layer-resolved magnetization change in the Co/PZT/Co heterostructure (Fig. 5.40) it can be seen that the ME coupling effect is localized within a few atomic layers in the interface regions.

To summarize this part, the ME coupling effect is anticipated for both interfaces in the Co/PTO(PZT)/Co junction, which differ, however, by the sign of the magnetization change in response to the ferroelectric switching. The observed ME coupling has its origin in the polarization-dependent orbital hybridization for Co-O, Pb-Co and Ti(Zr)-O bonds, which might have a profound influence on the electronic transport in this system.

Before the transport calculations, static electronic properties of the ferroelectric barrier in the Co/PTO/Co and the corresponding Zr-doped system were studied to ensure the necessary conditions for the tunneling regime. For the P_{\leftarrow} polarization, the PTO barrier is locally metallic within 1 u.c. near the Co_2/PbO interface and in the top-most TiO_2 plane near the right interface, while the inner 3.5 u.c.-thick region remains insulating (see Fig. 5.42). The metallization effect is due to the spin-dependent charge transfer from the ferromagnetic cobalt into the ferroelectric side at both interfaces, which is the origin of a strong magnetoelectric coupling in this system. Under polarization reversal the charge transfer at the TiO_2/Co_2 -terminated side propagates much

further into the ferroelectric barrier, so that the whole PTO layer becomes metallic for the P_{\rightarrow} -polarized state. The metallization mostly affects the TiO_2 atomic planes, leaving the PbO layers insulating, except for the interfacial PbO plane near the left interface, where sizeable moments are induced on the oxygen sites. This would lead to a considerable enhancement of the electron current for this configuration, since additional contributions to the conductance not related to the tunneling mechanism would appear. Moreover, the alternating conducting TiO_2 and insulating PbO atomic planes might create new interesting possibilities for electron transport. In contrast to this, the Zr-doped tunnel junction does not reveal a “breakdown” of the tunneling regime. The ferroelectric PZT barrier remains insulating in the inner region under switching and the metallization effect is restricted only to 1 u.c. near each interface, similarly to the P_{\leftarrow} -polarized $\text{Co}/\text{PTO}/\text{Co}$ (see Fig. 5.42). The reason for this fundamental difference between the PTO- and PZT-based tunnel junctions might be related to the aforementioned fact that Zr impurities stabilize the ionic displacements across the whole ferroelectric barrier (Fig. 5.39). Weaker localization of the 4d Zr orbitals might also reduce the penetration length of electronic states from the cobalt side.

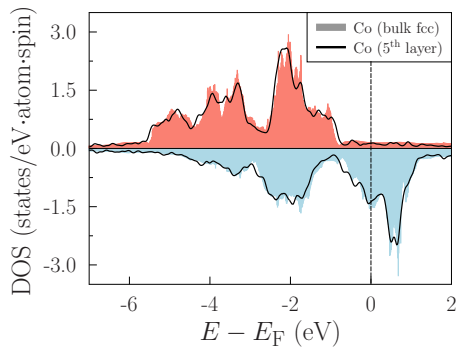


Figure 5.43: Comparison of the spin-resolved density of states of the bulk fcc cobalt and cobalt atoms in the fifth atomic layer away from the Co_2/PbO -terminated interface in the $\text{Co}/\text{PZT}/\text{Co}$ tunnel junction.

the electronic wavefunctions at these boundaries. Using the Landauer-Büttiker formalism implemented in QUANTUM ESPRESSO [124, 128, 155], the transmission function of $\text{Co}/\text{PTO}(\text{PZT})/\text{Co}$ was calculated in the two-dimensional Brillouin zone² for the different multiferroic states that can be realized in these tunnel junctions (see Fig. 4.7). An adaptive \mathbf{k} -mesh refinement procedure [182] was applied to obtain a reliable representation of the transmission function and an accurate estimate of the tunneling conductance (for details on the procedure see Appendix A). The latter was calculated for each configuration by integrating the transmission functions over the whole 2D Brillouin zone using the refined mesh. The convergence of the conductance up to $10^{-8} e^2/h$ (in the absolute value) is achieved already after a few refinements of the \mathbf{k} -mesh (see data in Appendix A). The average number of points needed for a reliable resolution of all features on each 2D map is in the range $N_{\text{kpts}} = (4 - 6) \cdot 10^3$.

For the $\text{Co}/\text{PTO}/\text{Co}$ tunnel junction, the tunneling transmission maps are presented in Fig. 5.44 for the P_{\leftarrow} polarization which leaves the barrier insulating. From the integrated values shown in Table III it can be concluded that the parallel orientation of the lead magnetization provides a higher tunneling conductance than the

²The BZ has a square form and is defined by inequalities $-\pi/a \leq k_x \leq \pi/a$ and $-\pi/a \leq k_y \leq \pi/a$.

antiparallel one, which corresponds to the normal TMR effect. For the parallel configuration of the electrodes, the tunneling transport is dominated by the spin-up electrons that demonstrate the free-electron character with the largest transmission values observed near the Gamma-point of the BZ. The spin-down channel also contributes to the transmission function, shows, however, a much more complex behavior with the largest transmission values observed near the \hat{X} and \hat{M} points of the BZ. The antiparallel configuration is characterized by reduced values of the tunneling conductance and a qualitatively different behavior of the transmission maps. In this case, the spin-up and spin-down channels contribute almost equally to the total conductance.

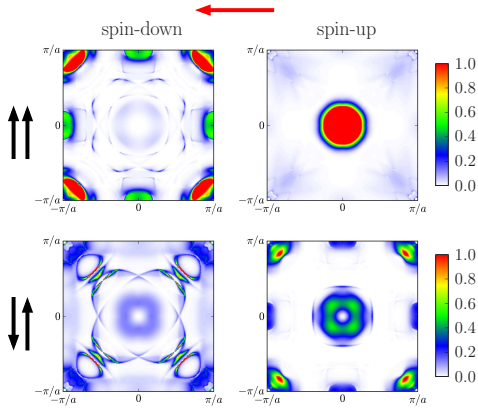


Figure 5.44: Spin-resolved transmission function of the multiferroic Co/PTO/Co tunnel junction for the P_{\leftarrow} polarization. Magnetic configuration of electrodes is shown by two vertical arrows on the left side of each panel, the barrier polarization is shown by the horizontal arrow. Transmission values are presented in units of $10^{-5} e^2/h$.

while keeping the qualitative behavior of this function unchanged. The Zr-doped system shows the normal TMR effect with the TMR ratio increased compared to the undoped system. After the polarization reversal, the qualitative behavior of the transmission maps becomes totally different from what was found for the opposite polarization. However, the sign of the TMR effect is preserved and its absolute value is moderately reduced from 70% to 48%.

All transmission maps presented in Fig. 5.44 and 5.45 show some of the characteristic features of the Fermi surface of the cobalt leads. The projection of this surface onto the 2D part of the BZ has an imprint on the spin-resolved transmission function (Fig. 5.49 in this paragraph and Fig. 5.54 in Appendix A) calculated for the tetragonally distorted *fcc* cobalt structure that is used as electrode material in the Co/PTO(PZT)/Co tunnel junction. Although the spin-down states dominate in bulk cobalt, the *ab initio* results for the P_{\leftarrow} state of the studied system indicate that these states cannot propagate effectively through the barrier compared to the spin-up states. On the other hand,

The effect of Zr doping on the electronic transport can be analyzed by comparing the transmission data for Co/PTO/Co (Fig. 5.44) and Co/PZT/Co digital alloy system (Fig. 5.45). For the P_{\leftarrow} -polarized barrier, the electron transmission for the parallel configuration is enhanced in the spin-up channel due to the Zr doping, whereas it remains mostly unaffected in the spin-down channel. This occurs despite the fact that the thickness of the ferroelectric barrier increases under the Zr doping, which would normally lead to lower transmission probabilities because of the exponential decay of the propagating states. No sizeable change of the total electron current is observed for the antiparallel lead magnetizations as well. Major effect of Zr impurities, in this case, is an intensity redistribution over the main peaks of the transmission function

Table III. Integrated tunneling conductance (in units of $10^{-6} G_0$, $G_0 = e^2/h$) for the minority and the majority spin channels and different magnetic configurations of the P_{\leftarrow} -polarized Co/PTO/Co. The TMR ratio is presented as well.

	P_{\leftarrow}		
spin	min.	maj.	total
$\uparrow\uparrow$	1.40	2.03	3.43
$\downarrow\uparrow$	0.82	0.80	1.62
TMR			53%

On the other hand,

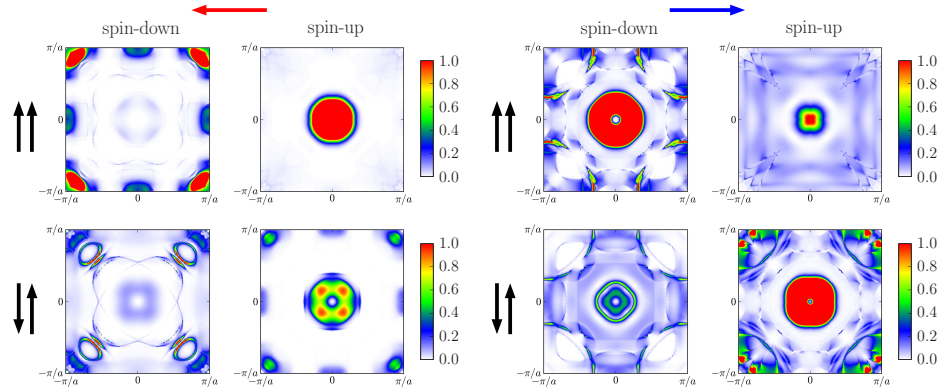


Figure 5.45: Spin-resolved transmission function of the Co/PZT/Co tunnel junction for the four multiferroic states. Magnetic configuration of electrodes is shown by two vertical arrows on the left side of each panel, the barrier polarization is shown, in each case, by a horizontal arrow. Transmission values are presented in units of $10^{-5} e^2/h$.

ferroelectric switching towards the P_{\rightarrow} state enhances the role of the spin-down channel (see Table IV). This can be explained by the polarization-triggered charge transfer at the Co/PZT interface where a large negative spin polarization appears on the Ti d orbitals due to the hybridization with the neighboring Co d orbitals [51].

Considering the TER effect in the Co/PZT/Co junction, where the barrier remains insulating under the polarization reversal, the conductance of the P_{\rightarrow} state is always higher than that of the P_{\leftarrow} state (see Table IV). The reason for this behavior might become clear, if one analyzes the local electrostatic potential $-e \cdot V(z)$ ($e > 0$) along the transport direction in this heterostructure³. Here, the potential is averaged for each z value and local minima and maxima of the resulting oscillating function vs the layer position are plotted in Fig. 5.46. While the potential is almost flat in the middle of the PZT barrier and in the distant cobalt layers, pronounced kinks appear on both interfaces of the considered junction. The magnitude of these kinks is related to the corresponding Schottky barriers. The potential step across the ZrO_2/Co_2 interface changes under the polarization reversal and becomes smaller for the P_{\rightarrow} state, which is in contrast to the behavior shown by another interface (Co_2/PbO) where no sizeable differences in the potential are observed. Moreover, the potential maxima and minima for the two polarization states are shifted along the $[001]$ direction with respect to each other. This might be interpreted as a smaller effective barrier thickness d_{eff} for the P_{\rightarrow} case and, since the influence of d_{eff} on the tunneling process has an exponential character, this enhances, in general, the conductance for the P_{\rightarrow} configuration.

To summarize this part, the presented results convince that the spin-dependent transport in the multiferroic Co/PTO/Co as well as Zr-doped Co/PZT/Co tunnel junction can be controlled by the polarization state of the ferroelectric barrier. This effect has different contributions: one is related to structural changes at the interfaces

Table IV. Integrated tunneling conductance (in units of $10^{-6} G_0$, $G_0 = e^2/h$) for the minority and the majority spin channels and different multiferroic configurations of Co/PZT/Co. The TMR and TER ratios are presented as well.

	P_{\leftarrow}		P_{\rightarrow}		TER
spin	min.	maj.	min.	maj.	
$\uparrow\uparrow$	1.43	3.55	16.2	0.79	241%
$\downarrow\uparrow$	0.70	0.82	0.80	8.07	484%
TMR	69.5%		47.8%		

³Further details on the procedure of obtaining this potential are given in paragraph 5.1.

under the switching of the electric polarization, and the other one originates from the strong interfacial magnetoelectric coupling that is attributed to the charge transfer from cobalt to the ferroelectric barrier. The former effect is responsible for a sizeable change of the effective barrier thickness in the switching process, which has a substantial influence on the tunneling conductance. The latter effect depends both on the symmetry of the hybridized orbitals that mediate the charge transfer and on the lengths of relevant bonds, such as Co-O and Co-Zr bonds at the ZrO_2/Co_2 terminated interface. Polarization-controlled orbital overlap at the interfaces and variable barrier thickness lead to the emergence of four distinct resistance states in the studied Co/PTO(PZT)/Co multiferroic system. A similar mechanism is anticipated for the more complex LSMO/PZT/Co tunnel junction, where the LSMO/PZT disordered interface might play, however, a significant role in electron tunneling, as follows from the *ab initio* results for this particular multiferroic interface discussed earlier in this work.

In the second part, spin-dependent electronic transport in conjunction with the magnetoelectric coupling phenomena are discussed for a more realistic system that represents the multiferroic LSMO/PTO/Co tunnel junction recently studied in [11].

The left electrode (LSMO) was modelled as a digital alloy by means of a $(1 \times 1 \times 3)$ supercell with three perovskite formula units and a tetragonally distorted structure where every third La cation is substituted by a Sr impurity. This structural model was applied by different authors to study the magnetism in bulk LSMO and related heterostructures [183, 184]. The equilibrium volume of the bulk phase was obtained within the GGA approach using the procedure based on the Murnaghan equation of state (3.46) (see paragraph 3.2.4) and equals $V_{\text{eq}} = 58.82 \text{ \AA}^3/\text{f.u.}$, which is 1.0% larger than the experimental value $V_{\text{eq}} = 58.23 \text{ \AA}^3/\text{f.u.}$ [181]. In comparison to this, the larger supercell that was described in paragraph 5.3 gives a worse agreement concerning the equilibrium volume.

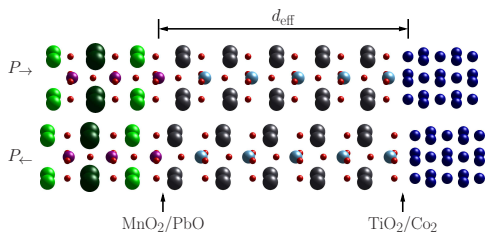


Figure 5.47: The supercells used to model the LSMO/PTO/Co tunnel junction for the two opposite polarizations (P_{\leftarrow} and P_{\rightarrow}). Chemically different interfaces are marked below by arrows. The effective thickness of the barrier (d_{eff}), i.e. the distance between the last MnO_2 atomic plane of LSMO and the last cobalt layer, is shown by the horizontal arrow.

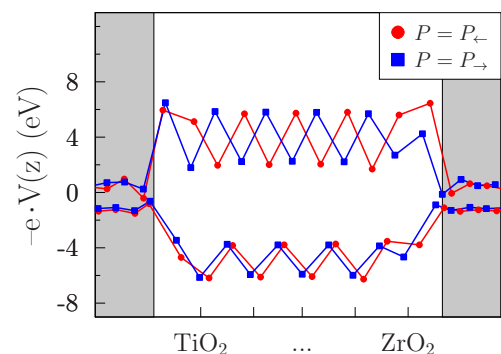


Figure 5.46: The electrostatic potential profile along [001] direction in the Co/PZT/Co tunnel junction for the two opposite polarizations (P_{\leftarrow} and P_{\rightarrow}). Local potential minima and maxima are plotted, each corresponding to an atomic plane. The electrode regions are shown by the grey-shaded areas.

Similarly to the case of the multiferroic Co/PTO(PZT)/Co tunnel junctions, a supercell for LSMO/PTO/Co is constructed using 5 u.c. of the ferroelectric PTO, 5 monolayers of cobalt and three LSMO u.c. (Fig. 5.47). The two interfaces in this tunnel junction have MnO_2/PbO and TiO_2/Co_2 terminations. The Sr-doped LSMO electrode is attached to the PTO film, so that the SrO layer is 1 u.c. away from the interface. A vacuum layer of more than 25 \AA was introduced to separate the free surfaces of the two ferromagnetic materials. The atomic relaxation was performed to obtain the equilibrium bonding distances at the

newly formed LSMO/PTO interface in the studied tunnel junction using VASP [152–154] with the Γ -centered $8 \times 8 \times 2$ k-point Monkhorst-Pack [164] mesh. The same procedure described above for the Co/PTO(PZT)/Co tunnel junctions was applied here to construct the corresponding double cells of LSMO/PTO/Co for the electronic structure and transport calculations. It should be noted that a double cell is necessary, in this case, even for the parallel magnetic configuration, since the studied tunnel junction has different electrodes that have to be isolated from each other in the supercell.

First, let us consider in more detail the electronic and magnetic properties of the LSMO electrode that is a part of the studied tunnel junction. From the spin-polarized density of states (Fig. 5.48) it can be concluded that LSMO is half-metallic with a positive spin polarization at the Fermi level. The DOS calculated for this Sr-doped digital alloy system compares well with the corresponding quantity that was obtained previously using a larger supercell with a different distribution of Sr impurities (see also Figs. 5.27-5.29 in paragraph 5.3). However, in the digital alloy model, the Mn magnetic moments show sizeable variations along the supercell that are of the order of $0.1 \mu_B$. This is explained by the existence of two distinct types of Mn cations in the digitally doped LSMO: one is situated between LaO and SrO planes, whereas the other has only LaO planes in its neighborhood. The latter Mn cations are characterized by a smaller magnetic moment ($3.40 \mu_B$) than the former ($3.48 \mu_B$). This is in contrast to the other structural model (Fig. 5.26) where the variations of the Mn magnetic moments are smeared out due to the more homogeneous distribution of Sr cations and do not exceed $10^{-2} \mu_B$. Despite this fact, the chosen approximation for the Sr-doped manganite appears to reproduce well its half-metallic conductive behavior at zero temperature and the existence of a moderate band gap ≈ 2 eV in the minority spin channel.

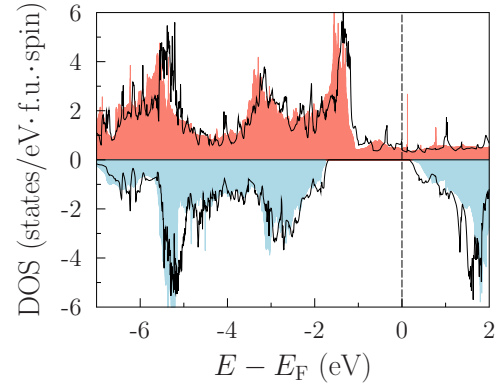


Figure 5.48: Spin-polarized density of states of the bulk LSMO in the ferromagnetic configuration. Results for the digital alloy model (shaded areas) are compared to those obtained using a larger supercell (solid lines).

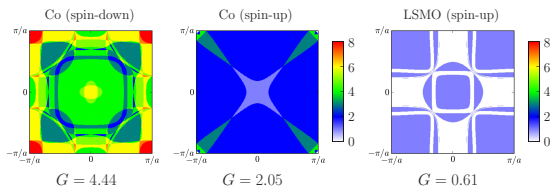


Figure 5.49: Spin-resolved transmission functions of the ferromagnetic cobalt (a) and LSMO (b) electrodes. Both spin channels are shown for cobalt, while only the spin-up current is present in LSMO. The total conductance values are given below each figure in units of $G_0 = e^2/h$.

or $T = 1$ transmission in the spin-up channel, whereas the minority states give no contribution to the electronic transport at the Fermi energy. More detailed analysis of the orbital symmetry shows that the electronic properties of cobalt at the Fermi energy are determined mostly by the majority s states and the minority d states. The Fermi surface of LSMO, on the other hand, is dominated by the d_{xy}/d_{z^2} states of Mn

The transmission functions of both electrodes are compared in Fig. 5.49 where the relative complexity of the electronic states in cobalt is opposed to the half-metallicity of LSMO. Multiple sheets of the Fermi surface in cobalt give rise to considerable variations of the transmission function that takes integer values from 0 to 8 within the 2D Brillouin zone, which corresponds to the number of available transmitting channels. In contrast to it, the LSMO electrode shows either zero

hybridized with the s and p orbitals of the surrounding oxygen. This fundamental difference between the two ferromagnetic materials is crucial for the understanding of tunneling phenomena in the multiferroic LSMO/PTO/Co oxide system.

The ferroelectric instability in the studied tunnel junction shows similar features compared to the Co/PTO/Co model system discussed previously in this chapter. For the P_{\leftarrow} polarization, the ionic displacements have a homogeneous distribution along the growth direction, whereas the opposite polarization is characterized by a strong suppression of the local ferroelectric distortions Δz near the TiO_2/Co_2 -terminated side (compare Fig. 5.39 and Fig. 5.50) and a moderate decrease of Δz near the other interface between LSMO and PTO. Structural changes in the ferroelectric PTO barrier and near both interfaces lead to the variation of the effective barrier thickness from 23.49 Å for the P_{\leftarrow} to 22.90 Å for the P_{\rightarrow} state. Detailed analysis of the interlayer distances in the optimized structure showed that this effect is dominated by the contraction of the atomic planes near the Co/PTO interface for the P_{\rightarrow} polarization. The estimated variation of the barrier thickness in LSMO/PTO/Co is smaller than in the model system with two cobalt electrodes and, therefore, even further away from the experimental result. However, the charge transfer phenomenon that is responsible for the ME coupling in this oxide system might change these estimates significantly.

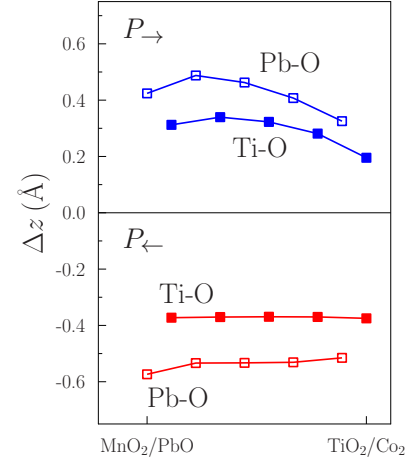


Figure 5.50: Relaxed ionic displacements Δz in the PbO and TiO_2 planes of the ferroelectric barrier in the LSMO/PTO/Co tunnel junction for the two opposite polarizations.

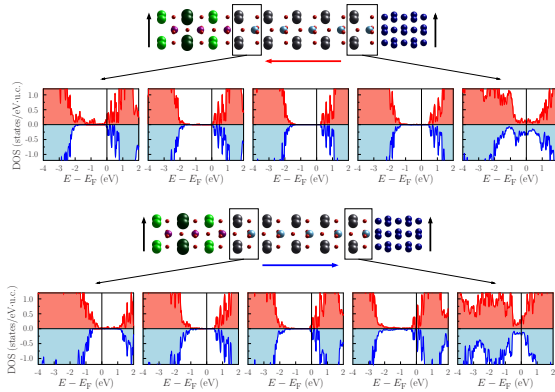


Figure 5.51: Spin-resolved density of states of the ferroelectric PTO barrier in the LSMO/PTO/Co tunnel junction for the two opposite polarizations (P_{\leftarrow} and P_{\rightarrow}). Subsequent unit cells of PTO from one interface to another are presented. Magnetic configuration of electrodes is shown by the vertical arrows and the PTO polarization is shown, in each case, by a horizontal arrow.

Similar metallization effect can be identified in the LSMO/PTO/Co tunnel junction. In the P_{\leftarrow} case, the three inner PTO u.c. are insulating, while the top-most u.c. near each electrode are metallic (Fig. 5.51). It should be mentioned that the PbO layers in the barrier are mostly insulating, so that the metallization effect is related to the charge redistribution in the TiO_2 atomic planes. The ferroelectric switching from the P_{\leftarrow} to the P_{\rightarrow} state enhances the metallization, as the charge transfer from the cobalt side propagates further into the barrier, affecting now two additional TiO_2 planes and making 2.5 PTO u.c. on the right side of the junction metallic. The second PTO u.c. near the MnO_2/PbO -

As noted already for the model Co/PTO/Co system, the ferroelectric polarization changes the electronic properties of the tunneling barrier, namely, the metallization effect is observed for the P_{\rightarrow} state where the spin-dependent charge transfer from cobalt towards the PTO film is significantly enhanced (Fig. 5.42). Due to the relatively small thickness of the PTO barrier, this phenomenon affects the whole barrier making it metallic.

terminated interface remains insulating, whereas the neighboring interfacial layer shows only marginal signs of metallization (Fig. 5.51). Therefore, the tunneling regime is preserved in the considered multiferroic system for both ferroelectric states, in contrast to the previously discussed Co/PTO/Co tunnel junction. On the other hand, the effective barrier thickness for the tunneling electrons would be smaller for the P_{\rightarrow} state due to the aforementioned metallization effect.

Strong magnetoelectric coupling is anticipated for both interfaces in the studied tunnel junction, as confirmed by the *ab initio* results for the isolated interfaces in paragraphs 5.2 and 5.3 of the present work. From the layer-resolved magnetization (Fig. 5.52) a sizeable change of $1 \mu_B$ can be seen in the topmost MnO_2 layer of LSMO near the PTO barrier under the polarization reversal. This is in agreement with the simulations using larger supercells with a different distribution of the Sr dopant (Fig. 5.32). According to the conclusions of paragraph 5.3, this effect originates from the spin-dependent screening of the bound polarization charges of PTO by the charge carriers in the half-metallic LSMO. The accumulation of additional carriers in LSMO in response to the ferroelectric polarization leads to the observed variations of the local magnetic moments. The effect decays exponentially as a function of the distance from the interface, and in the third LSMO unit cell the density of states is almost identical to that obtained for the bulk material (Fig. 5.48). Additional contributions to the ME coupling at this interface are due to orbital hybridization effects that are present also at the Co/PTO interface. The latter is characterized by negative induced moments on the Ti sites of the order of $-0.3 \mu_B$ for the P_{\rightarrow} polarization state and a comparable change of magnetization in the first atomic layer of cobalt. Away from the interface, the Co magnetic moments approach a constant value of $1.8 \mu_B$, which is close to the result of bulk calculations for the tetragonally distorted *fcc* structure.

The tunneling electronic current in the studied LSMO/PTO/Co system was calculated using the same method applied previously for the Co/PTO/Co and Co/PZT/Co tunnel junctions. In Fig. 5.53, the transmission maps for the four different multiferroic states are presented to demonstrate the main features of the TMR and TER effects in comparison with the model systems. The transmission function is non-zero only in the spin-up channel due to the half-metallic character of the LSMO electrode. The latter serves as a filter for the propagating states. Characteristic features of the Fermi surfaces of both electrodes can be identified on the obtained transmission maps by comparing them with the results presented in Fig. 5.49 for the LSMO and cobalt electrodes. The calculated conductance values for all studied configurations of LSMO/PTO/Co (see Table V) are smaller than most values obtained for the Co/PTO(PZT)/Co system. This is related to a smaller number of transverse modes in the half-metallic LSMO lead compared to the *fcc* cobalt. Similarly to the case of Co/PTO(PZT)/Co, normal TMR effect is observed for the LSMO/PTO/Co tunnel junction with the P_{\rightarrow} -polarized barrier, i.e. the parallel configuration of the lead magnetization is characterized by a larger conductance value than the antiparallel one. The estimated TMR ratio of 66% is comparable to the values obtained previously for the tunnel junctions with symmetric

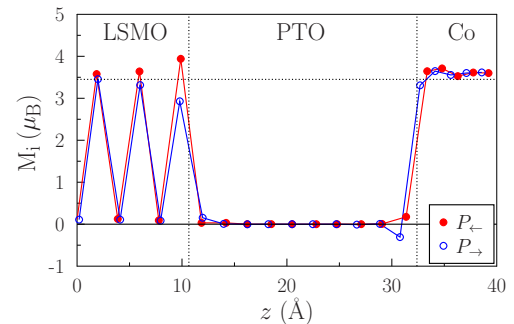


Figure 5.52: Layer-resolved magnetic moments in the multiferroic LSMO/PTO/Co tunnel junction for the parallel orientation of the lead magnetization and two opposite polarizations of the PTO barrier.

electrodes.

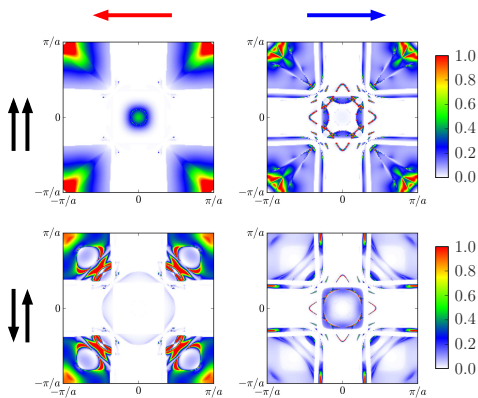


Figure 5.53: Spin-resolved transmission function of the LSMO/PTO/Co tunnel junction for the four multiferroic states. Magnetic configuration of electrodes is shown by two vertical arrows on the left side of each panel, the barrier polarization is shown, in each case, by a horizontal arrow. Transmission values are presented in units of $10^{-5} e^2/h$.

of the lead magnetization. The fact that these conditions are satisfied for the P_{\leftarrow} -polarized state but not for the opposite one can be attributed to the metallization effect in the PTO barrier and, therefore, suggests further research venues.

Therefore, the studied model system with asymmetric electrodes might reproduce the sign inversion of the TMR in the multiferroic LSMO/PZT/Co tunnel junction observed in experiment [11]. The estimated magnitude of the inverse TMR (-15%) agrees well with the low-temperature measurements of this quantity [11], whereas the calculated TMR ratio for the other polarization state (P_{\rightarrow}) is overestimated compared to the experiment. More importantly, these experimental data indicate that the polarization pointing towards Co electrode (P_{\rightarrow} for the supercell in Fig. 5.47) leads to the inverse TMR, whereas in the present *ab initio* study this is expected to happen for the opposite polarization, namely, for P_{\leftarrow} , as seen from the data in Table V.

Unusual behavior is revealed by the tunneling electroresistance that changes the sign under the magnetic switching of the electrodes. For the parallel configuration, the total tunneling current is enhanced for the P_{\rightarrow} state, giving thereby a moderate TER ratio of 26% , which is much smaller than the aforementioned values for the Co/PTO(PZT)/Co tunnel junctions. In contrast to it, the antiparallel configuration shows a significantly larger conductance for the P_{\leftarrow} polarization, so that the TER effect has a magnitude of 62% and a sign that is opposite to the experimental result (see Fig. 2 in [11]). The TER effect should be considered here in conjunction with the observed variations of the effective barrier thickness under the polarization reversal. From the atomic relaxation calculations, the effective thickness is expected to be smaller for the P_{\rightarrow} state by almost 0.6 \AA . Therefore, from this purely

Qualitatively different behavior is observed for the P_{\leftarrow} -polarized system. In this case, the antiparallel configuration has a larger total conductance than the parallel one, which is the signature of the inverse TMR effect. The origin of this behavior is related to the nature of tunneling states in the considered system. On the one hand, the electronic states in the left lead (LSMO) are positively spin-polarized at the Fermi level and have predominantly d character. On the other hand, the right lead (Co) provides both the majority s states and the minority d states. It follows that better matching conditions for the electronic wavefunctions on both sides of the junction and, consequently, a higher conductance can be achieved when electronic states with the same symmetry and spin are present in both leads, i.e. for the antiparallel orientation

Table V. Integrated tunneling conductance (in units of $10^{-6} G_0$, $G_0 = e^2/h$) for the majority spin channel and different multiferroic configurations of LSMO/PTO/Co. The TMR and TER ratios are presented as well.

	P_{\leftarrow}	P_{\rightarrow}	TER
$\uparrow\uparrow$	1.48	1.87	26%
$\downarrow\uparrow$	1.70	0.64	-62%
TMR	-15%	66%	

structural effect, one would expect a higher conductance for the P_{\rightarrow} ferroelectric state, which finds confirmation in the presented *ab initio* results for the parallel orientation of the lead magnetization (see Table V). The polarization-triggered charge transfer at the Co/PTO interface, which is the reason for the partial metallization of the PTO barrier (Fig. 5.51), provides an additional enhancement of the tunneling conductance. From this point of view, the origin of the unexpected TER behavior for the antiparallel configuration is not clear at the moment and requires a more detailed study.

To summarize, the spin-dependent transport properties of the multiferroic tunnel junctions with symmetric and asymmetric leads are studied in relation to the structural and magnetic changes that occur in these systems under the reversal of the ferroelectric polarization. For the Co/PTO(PZT)/Co tunnel junctions, normal TMR effect was obtained with a magnitude that depends on the polarization state of the barrier and varies in the range (50–70)%. In contrast to it, the LSMO/PTO/Co system with asymmetric leads reveals the sign inversion of the TMR induced by the ferroelectric switching, which clearly shows the importance of the half-metallic LSMO side for the transport phenomena. Concerning the TER in the studied system, the main factors determining this effect include i) the variation of the effective barrier thickness in the ferroelectric switching process, and ii) the local metallization of the barrier near the interfaces due to the charge transfer from the metallic leads. The latter effect is responsible for the strong ME coupling that allows to manipulate the magnetization locally by means of the ferroelectric polarization. The strongest magnetic response is observed for the LSMO/PTO interface where a magnetization change of up to $1.0 \mu_B/\text{surface u.c.}$ is anticipated, which exceeds the typical values reported for the prototype magnetoelectric Fe/BaTiO₃ interface [60, 61].

The aforementioned discrepancy between the experimental and first-principle results of this work regarding the TMR and TER effects indicates the necessity of further development of the *ab initio* model. In a search for a viable explanation of the TMR inversion in the LSMO/PZT/Co tunnel junction measured in [11] one might resort to different structural models where the influence of cation disorder at the interfaces is taken into account. Another important factor, which deserves a separate study, is the impact of electronic correlations on the tunneling phenomena. More specifically, the value of the fundamental band gap of the PTO (PZT) barrier is underestimated in the DFT-based calculations. Therefore, further studies using an appropriate correction scheme, such as the GGA+U approach [89, 96], might eventually answer the question, as to what conditions are necessary for the robust inversion of the TMR effect in such multiferroic systems.

Summary

In this work, electronic effects at multiferroic oxide interfaces, such as the magnetoelectric coupling and the emergence of a two-dimensional electron gas (2DEG), have been investigated using first-principle calculations. The presented studies were mostly motivated by recent experimental findings concerning the multiferroic and transport properties of LSMO/PZT/Co tunnel junctions [11] and many other oxide heterostructures [12, 59, 60] with interesting physics. Different *ab initio* techniques based on the density functional theory were applied to study the structural and electronic behavior of the systems of interest.

The emergence of a 2D electron gas was investigated on the example of the multiferroic SrTcO₃/BaTiO₃ (001) interface, which offers a new functionality due to the polarized nature of BaTiO₃ (BTO) and antiferromagnetic ordering in SrTcO₃, in contrast to the LaAlO₃/SrTiO₃ (001) system where this effect was first observed. The results of the present *ab initio* study suggest that the 2DEG appears in the SrTcO₃/BaTiO₃ system due to the accumulation of charge carriers near the interface in response to the electric field created by the polarized BTO side. The 2DEG character can be switched from the p-type to n-type by means of the polarization reversal. Moreover, the absence of polarization in BTO makes the electron gas disappear completely. This behavior is universal for both types of the interface termination and shows a weak dependence on the electronic correlations. The modest band gap of SrTcO₃ (less than 1.5 eV) and the tilting pattern of oxygen octahedra in this material are important factors for the formation of the 2DEG. The proposed mechanism might assist in identifying multiferroic structures with similar 2DEG behavior.

Further findings in the present work concern the magnetoelectric coupling phenomena and its influence on the electron tunneling in the LSMO/PZT/Co tunnel junctions. Both interfaces in this system show a strong ME coupling effect with a local magnetization change of the order of 1 μ_B . At the LSMO/PTO interface, the spin-dependent screening leads to a sizeable magnetization modulation in LSMO that provides the largest contribution to the ME response. Different magnetic structures might be induced in the ferroelectric PTO due to the charge transfer from the half-metallic LSMO depending on the concrete interface termination. This effect can be used in practice to identify the chemical composition of such interfaces. For the other interface between Co and PZT, strong orbital hybridization between the *d* states of Co and Ti(Zr) cations is responsible for the induction of a large negative spin polarization in a thin layer of the ferroelectric barrier. Moreover, reconstruction of the epitaxial cobalt film to an *hcp* structure is anticipated for both polarizations, independent of the Ti/Zr disorder in the PZT barrier.

In the final part, electronic tunneling effects are studied, first, for the model Co/PTO/Co and Co/PZT/Co systems, where, similarly to the experimentally investigated LSMO/PZT/Co junction [11], both interfaces are characterized by a strong magnetoelectric response. From the first-principle calculations of the tunneling conductance, four distinct resistance states have been clearly identified for this model tunnel junction. The tunneling magneto- and electroresistance ratios depend on the

conjugate order parameter, as expected for a multiferroic system. The presented results also support the experimental findings regarding the effective thickness of the PTO (PZT) barrier, which is an important input for the correct explanation of the observed TER effect. However, the sign of the TMR effect is always opposite to what is found in experiment [11]. This discrepancy shows that the ME coupling at the Co/PZT interface is insufficient to explain the inversion of the TMR effect and that the effect of the LSMO side should be included in the calculation of transport properties. Accordingly, a more realistic model system representing the multiferroic LSMO/PTO/Co tunnel junction was studied in comparison to the systems with two cobalt electrodes. Half-metallic nature and special symmetry of the electronic states in the ferromagnetic LSMO have a profound impact on the character of the tunneling states, which is argued to account for the inversion of both TMR and TER that were obtained for the considered system. However, the major discrepancy between theory and experiment, in this case, is the prediction of the concrete polarization direction for which the inverse TMR is observed. Further research venues are discussed in relation to the origins of the inversion of the TMR effect in the real system. In this respect, the spin-dependent charge transfer, which is responsible for the partial metallization of the ferroelectric barrier, is assumed to play the decisive role. The correct description of the insulating band gap of the barrier and the effects of structural imperfections at both interfaces might provide important insights and require further studies.

To summarize, the first-principle results of this work provide a detailed picture of the interplay between different order parameters and their influence on the electronic states at the multiferroic oxide interfaces. Different types of the magnetoelectric coupling in these systems have been investigated and their role for the tunneling phenomena was discussed.

Appendix A. Adaptive mesh refinement

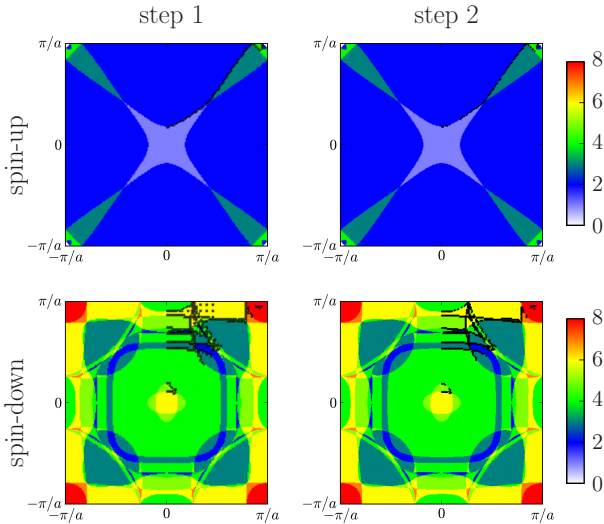


Figure 5.54: Refinement procedure for the transmission function of cobalt leads (upper panels for the spin-up and lower panels for the spin-down component). The regions of the irreducible BZ that need to be refined at each step are marked by the black color.

from the larger and the smaller elements are compared with each other and, depending on the relative difference between them, the mesh is further refined in the considered region. This process continues until the required precision for the total transmission is reached. The adaptive refinement method is advantageous for systems where the transmission function experiences abrupt changes, which might be related, in case of transition metals and oxides, to the localized d states.

The evolution of the \mathbf{k} -mesh is presented here for the fcc -cobalt electrodes (the last two steps are shown in Fig. 5.54). Due to the nature of the above-mentioned procedure, the refinement takes place exactly at the boundaries where the transmission function changes abruptly. In case of bulk cobalt, the transmission takes only integer values, so that the lines separating the regions with different values require a larger number of points, whereas inside these regions only a small number of points is necessary for a reliable representation of the transmission function.

On the example of the Co/PZT/Co multiferroic tunnel junction where the tunneling regime is realized, the convergence of the calculated total conductance with respect to the number of \mathbf{k} -points in the adaptive mesh refinement procedure can be demonstrated. For each multiferroic configuration, the calculation starts with a rough mesh containing 900 points in the irreducible part of the 2D Brillouin zone (step 1 in Fig. 5.55). The estimated value of the total transmission for this mesh (T_0) is taken as a first approximation for the subsequently refined values. At the next step, each

For the calculation of transmission maps, an adaptive mesh refinement technique [182] was used to reduce the number of \mathbf{k} -points that are necessary for a given precision. First, the irreducible part of the Brillouin Zone is subdivided into a moderate number of triangles, which is a starting configuration for the mesh. Then, each triangle can be further refined by finding its center of mass and connecting it with the corner points, thereby creating three new elements of the mesh. An alternative way that was also used in this work is to divide every edge of a given triangle in the middle, thereby obtaining four smaller triangles. In both approaches, the estimates of the integral transmission

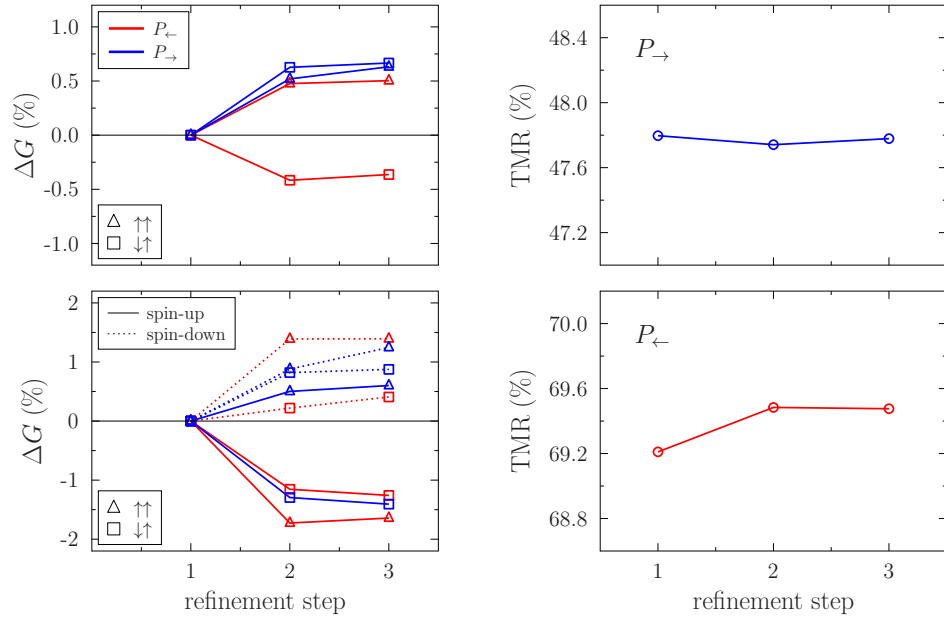


Figure 5.55: Relative change of the total tunneling conductance (left panels) and the TMR ratio (right panels) of the Co/PZT/Co tunnel junction after the subsequent adaptive \mathbf{k} -mesh refinement steps. In the left figures, the convergence of the tunneling conductance is demonstrated, first, for each spin channel (bottom figure) and, then, for the sum over the two spin channels (top figure) both for parallel and for antiparallel magnetic configurations. For each quantity, the results for the two opposite polarizations, P_{\leftarrow} (red lines) and P_{\rightarrow} (blue lines), are presented.

element of the mesh is refined by defining three smaller elements which yields 2628 mesh points in total (step 2 in Fig. 5.55). Further refinement of the mesh gives different numbers of additional \mathbf{k} -points within the range (600–3000) depending on the concrete configuration of the system. At each step, the relative deviation of the newly estimated total transmission T from the initial value T_0 is estimated (Fig. 5.55). The last refinement step (also presented in Table IV) changes the total value of T by less than 0.13%, whereas the corrections in each spin channel might be of the order of 0.4%.

Based on these data, the TMR ratio is calculated for each refinement step using the definition

$$\text{TMR} = \frac{G_{\uparrow\uparrow} - G_{\downarrow\uparrow}}{G_{\uparrow\uparrow}} \times 100\% \quad (5.2)$$

and the results are presented in Fig. 5.55. Reliable values are obtained even for the initial mesh, where the difference from the refined values is less than 0.5%.

Bibliography

- [1] **H. Schmid**, *Multi-ferroic magnetoelectrics*, *Ferroelectrics* **162** (1), pp. 317–338 (1994).
- [2] **N. A. Hill**, *Why are there so few magnetic ferroelectrics?*, *J. Phys. Chem. B* **104** (29), pp. 6694–6709 (2000).
- [3] **S. Picozzi** and **C. Ederer**, *First principles studies of multiferroic materials*, *J. Phys.: Condens. Matter* **21** (30), p. 303201 (2009).
- [4] **D. N. Astrov**, *The magnetoelectric effect in antiferromagnetics*, *Sov. Phys. JETP-USSR* **11** (3), pp. 708–709 (1960).
- [5] **D. Khomskii**, *Classifying multiferroics: Mechanisms and effects*, *Physics* **2** (20), pp. 1–8 (2009).
- [6] **N. A. Spaldin** and **M. Fiebig**, *The renaissance of magnetoelectric multiferroics*, *Science* **309** (5733), pp. 391–392 (2005).
- [7] **M. Fiebig**, *Revival of the magnetoelectric effect*, *J. Phys. D Appl. Phys.* **38** (8), pp. R123–R152 (2005).
- [8] **J. Hu**, **J. Li**, and **C.-W. Nan**, *Recent progress in multiferroic magnetoelectric composites: from bulk to thin films*, *Adv. Mater.* **23**, pp. 1062–1087 (2011).
- [9] **J. P. Velev**, **S. S. Jaswal**, and **E. Y. Tsymbal**, *Multi-ferroic and magnetoelectric materials and interfaces*, *Phil. Trans. R. Soc. A* **369**, pp. 3069–3097 (2011).
- [10] **J. D. Burton** and **E. Y. Tsymbal**, *Magnetoelectric interfaces and spin transport*, *Phil. Trans. R. Soc. A* **370**, pp. 4840–4855 (2012).
- [11] **D. Pantel**, **S. Goetze**, **D. Hesse**, and **M. Alexe**, *Reversible electrical switching of spin polarization in multiferroic tunnel junctions*, *Nat. Mater.* **11** (4), pp. 289–293 (2012).
- [12] **A. Ohtomo** and **H. Y. Hwang**, *A high-mobility electron gas at the $\text{LaAlO}_3/\text{SrTiO}_3$ heterointerface*, *Nature* **427**, pp. 423–426 (2004).
- [13] **J. B. Goodenough**, *Electronic and ionic transport properties and other physical aspects of perovskites*, *Rep. Prog. Phys.* **67** (11), pp. 1915–1913 (2004).
- [14] **M. Dawber**, **K. M. Rabe**, and **J. F. Scott**, *Physics of thin-film ferroelectric oxides*, *Rev. Mod. Phys.* **77** (4), pp. 1083–1130 (2005).
- [15] **D. J. Khomskii**, in *Spin Electronics*, edited by **M. Ziese** and **M. J. Thornton**, Springer-Verlag, Berlin Heidelberg (2001).

- [16] **T. Toshio, K.-H. Hellwege, H. Landolt, R. Börnstein, and O. Madelung**, *Ferro- and Antiferroelectric Substances*, vol. 3, Springer-Verlag, Berlin (1981).
- [17] **P. Bezdicka, A. Wattiaux, J. C. Grenier, M. Pouchard, and P. Hagenmuller**, *Preparation and characterization of fully stoichiometric SrCoO₃ by electrochemical oxidation*, *Z. anorg. allg. Chem.* **619** (1), pp. 7–12 (1993).
- [18] **H. H. Mestric, R.-A. Eichel, T. Kloss, K.-P. Dinse, S. Laubach, S. Laubach, P. C. Schmidt, K. A. Schonau, M. Knapp, and H. Ehrenberg**, *Iron-oxygen vacancy defect centers in PbTiO₃: Newman superposition model analysis and density functional calculations*, *Phys. Rev. B* **71**, p. 134109 (2005).
- [19] **N. A. Pertsev, A. K. Tagantsev, and N. Setter**, *Phase transitions and strain-induced ferroelectricity in SrTiO₃ epitaxial thin films*, *Phys. Rev. B* **61** (2), pp. R825–R829 (2000).
- [20] **R. D. Shannon and C. T. Prewitt**, *Effective ionic radii in oxides and fluorides*, *Acta Crystallogr. B* **25** (725) (1969).
- [21] **R. D. Shannon and C. T. Prewitt**, *Revised values of effective ionic radii*, *Acta Crystallogr. B* **26** (1046) (1970).
- [22] **W. Cochran**, *Crystal stability and the theory of ferroelectricity*, *Adv. Phys.* **9** (387) (1960).
- [23] **R. E. Cohen**, *Origin of ferroelectricity in perovskite oxides*, *Nature* **358**, pp. 136–138 (1992).
- [24] **R. E. Cohen**, *Theory of ferroelectrics: a vision for the next decade and beyond*, *J Phys. Chem. Solids* **61** (2), pp. 139–146 (2000).
- [25] **P. Ghosez and J. Junquera**, *First-Principles Modeling of Ferroelectric Oxides Nanostructures*, American Scientific Publisher (Stevenson Ranch, CA, USA) (2006).
- [26] **J. B. Goodenough**, *Magnetism and Chemical Bonds*, Interscience publ., N. Y.-Lnd (1963).
- [27] **T. Wolfram and S. Ellialtioglu**, *Electronic and Optical Properties of d-Band Perovskites*, Cambridge University Press, Cambridge (2006).
- [28] **H. A. Jahn and E. Teller**, *Stability of polyatomic molecules in degenerate electronic states. I. Orbital degeneracy*, *Proceedings of the Royal Society of London. Series A, Mathematical and Physical Sciences* **161** (905), pp. 220–235 (1937).
- [29] **J. B. Goodenough**, *Theory of the role of covalence in the perovskite-type manganites [La, M(II)]MnO₃*, *Phys. Rev.* **100** (2), pp. 564–573 (1955).
- [30] **E. Stoner**, *Atomic moments in ferromagnetic metals and alloys with non-ferromagnetic elements*, *Philosophical Magazine Series* **7** (15), pp. 1018–1034 (1933).

- [31] **M. Pouchard, A. Villesuzanne, and J.-P. Doumerc**, *Spin state behavior in some cobaltites (III) and (IV) with perovskite or related structure*, J. Solid State Chem. **162**, pp. 282–292 (2001).
- [32] **R. H. Potze, G. A. Sawatzky, and M. Abbate**, *Possibility for an intermediate-spin ground state in the charge-transfer material SrCoO₃*, Phys. Rev. B **51** (17), pp. 501–506 (1995).
- [33] **E. E. Rodriguez, F. Poineau, A. Llobet, B. J. Kennedy, M. Avdeev, G. J. Thorogood, M. L. Carter, R. Seshadri, D. J. Singh, and A. K. Cheetham**, *High temperature magnetic ordering in the 4d perovskite SrTcO₃*, Phys. Rev. Lett. **106**, p. 067201 (2011).
- [34] **M. Avdeev, G. J. Thorogood, M. L. Carter, B. J. Kennedy, J. Ting, D. J. Singh, and K. S. Wallwork**, *Antiferromagnetism in a technetium oxide. Structure of CaTcO₃*, J. Am. Chem. Soc. **133** (6), pp. 1654–1657 (2011).
- [35] **J. M. D. Coey, M. Viret, and S. von Molnár**, *Mixed-valence manganites*, Adv. Phys. **48** (2), pp. 167–293 (1999).
- [36] **C. Zener**, *Interaction between the d-shells in the transition metals. II. Ferromagnetic compounds of manganese with perovskite structure*, Phys. Rev. **82** (3), pp. 403–405 (1951).
- [37] **Y. Endoh, H. Nojiri, K. Kaneko, K. Hirota, T. Fukuda H, H. Kimura, Y. Murakami, S. Ishihara, S. Maekawa, S. Okamoto, and M. Motokawa**, *Field induced transition from metal to insulator in the colossal magnetoresistance manganites*, Mat. Sci. and Eng.: B **63** (1–2), pp. 151–158 (1999).
- [38] **H. D. Megaw**, *Origin of ferroelectricity in barium titanate and other perovskite-type crystals*, Acta Crystallogr. **5** (6), pp. 739–749 (1952).
- [39] **G. A. Smolensky, A. I. Agranovskaya, and V. A. Isupov**, SoV. Phys. Solid State **1** (149) (1959).
- [40] **W. Brixel, J. P. Rivera, A. Steiner, and H. Schmid**, *Magnetic-field induced magnetoelectric effects, (ME)_H, in the perovskites Pb₂CoWO₆ and Pb₂FeTaO₆*, Ferroelectrics **79** (1), pp. 495–498 (1988).
- [41] **C. Ederer and N. A. Spaldin**, *Weak ferromagnetism and magnetoelectric coupling in bismuth ferrite*, Phys. Rev. B **71** (6), p. 060401 (2005).
- [42] **J. Wang, J. B. Neaton, H. Zheng, V. Nagarajan, S. B. Ogale, B. Liu, D. Viehland, V. Vaithyanathan, D. G. Schlom, U. V. Waghmare, N. A. Spaldin, K. M. Rabe, M. Wuttig, and R. Ramesh**, *Epitaxial BiFeO₃ multiferroic thin film heterostructures*, Science **299** (5613), pp. 1719–1722 (2003).
- [43] **C. Ederer and N. A. Spaldin**, *Effect of epitaxial strain on the spontaneous polarization of thin film ferroelectrics*, Phys. Rev. Lett. **95** (25), p. 257601 (2005).
- [44] **S. M. Nakhmanson, K. M. Rabe, and D. Vanderbilt**, *Polarization enhancement in two- and three-component ferroelectric superlattices*, Appl. Phys. Lett. **87** (10) (2005).

- [45] J. H. Haeni, P. Irvin, W. Chang, R. Uecker, P. Reiche, Y. L. Li, S. Choudhury, W. Tian, M. E. Hawley, B. Craigo, A. K. Tagantsev, X. Q. Pan, S. K. Streiffer, L. Q. Chen, S. W. Kirchoefer, J. Levy, and D. G. Schlom, *Room-temperature ferroelectricity in strained SrTiO₃*, *Nature* **430** (7001), pp. 758–761 (2004).
- [46] M. Dawber, P. Chandra, P. B. Littlewood, and J. F. Scott, *Depolarization corrections to the coercive field in thin-film ferroelectrics*, *J. Phys.: Condens. Matter* **15** (24), pp. L393–L398 (2003).
- [47] H. L. Meyerheim, F. Klimenta, A. Ernst, K. Mohseni, S. Ostanin, M. Fechner, S. Parihar, I. V. Maznichenko, I. Mertig, and J. Kirschner, *Structural secrets of multiferroic interfaces*, *Phys. Rev. Lett.* **106**, p. 087203 (2011).
- [48] H. L. Meyerheim, A. Ernst, K. Mohseni, I. V. Maznichenko, J. Henk, S. Ostanin, N. Jedrecy, F. Klimenta, J. Zegenhagen, C. Schlueter, I. Mertig, and J. Kirschner, *Tuning the structure of ultrathin BaTiO₃ films on Me(001) (Me=Fe,Pd,Pt) surfaces*, *Phys. Rev. Lett.* **111**, p. 105501 (2013).
- [49] C. H. Lanier, J. M. Rondinelli, B. Deng, R. Kilaas, K. R. Poepelmeier, and L. D. Marks, *Surface reconstruction with a fractional hole: ($\sqrt{5} \times \sqrt{5}$)R26.6° LaAlO₃(001)*, *Phys. Rev. Lett.* **98** (8) (2007).
- [50] M. Fechner, S. Ostanin, and I. Mertig, *Effect of the surface polarization in polar perovskites studied from first principles*, *Phys. Rev. B* **77**, p. 094112 (2008).
- [51] V. S. Borisov, S. Ostanin, I. V. Maznichenko, A. Ernst, and I. Mertig, *Magnetoelectric properties of the Co/PbZr_xTi_{1-x}O₃ (001) interface studied from first principles*, *Phys. Rev. B* **89** (5) (2014).
- [52] L. Bengtsson, *Dipole correction for surface supercell calculations*, *Phys. Rev. B* **59** (19), pp. 12301–12304 (1999).
- [53] I. E. Dzyaloshinskii, *On the magneto-electrical effect in antiferromagnets*, *Sov. Phys. JETP* **10** (3), pp. 628–629 (1960).
- [54] S. Zhang, *Spin-dependent surface screening in ferromagnets and magnetic tunnel junctions*, *Phys. Rev. Lett.* **83**, pp. 640–643 (1999).
- [55] C.-G. Duan, J. P. Velev, R. F. Sabirianov, Z. Zhu, J. Chu, S. S. Jaswal, and E. Y. Tsymbal, *Surface magnetoelectric effect in ferromagnetic metal films*, *Phys. Rev. Lett.* **101**, p. 137201 (2008).
- [56] A. Sukhov, C. Jia, P. P. Horley, and J. Berakdar, *Polarization and magnetization dynamics of a field-driven multiferroic structure*, *J. Phys.: Condens. Matter* **22** (35) (2010).
- [57] P. P. Horley, A. Sukhov, C. Jia, E. Martinez, and J. Berakdar, *Influence of magnetoelectric coupling on electric field induced magnetization reversal in a composite unstrained multiferroic chain*, *Phys. Rev. B* **85** (5) (2012).

- [58] **J. D. Burton** and **E. Y. Tsymbal**, *Prediction of electrically induced magnetic reconstruction at the manganite/ferroelectric interface*, Phys. Rev. B **80**, p. 174406 (2009).
- [59] **H. Lu**, **T. A. George**, **Y. Wang**, **I. Ketsman**, **J. D. Burton**, **C. W. Bark**, **S. Ryu**, **D. J. Kim**, **J. Wang**, **C. Binek**, **P. A. Dowben**, **A. Sokolov**, **C. B. Eom**, **E. Y. Tsymbal**, and **A. Gruverman**, *Electric modulation of magnetization at the $BaTiO_3/La_{0.67}Sr_{0.33}MnO_3$ interfaces*, Appl. Phys. Lett. **100** (23), p. 232904 (2012).
- [60] **C.-G. Duan**, **S. S. Jaswal**, and **E. Y. Tsymbal**, *Predicted magnetoelectric effect in $Fe/BaTiO_3$ multilayers: Ferroelectric control of magnetism*, Phys. Rev. Lett. **97**, p. 047201 (2006).
- [61] **M. Fechner**, **I. V. Maznichenko**, **S. Ostanin**, **A. Ernst**, **J. Henk**, and **I. Mertig**, *Ab initio study of magnetoelectricity in composite multiferroics*, Phys. Status Solidi B **247** (7), pp. 1600–1607 (2010).
- [62] **J. P. Velev**, **C.-G. Duan**, **K. D. Belashchenko**, **S. S. Jaswal**, and **E. Y. Tsymbal**, *Effects of ferroelectricity and magnetism on electron and spin transport in $Fe/BaTiO_3/Fe$ multiferroic tunnel junctions*, J. Appl. Phys. **103** (7) (2008).
- [63] **S. Valencia**, **A. Crassous**, **L. Bocher**, **V. Garcia**, **X. Moya**, **R. O. Cherifi**, **C. Deranlot**, **K. Bouzehouane**, **S. Fusil**, **A. Zobelli**, **A. Gloter**, **N. D. Mathur**, **A. Gaupp**, **R. Abrudan**, **F. Radu**, **A. Barthelemy**, and **M. Bibes**, *Interface-induced room-temperature multiferroicity in $BaTiO_3$* , Nat. Mater. **10**, pp. 753–758 (2011).
- [64] **M. Fechner**, **S. Ostanin**, and **I. Mertig**, *Effect of oxidation of the ultrathin Fe electrode material on the strength of magnetoelectric coupling in composite multiferroics*, Phys. Rev. B **80**, p. 094405 (2009).
- [65] **M. Hölzer**, **M. Fechner**, **S. Ostanin**, and **I. Mertig**, *Effect of interfacial Cr on magnetoelectricity of $Fe_2/CrO_2/BaTiO_3$ (001)*, Phys. Rev. B **81**, p. 214428 (2010).
- [66] **M. Hölzer**, **M. Fechner**, **S. Ostanin**, and **I. Mertig**, *Ab initio study of magnetoelectricity in $Fe/BaTiO_3$: the effects of n -doped perovskite interfaces*, J. Phys.: Condens. Matter **23** (455902), pp. 1–6 (2011).
- [67] **N. Nakagawa**, **H. Y. Hwang**, and **D. A. Muller**, *Why some interfaces cannot be sharp*, Nat. Mater. **5**, pp. 204–209 (2006).
- [68] **R. Pentcheva** and **W. E. Pickett**, *Electronic phenomena at complex oxide interfaces: insights from first principles*, J. Phys.: Condens. Matter **22**, p. 043001 (2010).
- [69] **R. Pentcheva**, **R. Arras**, **K. Otte**, **V. G. Ruiz**, and **W. E. Pickett**, *Termination control of electronic phases in oxide thin films and interfaces: $LaAlO_3/SrTiO_3$ (001)*, Philos. T. Roy. Soc. A **370** (1977), pp. 4904–4926 (2012).

- [70] N. Reyren, S. Thiel, A. D. Caviglia, L. F. Kourkoutis, G. Hammerl, C. Richter, C. W. Schneider, T. Kopp, A.-S. Ruetschi, D. Jaccard, M. Gabay, D. A. Muller, J.-M. Triscone, and J. Mannhart, *Superconducting interfaces between insulating oxides*, Science **317** (5842), pp. 1196–1199 (2007).
- [71] N. Pavlenko, T. Kopp, E. Y. Tsymbal, J. Mannhart, and G. A. Sawatzky, *Oxygen vacancies at titanate interfaces: Two-dimensional magnetism and orbital reconstruction*, Phys. Rev. B **86**, p. 064431 (2012).
- [72] A. Brinkman, M. Huijben, M. Van Zalk, J. Huijben, U. Zeitler, J. C. Maan, W. G. Van der Wiel, G. Rijnders, D. H. A. Blank, and H. Hilgenkamp, *Magnetic effects at the interface between non-magnetic oxides*, Nat. Mater. **6** (7), pp. 493–496 (2007).
- [73] S. Thiel, G. Hammerl, A. Schmehl, C. W. Schneider, and J. Mannhart, *Tunable quasi-two-dimensional electron gases in oxide heterostructures*, Science **313**, pp. 1942–1945 (2006).
- [74] M. Bibes, N. Reyren, E. Lesne, J. M. George, C. Deranlot, S. Collin, A. Barthelemy, and H. Jaffres, *Towards electrical spin injection into $LaAlO_3 - SrTiO_3$* , Philos. T. Roy. Soc. A **370** (1977), pp. 4958–4971 (2012).
- [75] M. Huijben, G. Rijnders, D. Blank, S. Bals, S. Van Aert, J. Verbeeck, G. Van Tendeloo, A. Brinkman, and H. Hilgenkamp, *Electronically coupled complementary interfaces between perovskite band insulators*, Nat. Mater. **5** (7), pp. 556–560 (2006).
- [76] R. Arras, V. G. Ruiz, W. E. Pickett, and R. Pentcheva, *Tuning the two-dimensional electron gas at the $LaAlO_3/SrTiO_3$ (001) interface by metallic contacts*, Phys. Rev. B **85** (12), p. 125404 (2012).
- [77] P. Perna, D. Maccariello, M. Radovic, U. S. di Uccio, I. Pallecchi, M. Codda, D. Marre, C. Cantoni, J. Gazquez, M. Varela, S. J. Pennycook, and F. M. Granozio, *Conducting interfaces between band insulating oxides: the $LaGaO_3/SrTiO_3$ heterostructure*, Appl. Phys. Lett. **97** (15), p. 152111 (2010).
- [78] H. W. Jang, D. A. Felker, C. W. Bark, Y. Wang, M. K. Niranjan, C. T. Nelson, Y. Zhang, D. Su, C. M. Folkman, S. H. Baek, S. Lee, K. Janicka, Y. Zhu, X. Q. Pan, D. D. Fong, E. Y. Tsymbal, M. S. Rzchowski, and C. B. Eom, *Metallic and insulating oxide interfaces controlled by electronic correlations*, Science **331** (6019), pp. 886–889 (2011).
- [79] Y. Hotta, T. Susaki, and H. Y. Hwang, *Polar discontinuity doping of the $LaVO_3/SrTiO_3$ interface*, Phys. Rev. Lett. **99** (23), p. 236805 (2007).
- [80] M. Born and R. Oppenheimer, *On the quantum theory of molecules*, Ann. Phys. **84**, p. 457 (1927).
- [81] J. Kübler, *Theory of Itinerant Electron Magnetism*, Clarendon Press (2000).
- [82] W. Kohn, *Density Functional Theory: Fundamentals and Applications* (1985).

- [83] **J. P. Perdew** and **S. Kurth**, *Density functionals for non-relativistic coulomb systems in the new century*, in *A Primer in Density Functional Theory, Lecture Notes in Physics*, vol. 620, edited by **C. Fiolhais**, **F. Nogueira**, and **M. A. L. Marques**, pp. 1–55, Springer, Berlin (2003).
- [84] **D. Sholl** and **J. A. Steckel**, *Density Functional Theory: A Practical Introduction*, WILEY (2009), 252 pp.
- [85] **P. Hohenberg** and **W. Kohn**, *Inhomogeneous electron gas*, Phys. Rev. B **136** (3B), p. B864 (1964).
- [86] **W. Kohn** and **L. J. Sham**, *Self-consistent equations including exchange and correlation effects*, Phys. Rev. **140** (4A), pp. 1133–1138 (1965).
- [87] **U. V. Barth** and **L. Hedin**, *Local exchange-correlation potential for spin polarized case .1.*, J. Phys. C: Solid State Phys. **5** (13), pp. 1629–1642 (1972).
- [88] **A. K. Rajagopa** and **J. Callaway**, *Inhomogeneous electron-gas*, Phys. Rev. B **7** (5), pp. 1912–1919 (1973).
- [89] **V. I. Anisimov**, **J. Zaanen**, and **O. K. Andersen**, *Band theory and Mott insulators: Hubbard U instead of Stoner I* , Phys. Rev. B **44**, pp. 943–954 (1991).
- [90] **A. G. Petukhov**, **I. I. Mazin**, **L. Chioncel**, and **A. I. Lichtenstein**, *Correlated metals and the LDA+ U method*, Phys. Rev. B **67**, p. 153106 (2003).
- [91] **J. F. Janak**, **V. L. Moruzzi**, and **A. R. Williams**, *Ground-state thermomechanical properties of some cubic elements in local-density formalism*, Phys. Rev. B **12** (4), pp. 1257–1261 (1975).
- [92] **S. H. Vosko**, **L. Wilk**, and **M. Nusair**, *Accurate spin-dependent electron liquid correlation energies for local spin-density calculations – a critical analysis*, Can. J. Phys. **58** (8), pp. 1200–1211 (1980).
- [93] **J. P. Perdew** and **Y. Wang**, *Accurate and simple analytic representation of the electron-gas correlation-energy*, Phys. Rev. B **45** (23), pp. 13244–13249 (1992).
- [94] **J. P. Perdew**, **K. Burke**, and **M. Ernzerhof**, *Generalized gradient approximation made simple*, Phys. Rev. Lett. **77** (18), pp. 3865–3868 (1996).
- [95] **J. Heyd**, **G. E. Scuseria**, and **M. Ernzerhof**, *Hybrid functionals based on a screened Coulomb potential*, J. Chem. Phys. **118** (18), pp. 8207–8215 (2003).
- [96] **S. L. Dudarev**, **G. A. Botton**, **S. Y. Savrasov**, **C. J. Humphreys**, and **A. P. Sutton**, *Electron-energy-loss spectra and the structural stability of nickel oxide: An LSDA+ U study*, Phys. Rev. B **57** (3), pp. 1505–1509 (1998).
- [97] **J. P. Perdew** and **A. Zunger**, *Self-interaction correction to density-functional approximations for many-electron systems*, Phys. Rev. B **23** (10), pp. 5048–5079 (1981).
- [98] **J. P. Perdew**, **M. Ernzerhof**, and **K. Burke**, *Rationale for mixing exact exchange with density functional approximations*, J. Chem. Phys. **105** (22), pp. 9982–9985 (1996).

- [99] **K. Burke**, *Perspective on density functional theory*, J. Chem. Phys. **136** (150901), pp. 1–9 (2012).
- [100] **R. M. Martin**, *Electronic Structure: Basic Theory and Practical Methods*, Cambridge University Press (2008), 647 pp.
- [101] **D. J. Singh** and **L. Nordström**, *Planewaves, Pseudopotentials, and the LAPW Method*, Springer (2006), 147 pp.
- [102] **H. Ebert**, **D. Ködderitzsch**, and **J. Minár**, *Calculating condensed matter properties using the KKR-Green's function method - recent developments and applications*, Rep. Prog. Phys. **74** (9), p. 096501 (2011).
- [103] **J. C. Phillips** and **L. Kleinman**, *New method for calculating wave functions in crystals and molecules*, Phys. Rev. **116**, pp. 287–294 (1959).
- [104] **E. Antončík**, *Approximate formulation of the orthogonalized plane-wave method*, J. Phys. Chem. Solids **10** (4), pp. 314–320 (1959).
- [105] **M. H. Cohen** and **V. Heine**, *Cancellation of kinetic and potential energy in atoms, molecules, and solids*, Phys. Rev. **122** (6), pp. 1821–1826 (1961).
- [106] **L. Kleinman**, *Relativistic norm-conserving pseudopotential*, Phys. Rev. B **21** (6), pp. 2630–2631 (1980).
- [107] **D. Vanderbilt**, *Soft self-consistent pseudopotentials in a generalized eigenvalue formalism*, Phys. Rev. B **41** (11), pp. 7892–7895 (1990).
- [108] **P. E. Blöchl**, *Projector augmented-wave method*, Phys. Rev. B **50** (24), pp. 17953–17979 (1994).
- [109] **P. E. Blöchl**, **O. Jepsen**, and **O. K. Andersen**, *Improved tetrahedron method for Brillouin-zone integrations*, Phys. Rev. B **49** (23), pp. 223–233 (1994).
- [110] **F. O. Murnaghan**, *Finite deformations of an elastic solid*, Amer. J. Math. **59**, pp. 235–260 (1937).
- [111] **R. P. Feynman**, *Forces in molecules*, Phys. Rev. **56**, pp. 340–343 (1939).
- [112] **V. G. Tyuterev** and **N. Vast**, *Murnaghan's equation of state for the electronic ground state energy*, Computational Materials Science **38**, pp. 350–353 (2006).
- [113] **J. Korrynga**, *On the calculation of the energy of a bloch wave in a metal*, Physica **13** (6-7), pp. 392–400 (1947).
- [114] **W. Kohn** and **N. Rostoker**, *Solution of the Schrödinger equation in periodic lattices with an application to metallic lithium*, Phys. Rev. **94** (5), p. 1111 (1954).
- [115] **I. Mertig**, **E. Mrosan**, and **P. Ziesche**, *Multiple Scattering Theory of Point Defects in Metals: Electronic Properties*, Teubner, Berlin (1987).
- [116] **B. L. Györffy** and **M. J. Stott**, in *Band Structure Spectroscopy of Metals and Alloys*, edited by **D. J. Fabian** and **L. M. Watson**, p. 385, Academic Press, New York (1973).

- [117] **A. I. Liechtenstein, M. I. Katsnelson, V. P. Antropov, and V. A. Gubanov**, *Local spin density functional approach to the theory of exchange interactions in ferromagnetic metals and alloys*, J. Magn. Magn. Mater. **67** (1), pp. 65–74 (1987).
- [118] **A. R. Machintosh and O. K. Andersen**, in *Electrons at the Fermi Surface*, edited by **M. Springford**, p. 149, Cambridge Univ. Press, London (1980).
- [119] **V. Popescu and A. Zunger**, *Effective band structure of random alloys*, Phys. Rev. Lett. **104** (23), p. 236403 (2010).
- [120] **L. Nordheim**, *Zur Elektronentheorie der Metalle. I*, Ann. Phys. **401** (5), pp. 607–640 (1931).
- [121] **P. Soven**, *Coherent-potential model of substitutional disordered alloys*, Phys. Rev. **156** (3), pp. 809–813 (1967).
- [122] **A. J. Pindor, J. Staunton, G. M. Stocks, and H. Winter**, *Disordered local moment state of magnetic transition-metals – a self-consistent KKR CPA calculation*, J. Phys. F.: Met. Phys. **13** (5), pp. 979–989 (1983).
- [123] **J. Staunton, B. L. Gyorffy, A. J. Pindor, G. M. Stocks, and H. Winter**, *The disordered local moment picture of itinerant magnetism at finite temperatures*, J. Magn. Magn. Mater. **45** (1), pp. 15–22 (1984).
- [124] **M. Büttiker, Y. Imry, R. Landauer, and S. Pinhas**, *Generalized many-channel conductance formula with application to small rings*, Phys. Rev. B **31** (10), pp. 6207–6215 (1985).
- [125] **Y. Imry and R. Landauer**, *Conductance viewed as transmission*, Rev. Mod. Phys. **71** (2, SI), pp. S306–S312 (1999).
- [126] **T. Schäpers**, *Phase-coherent transport*, in *Nanotechnology, Information Technology I*, vol. 3, edited by **R. Waser**, WILEY-VCH Verlag GmbH & Co. KGaA, Weinheim (2008).
- [127] **S. Datta**, *Electronic transport in mesoscopic systems*, Cambridge University Press (1995).
- [128] **A. Smogunov, A. D. Corso, and E. Tosatti**, *Ballistic conductance of magnetic Co and Ni nanowires with ultrasoft pseudopotentials*, Phys. Rev. B **70** (045417), pp. 1–9 (2004).
- [129] **H. J. Choi and J. Ihm**, *Ab initio pseudopotential method for the calculation of conductance in quantum wires*, Phys. Rev. B **59** (3), pp. 2267–2275 (1999).
- [130] **I. P. Batra, P. Wurfel, and B. D. Silverman**, *Depolarization field and stability considerations in thin ferroelectric films*, J. Vac. Sci. Technol. **10** (5), pp. 687–692 (1973).
- [131] **J. Junquera and P. Ghosez**, *Critical thickness for ferroelectricity in perovskite ultrathin films*, Nature **422** (6931), pp. 506–509 (2003).

- [132] M. Y. Zhuravlev, R. F. Sabirianov, S. S. Jaswal, and E. Y. Tsymlal, *Giant electroresistance in ferroelectric tunnel junctions*, Phys. Rev. Lett. **94** (24), p. 246802 (2005).
- [133] V. Garcia, M. Bibes, L. Bocher, S. Valencia, F. Kronast, A. Crasous, X. Moya, S. Enouz-Vedrenne, A. Gloter, D. Imhoff, C. Deranlot, N. Mathur, S. Fusil, K. Bouzehouane, and A. Barthelemy, *Ferroelectric control of spin polarization*, Science **327** (5969), pp. 1106–1110 (2010).
- [134] J. P. Velev, C.-G. Duan, J. D. Burton, A. Smogunov, M. K. Niranjan, E. Tosatti, S. S. Jaswal, and E. Y. Tsymlal, *Magnetic tunnel junctions with ferroelectric barriers: Prediction of four resistance states from first principles*, Nano Lett. **9** (1), pp. 427–432 (2009).
- [135] D. I. Bilc, F. D. Novaes, J. Iniguez, P. Ordejon, and P. Ghosez, *Electroresistance effect in ferroelectric tunnel junctions with symmetric electrodes*, ACS NANO **6** (2), pp. 1473–1478 (2012).
- [136] M. Stengel, D. Vanderbilt, and N. A. Spaldin, *First-principles modeling of ferroelectric capacitors via constrained displacement field calculations*, Phys. Rev. B **80** (22), p. 224110 (2009).
- [137] M. Stengel, P. Aguado-Puente, N. A. Spaldin, and J. Junquera, *Band alignment at metal/ferroelectric interfaces: Insights and artifacts from first principles*, Phys. Rev. B **83**, p. 235112 (2011).
- [138] N. F. Mott, *The electrical conductivity of transition metals*, Proc. R. Soc. London, Ser. A **153**, pp. 699–717 (1936).
- [139] N. F. Mott, *The resistance and thermoelectric properties of the transition metals*, Proc. R. Soc. London, Ser. A **156**, pp. 368–382 (1936).
- [140] I. A. Campbell, A. Fert, and A. R. Pomeroy, *Evidence for 2 current conduction iron*, Phil. Mag. **15** (137), pp. 977–983 (1967).
- [141] A. Fert and I. A. Campbell, *2-current conduction in nickel*, Phys. Rev. Lett. **21** (16), pp. 1190–1192 (1968).
- [142] M. Julliere, *Tunneling between ferromagnetic films*, Phys. Lett. **54A**, pp. 225–226 (1975).
- [143] M. Bowen, M. Bibes, A. Barthelemy, J. Contour, A. Anane, Y. Lemaitre, and A. Fert, *Nearly total spin polarization in $La_{2/3}Sr_{1/3}MnO_3$ from tunneling experiments*, Appl. Phys. Lett. **82** (2), pp. 233–235 (2003).
- [144] S. S. P. Parkin, C. Kaiser, A. Panchula, P. M. Rice, B. Hughes, M. Samant, and S. H. Yang, *Giant tunnelling magnetoresistance at room temperature with MgO (100) tunnel barriers*, Nat. Mater. **3** (12), pp. 862–867 (2004).
- [145] S. Yuasa, T. Nagahama, A. Fukushima, Y. Suzuki, and K. Ando, *Giant room-temperature magnetoresistance in single-crystal Fe/MgO/Fe magnetic tunnel junctions*, Nat. Mater. **3** (12), pp. 868–871 (2004).

- [146] **X. G. Zhang** and **W. H. Butler**, *Band structure, evanescent states, and transport in spin tunnel junctions*, J. Phys.: Condens. Matter **15** (41), pp. R1603–R1639 (2003).
- [147] **X. G. Zhang**, **W. H. Butler**, and **A. Bandyopadhyay**, *Effects of the iron-oxide layer in Fe-FeO-MgO-Fe tunneling junctions*, Phys. Rev. B **68** (9), p. 092402 (2003).
- [148] **C. Heiliger**, **P. Zahn**, **B. Y. Yavorsky**, and **I. Mertig**, *Interface structure and bias dependence of Fe/MgO/Fe tunnel junctions: ab initio calculations*, Phys. Rev. B **73** (21) (2006).
- [149] **M. Y. Zhuravlev**, **S. S. Jaswal**, **E. Y. Tsymbal**, and **R. F. Sabirianov**, *Ferroelectric switch for spin injection*, Appl. Phys. Lett. **87** (22), p. 222114 (2005).
- [150] **J. D. Burton** and **E. Y. Tsymbal**, *Giant tunneling electroresistance effect driven by an electrically controlled spin valve at a complex oxide interface*, Phys. Rev. Lett. **106**, p. 157203 (2011).
- [151] **V. S. Borisov**, **I. V. Maznichenko**, **D. Böttcher**, **S. Ostanin**, **A. Ernst**, **J. Henk**, and **I. Mertig**, *Magnetic exchange interactions and antiferromagnetism of $ATcO_3$ ($A = Ca, Sr, Ba$) studied from first principles*, Phys. Rev. B **85**, p. 134410 (2012).
- [152] **G. Kresse** and **J. Hafner**, *Ab initio molecular-dynamics simulation of the liquid-metal–amorphous-semiconductor transition in germanium*, Phys. Rev. B **49** (20), pp. 14251–14269 (1994).
- [153] **G. Kresse** and **J. Furthmüller**, *Efficient iterative schemes for ab initio total-energy calculations using a plane-wave basis set*, Phys. Rev. B **54** (16), pp. 11169–11186 (1996).
- [154] **J. Hafner**, *Ab-initio simulations of materials using VASP: Density-functional theory and beyond*, J. Comp. Chem. **29** (13), pp. 2044–2078 (2008).
- [155] **P. Giannozzi**, **S. Baroni**, **N. Bonini**, **M. Calandra**, **R. Car**, **C. Cavazzoni**, **D. Ceresoli**, **G. L. Chiarotti**, **M. Cococcioni**, **I. Dabo**, **A. Dal Corso**, **S. de Gironcoli**, **S. Fabris**, **G. Fratesi**, **R. Gebauer**, **U. Gerstmann**, **C. Gougoussis**, **A. Kokalj**, **M. Lazzeri**, **L. Martin-Samos**, **N. Marzari**, **F. Mauri**, **R. Mazzarello**, **S. Paolini**, **A. Pasquarello**, **L. Paulatto**, **C. Sbraccia**, **S. Scandolo**, **G. Sclauzero**, **A. P. Seitsonen**, **A. Smogunov**, **P. Umari**, and **R. M. Wentzcovitch**, *QUANTUM ESPRESSO: a modular and open-source software project for quantum simulations of materials*, J. Phys.: Condens. Matter **21** (39) (2009).
- [156] **M. Lüders**, **A. Ernst**, **W. M. Temmerman**, **Z. Szotek**, and **P. J. Durham**, *Ab initio angle-resolved photoemission in multiple-scattering formulation*, J. Phys.: Condens. Matter **13** (38), pp. 8587–8606 (2001).
- [157] **H. Y. Hwang**, **Y. Iwasa**, **M. Kawasaki**, **B. Keimer**, **N. Nagaosa**, and **Y. Tokura**, *Emergent phenomena at oxide interfaces*, Nature materials **11**, pp. 103–113 (2012).

- [158] V. Vonk, J. Huijben, D. Kukuruznyak, A. Stierle, H. Hilgenkamp, A. Brinkman, and S. Harkema, *Polar-discontinuity-retaining A-site intermixing and vacancies at SrTiO₃/LaAlO₃ interfaces*, Phys. Rev. B **85**, p. 045401 (2012).
- [159] S. C. Chae, W. S. Choi, H. K. Yoo, and B. S. Kang, *Metal-insulator-like transition in the LaAlO₃/BaTiO₃ interface*, Current Applied Physics **11**, pp. 521–524 (2011).
- [160] J. Junquera and P. Ghosez, *Critical thickness for ferroelectricity in perovskite ultrathin films*, Nature **422**, pp. 506–509 (2003).
- [161] M. Stengel, P. Aguado-Puente, N. A. Spaldin, and J. Junquera, *Band alignment at metal/ferroelectric interfaces: insights and artifacts from first principles*, Phys. Rev. B **83**, p. 235112 (2011).
- [162] Y. Wang, M. K. Niranjana, J. D. Burton, J. M. An, K. D. Belashchenko, and E. Y. Tsymbal, *Prediction of a spin-polarized two-dimensional electron gas at the LaAlO₃/EuO(001) interface*, Phys. Rev. B **79**, p. 212408 (2009).
- [163] C. Franchini, T. Archer, J. He, X.-Q. Chen, A. Filippetti, and S. Sanvito, *Exceptionally strong magnetism in the 4d perovskites RTcO₃ (R = Ca, Sr, Ba)*, Phys. Rev. B **83**, p. 220402 (2011).
- [164] H. J. Monkhorst and J. D. Pack, *Special points for Brillouin-zone integrations*, Phys. Rev. B **13** (12), pp. 5188–5192 (1976).
- [165] G. Herranz, F. Sánchez, N. Dix, M. Scigaj, and J. Fontcuberta, *High mobility conduction at (110) and (111) LaAlO₃/SrTiO₃ interfaces*, Scientific Reports **2** (758) (2012).
- [166] D. J. Kim, H. Lu, S. Ryu, C.-W. Bark, C.-B. Eom, E. Y. Tsymbal, and A. Gruverman, *Ferroelectric tunnel memristor*, Nano Letters **12**, pp. 5697–5702 (2012).
- [167] M. Stengel and N. A. Spaldin, *Origin of the dielectric dead layer in nanoscale capacitors*, Nature **443** (7112), pp. 679–682 (2006).
- [168] N. Sai, C. J. Fennie, and A. A. Demkov, *Absence of critical thickness in an ultrathin improper ferroelectric film*, Phys. Rev. Lett. **102** (10), p. 107601 (2009).
- [169] N. A. Benedek and C. J. Fennie, *Hybrid improper ferroelectricity: a mechanism for controllable polarization-magnetization coupling*, Phys. Rev. Lett. **106** (10), p. 107204 (2011).
- [170] M. Stengel, C. J. Fennie, and P. Ghosez, *Electrical properties of improper ferroelectrics from first principles*, Phys. Rev. B **86** (9), p. 094112 (2012).
- [171] A. Y. Borisevich, H. J. Chang, M. Huijben, M. P. Oxley, S. Okamoto, M. K. Niranjana, J. D. Burton, E. Y. Tsymbal, Y. H. Chu, P. Yu, R. Ramesh, S. V. Kalinin, and S. J. Pennycook, *Suppression of octahedral tilts and associated changes in electronic properties at epitaxial oxide heterostructure interfaces*, Phys. Rev. Lett. **105**, p. 087204 (2010).

- [172] **I. I. Oleinik, E. Y. Tsymbal, and D. G. Pettifor**, *Atomic and electronic structure of Co/SrTiO₃/Co magnetic tunnel junctions*, Phys. Rev. B **65**, p. 020401 (2001).
- [173] **D. Di Sante, K. Yamauchi, and S. Picozzi**, *Beyond standard local density approximation in the study of magnetoelectric effects in Fe/BaTiO₃ and Co/BaTiO₃ interfaces*, J. Phys.: Condens. Matter **25** (6) (2013).
- [174] **T. Yamamoto**, *Ferroelectric properties of the PbZrO₃-PbTiO₃ system*, Jpn. J. Appl. Phys. **35** (9B), pp. 5104–5108 (1996).
- [175] **G. H. Haertlin**, *Hot-pressed ferroelectric lead zirconate titanate ceramics for electro-optical applications*, Am. Ceram. Soc. Bull. **49**, p. 564 (1970).
- [176] **B. Jaffe, R. S. Roth, and S. Marzullo**, *Properties of piezoelectric ceramics in the solid solution series lead titanate-lead zirconate-lead oxide: tin oxide and lead titanate-lead hafnate*, J. Res. Nat. Bur. Stds **55**, pp. 239–254 (1955).
- [177] **J. M. De Teresa, A. Barthelemy, A. Fert, J. P. Contour, F. Montaigne, and P. Seneor**, *Role of metal-oxide interface in determining the spin polarization of magnetic tunnel junctions*, Science **286** (5439), pp. 507–509 (1999).
- [178] **L. Jiang, W. S. Choi, H. Jeon, S. Dong, Y. Kim, M.-G. Han, Y. Zhu, S. V. Kalinin, E. Dagotto, T. Egami, and H. N. Lee**, *Tunneling electroresistance induced by interfacial phase transitions in ultrathin oxide heterostructures*, Nano Letters **13** (12), pp. 5837–5843 (2013).
- [179] **Y. W. Yin, J. D. Burton, Y.-M. Kim, A. Y. Borisevich, S. J. Pennycook, S. M. Yang, T. W. Noh, A. Gruverman, X. G. Li, E. Y. Tsymbal, and Q. Li**, *Enhanced tunnelling electroresistance effect due to a ferroelectrically induced phase transition at a magnetic complex oxide interface*, Nat. Mater. **12**, pp. 397–402 (2013).
- [180] **H. Chen and S. Ismail-Beigi**, *Ferroelectric control of magnetization in La_{1-x}Sr_xMnO₃ manganites: a first-principles study*, Phys. Rev. B **86** (2) (2012).
- [181] **F. Tsui, M. C. Smoak, T. K. Nath, and C. B. Eom**, *Strain-dependent magnetic phase diagram of epitaxial La_{0.67}Sr_{0.33}MnO₃ thin films*, Appl. Phys. Lett. **76** (17), pp. 2421–2423 (2000).
- [182] **J. Henk**, *Integration over two-dimensional Brillouin zones by adaptive mesh refinement*, Phys. Rev. B **64** (3) (2001).
- [183] **B. Zheng and N. Binggeli**, *Effects of chemical order and atomic relaxation on the electronic and magnetic properties of La_{2/3}Sr_{1/3}MnO₃*, J. Phys.: Condens. Matter **21** (11) (2009).
- [184] **D. Petti, A. Stroppa, S. Picozzi, S. Brivio, M. Cantoni, and R. Bertacco**, *Effect of Au proximity on the LSMO surface: An ab initio study*, J. Magn. Magn. Mater. **324** (17), pp. 2659–2663 (2012).

List of publications

- [1] V. S. Borisov, I. V. Maznichenko, D. Böttcher, S. Ostanin, A. Ernst, J. Henk, and I. Mertig, *Magnetic exchange interactions and antiferromagnetism of $ATcO_3$ ($A = Ca, Sr, Ba$) studied from first principles*, Phys. Rev. B **85**, 134410 (2012).
- [2] V. S. Borisov, S. Ostanin, I. V. Maznichenko, A. Ernst, and I. Mertig, *Magnetoelectric properties of the $Co/PbZr_xTi_{1-x}O_3$ (001) interface studied from first principles*, Phys. Rev. B **89**, 054436 (2014).

Earlier published papers:

- [1] V. S. Borisov, *Contribution of the interphase interaction to the internal energy and thermodynamic properties of dispersed matrix composites*, Mod. Phys. Lett. B **25**, 781 (2011).
- [2] V. S. Borisov, Yu. V. Agrafonov, L. A. Shcherbachenko, Ya. V. Ezhova, S. S. Baryshnikov, O. B. Rubtsova, *Specific features of the dielectric response of heterogeneous systems with a polar matrix containing electrically active inclusions*, Physics of the Solid State **53** (1), pp. 53–58 (2011).
- [3] V. S. Borisov, *Pool-Frenkel effect in polar liquids placed in strong electric fields*, Mod. Phys. Lett. B **24**, 2625 (2010).
- [4] V. S. Borisov, S. D. Marchuk, Ya. V. Ezhova, S. S. Baryshnikov, V. S. Marchuk, L. A. Shcherbachenko, *Electret effect in heterogeneous systems comprising low-dimensional particles with electrically active surface*, Russian Physics Journal **53** (5), pp. 493–498 (2010).
- [5] L. A. Shcherbachenko, V. S. Borisov, N. T. Maksimova, E. S. Baryshnikov, Ya. V. Ezhova, V. A. Karnakov, S. D. Marchuk, Yu. T. Eine, *Electret-thermal and dielectric analyses of electrically active colloids*, Technical Physics **55** (8), pp. 1209–1215 (2010).
- [6] V. S. Borisov, L. A. Shcherbachenko, *Specific features of the thermodynamic equilibrium state of a thin water film in an electric field of surface active centers of a mica crystal*, Physics of the Solid State **51** (12), pp. 2546–2552 (2009).
- [7] L. A. Shcherbachenko, V. S. Borisov, N. T. Maksimova, E. S. Baryshnikov, V. A. Karnakov, S. D. Marchuk, Ya. V. Ezhova, L. I. Ruzhnikov, *Electret effect and electrotransport in disperse organic and inorganic systems*, Technical Physics **54** (9), pp. 1372–1379 (2009).
- [8] V. A. Karnakov, V. S. Borisov, Ya. V. Ezhova, S. V. Marchuk, A. R. Kharlan, L. A. Shcherbachenko, *Spectroscopy of thermally activated thin water layers*, Russian Physics Journal **51** (8), pp. 840–843 (2008).

- [9] **V. S. Borisov, V. A. Karnakov, Ya. V. Ezhova, O. B. Rubtsova, L. A. Shcherbachenko**, *Specific features of the polarization of thin water films in the field of the active surface of a mica crystal*, *Physics of the Solid State* **50** (6), pp. 1022–1027 (2008).

Acknowledgements

I would like to thank everybody who inspired and supported me during the preparation of this work.

First of all, I would like to sincerely thank my supervisor Prof. Dr. Ingrid Mertig for giving me a great opportunity to conduct research in the fascinating field of multi-ferroics and exchange ideas with other scientists on the international conferences and workshops. I am grateful to her for guiding me through all these years and for the numerous fruitful discussions that ignited my interest and improved my understanding in this field. It was a great pleasure to be a member of her research group at the Martin Luther University Halle-Wittenberg, and I would like to say thanks to my colleagues for a friendly atmosphere and a good deal of memorable moments. Our coffee meetings and group seminars always provided enough food for thought.

At this point, I would like to thank Sergey Ostanin for helping me to learn first-principle calculations and for supporting me at venturing new research venues. He shared a lot of his knowledge with me in these years and always found time for detailed discussions which was essential for producing new ideas and solving tricky problems. Many thanks as well to Steven Achilles for sharing with me his vast experience in the scientific computing and some programming tricks. I would like to say thanks to Francisco Muñoz for many good memories and for inspiring me to start programming in Python, which made a lot of things much easier and faster. Not to be forgotten here is a friendly support from my colleagues in the office, Michael Strauch, who gave me many valuable advices in daily life, and Dmitry Fedorov, with whom I had many nice conversations. My thanks are given here also to Helgard Meyn and Jurate Claus for a kind help with many work-related issues.

I enjoyed very much the atmosphere at the Max Planck Institute of Microstructure Physics, in particular, during weekly seminars within the International Max Planck Research School and invited talks at the institute. Many thanks to everybody who contributed to the success of these events. In addition, I would like to thank Marin Alexe, Dietrich Hesse and Andy Quindeau for a great collaboration and many insightful experiments. My thanks are given here also to Udo Schmidt, since without his assistance many of the demanding calculations performed in this work would be missing now. I would like to thank Maria Santo for helping me during my first steps in Halle and Ina Goffin for her kind support during the preparation for conferences. Many thanks to Violetta Neuber, our German teacher at the institute, for helping me to improve my language skills.

A very special and simultaneously enriching experience was the organization of the IMPRS/SFB workshop, which took place in Halle in the beginning of October 2013. I am glad having had an opportunity to work together with Danny Thonig, Martin Hoffmann and Safa Golrokh Bahoosh during this time, and I thank these people for this and many other nice moments.

Finally, I would like to heartily thank my family, especially my mother for making it possible for me to live in the wonderful world of physics and for encouraging me in difficult situations during all my life. Without her constant support and understanding the successful accomplishment of this work would have been impossible to imagine.

Curriculum vitae

PERSONAL INFORMATION

Name Vladislav Borisov
Address Max-Nenke-Str. 1, 06120 Halle (Saale), Germany
Date and place of birth 05.05.1988, Irkutsk (USSR)

EDUCATION AND WORK EXPERIENCE

since 06/2014 Research assistant in the group of Prof. Dr. Ingrid Mertig at the Institute of Physics, Martin Luther University Halle-Wittenberg. Halle (Saale), Germany.

2012 – 2013 Member of the conference committee of the “Joint IMPRS/SFB Workshop on Nanoscience and -technology” (30.09 – 02.10.2013), Halle (Saale), Germany.

03/2011 – 05/2014 Doctoral candidate at the Max Planck Institute of Microstructure Physics. Halle (Saale), Germany.

03/2011 – 05/2014 Member of the International Max Planck Research School for Science and Technology of Nanostructures.

2008 – 2010 Research assistant at the Department of Physics, Irkutsk State University.

2004 – 2009 Study of physics at Irkutsk State University. Diploma in physics with honors, the awarded qualification: “Radiophysicist” specializing in “Radiophysics and electronics”. Diploma title: “Thermostimulated and dielectric spectroscopy of heterogeneous systems containing structured water”.

2007 – 2009 Study of educational technologies at Irkutsk State University. Diploma of extended education with honors, the awarded special qualification: “Teacher”. Diploma title: “Use of information technologies for students”.

2001 – 2004 Winner of Olympiads in physics, mathematics, and informatics.

1997 – 2001 Irkutsk Regional School of Arts, department of drawing. Stipendiary from 1998 till 2001. Certificate with honors No. 490 from 25.05.2001.

1994 – 2004 Lyceum No. 3 (Irkutsk) with extended education in physics and mathematics. Certificate of secondary education with honors.

Halle (Saale), 16 October 2014

Vladislav Borisov

Eidesstattliche Erklärung

Hiermit erkläre ich gemäß §5 der Promotionsordnung der Naturwissenschaftlichen Fakultät II der Martin-Luther-Universität Halle-Wittenberg vom 13.06.2012, dass ich die vorliegende Arbeit

Multiferroic interfaces of mixed valency systems studied from first principles

selbstständig und ohne fremde Hilfe verfasst, keine anderen als die von mir angegebenen Quellen und Hilfsmittel benutzt und die den benutzten Werken wörtlich oder inhaltlich entnommenen Stellen als solche kenntlich gemacht habe.

Desweiteren erkläre ich, dass ich die Angaben wahrheitsgemäß gemacht habe und keine Arbeit an einer anderen wissenschaftlichen Einrichtung zur Erlangung eines akademischen Grades eingereicht habe.

Halle (Saale), den 16. Oktober 2014

Vladislav Borisov